ENERGY HARVESTING NEAR THE HUMAN BODY USING FINITE-DIFFERENCE TIME-DOMAIN SIMULATIONS

by

Rachel S. Lumnitzer

A thesis submitted to the Faculty and the Board of Trustees of the Colorado School of Mines in partial fulfillment of the requirements for the degree of Master of Science (Electrical Engineering).

Golden, Colorado

Date _____

Signed: _____

Rachel S. Lumnitzer

Signed: _____

Dr. Atef Z. Elsherbeni
Thesis Advisor

Golden, Colorado

Date _____

Signed: _____

Dr. Peter Aaen
Department Head
Department of Electrical Engineering

ABSTRACT

The finite-difference time-domain (FDTD) algorithm is a very useful numerical technique used to solve Maxwell's equations in either the time or frequency domain by approximating the derivatives. This work focuses on biomedical applications of the algorithm with and without dispersive media representing human tissues. The use of dispersive media requires adaptations to the FDTD algorithm since the material properties change with frequency. This is a unique challenge faced by today's 5G biomedical applications of FDTD that use human biological tissues. One of the most efficient and powerful ways to apply dispersive media such as human tissues in FDTD is with the Debye model. Once the human tissues are fully characterized accordingly using Debye, a dispersive FDTD formulation can be used to accurately assess the performance of the model.

The goal of this thesis is to characterize the Debye parameters for several human tissues up to 100 GHz and apply them to the FDTD algorithm to evaluate practical 5G biomedical applications. The applications focus on the wireless charging optimization of 5G biomedical devices using dielectric cylinders placed above the human tissues. The device would be installed, for example, on the surface of a patient's wrist. The application is explored in the 2D space as well as 3D space for the same relative model dimensions.

As a first step and quick analysis, a 2D application is developed that uses the traditional FDTD algorithm in the time domain with the dielectric properties of the human tissues. A reflector antenna is included in the 2D analysis to focus the incident wave on the tissue area. Next, a practical 3D application is developed that uses the dispersive FDTD adaptation of the algorithm with the Debye parameters of the human tissues included in the model. The results show approximately 3 to 8 dB of gain in general and at certain positions the gain can reach 10 dB with the use of the optimized dielectric cylinders placed on the first tissue layer. The resulting incident E-field is focused on the surface of the tissue layers. This thesis shows the practical advantages of using the Debye model for human tissues and how to increase the performance of 5G biomedical applications.

TABLE OF CONTENTS

LIST OF FIGURES

LIST OF TABLES

LIST OF SYMBOLS

Capacitance C

Current I

Current density . . . . . J

Electric field . . . . . E

Gram . . . . . g

Inductance L

Magnetic field . . . . . H

Material conductivity . . . . . σ

Material permeability . . . . . μ

Material permittivity . . . . . ϵ

Meter . . . . . m

Permeability of free space . . . . . μ_0

Permittivity of free space . . . . . ϵ_0

Relative permeability . . . . . μ_r

Relative permittivity . . . . . ϵ_r

Resistance . . . . . R

Wavelength of electromagnetic wave . . . . . λ

LIST OF ABBREVIATIONS

Colorado School of Mines	CSM
Electromagnetic	EM
Finite Difference Frequency Domain	FDFD
Finite Difference Time Domain	FDTD
Method of Moments	MoM
Multiple Input Multiple Output	MIMO
Specific Absorption Rate	SAR

ACKNOWLEDGMENTS

I would like to thank everyone that made this thesis a reality. This thesis would not have been possible without Dr. Atef Z. Elsherbeni's continuous support and guidance over the last few years. I would like to thank Yiming Chen, Fatih Kaburcuk, Allison Tanner, and Andres Velasco for all their help in conducting my research. I would also like to thank my family and friends for all their support while working on this thesis.

CHAPTER 1

INTRODUCTION

The finite difference time domain (FDTD) method has been well characterized for computational electromagnetic simulations for various multi-dimensional 5G applications involving near-field and far-field sources [1]. However, as frequencies increase in wireless communication applications, the need for increasingly complex electromagnetic solvers is also required. Several 5G applications use the WiFi bands of 2.45 and 5.8 GHz though this work will primarily focus on applications at the high frequency bands of 24 GHz (n258 band), 28 GHz, and 29 GHz (n257 and n261 bands) [2]. This thesis demonstrates the optimization of the FDTD algorithm for biomedical applications at one of the upper ranges of 5G frequencies.

The motivation is based on the increasing demand for emerging 5G device technologies to provide the necessary capacity and performance for increasing data rates of mobile data traffic [2]. A solution to enhance capacity and data rates is through the bandwidth. Technologies that use 2.45 GHz or lower are limited in not just bandwidth but also available space, thus, high frequency allocated bands are of interest. The use of mm-wave bands enhances wireless communication quality but also provides more compact designs. However, some challenges with higher frequency devices include higher path loss, increased sensitivity to manufacturing defects and tolerances, and health concerns regarding specific absorption rate (SAR) with no standard in place at frequencies above 24 GHz. Some of these challenges can be addressed with the design; the path loss can be reduced with high directive gain radiation patterns with respect to the direction of propagation and the health effects can be evaluated by measuring the power density [2]. Despite these considerations, there is a need for research and demonstrated performance of 5G devices at the higher frequency range.

1.1 Literature Review

A literature review is conducted on the wearable design constraints, current designs and technologies, and computational electromagnetic modeling for human tissues.

1.1.1 Advances in 5G Biomedical Technology

The healthcare industry is rapidly transitioning from a traditional hospital approach to a patient-focused approach. Wireless communication technologies have enabled patients to receive remote medical care. As the smart healthcare market expands within the 5G network, the number of applications connected to the network will create demands in terms of bandwidth and data rates. The 5G network can

meet the demands by providing high bandwidth, high efficiency, reliability, and low latency, as well as increased cellular coverage, potential data rates of Gb/s, and added security benefits [3].

The primary focus area for biomedical applications is 5G wearable antennas for medical devices and remote monitoring of patient health. The number of wearable devices has increased from 325 million in 2016 to approximately 720 million in 2019 and is predicted to grow to over 1.1 billion [2]. Wearable devices such as sensors and smart watches collect data such as blood pressure, heart rate, amount of sleep, and continuous monitoring of patients with chronic illnesses [3].

The 5G network must have smart biomedical devices that support high dense networks due to many devices within a given area and high energy consumption. The typical 5G antenna devices typically focus on the industrial, scientific, and medical (ISM) bands of 902 to 928 MHz, 2.4 to 2.5 GHz, and 5.725 to 5.875 GHz [4]. However, higher 5G bands of 20 GHz and above offer unused bandwidth to meet these needs [3]. The 20 to 30 GHz band is considered appropriate for wearable technology according to the WiGig protocol (IEEE 802.11ad) [4]. The most promising bands include 28 to 30 GHz for local multi-point distribution, 60 GHz for license-free requirements, 71 to 76 GHz, 81 to 86 GHz, and 92 to 95 GHz [5]. The mm-wave bands have potential to provide exceptionally high energy efficiency given reasonable power consumption estimates which could prove useful for biomedical devices with power transfer limitations [5]. However, the 5G wearable devices described here for biomedical applications are primarily based below the mm-wavelengths of 1 to 10 mm or 30 to 300 GHz [6].

Some of the challenges faced by mm-wave antenna designs at 5G frequencies of 30 GHz or higher include fabrication tolerance issues affecting performance, lack of SAR data, large path loss, narrow beam-width, and sensitive operation [2]. This higher frequency band also includes the intense rate of heating and potentially unsafe SAR values, or radiation exposure on the human body, despite an average power density of less than 20 mW/cm^2 [6]. However, a textile-based mm-wave antenna is described in [7] that operates within the 24.9 to 31.1 GHz band with a gain of 8.2 dBi. The researchers also explore using a 13 by 13 element array that showed potential for a power reception that is six times higher than a traditional patch antenna [7].

Wireless power transfer and energy harvesting are crucial areas of research for remotely monitored devices [8]. They enable wireless charging of the wearable devices to either extend battery life or prevent the need for batteries. Wearable biomedical devices such as a wristband sensor are low power and consume approximately 0.83 mW whereas implantable devices such as a pacemaker consume 1 uW [8]. Wireless power transfer is where the electric power is transferred from a source to load such as through a time oscillating electromagnetic field. It can be classified as far-field radiative systems or near-field non-radiative systems. The most well-known techniques for wireless power transfer are inductive coupling, magnetic

resonant coupling, as well as electromagnetic radiation. However, it is often used for static devices rather than mobile devices due to the short-range limit and line of sight issues [8]. Energy harvesting techniques scavenge power from various sources and convert it to electric energy. Potential energy harvesting sources include light or vibration energies, body warmth, solar, wind, piezoelectricity, heartbeat, and radio frequency energy. The energy harvester source is converted as applicable with AC-DC and DC-DC converters, the output voltage level is maintained with voltage regulators, and the energy is stored as specified by the application [8].

Wireless power transfer technology has performed well for sub 6 GHz systems with high efficiency. The near-field systems are applicable for wearable biomedical devices as the transmitted wavelength is larger than the receiver distance [8]. The power is transferred by capacitive coupling with an electric field or inductive coupling with a magnetic field. For small multi-band antennas, antenna booster technology has been recently used to excite currents in the ground plane of IoT devices using a matching network with passive components [9].

Energy harvesting technologies prevent the need to replace batteries and are promising for wearable biomedical devices to extend their lifespan of use. Some of the main energy harvesters include triboelectric nano generators (TENG), piezoelectric generators (PEG), and thermoelectric generators (TEG) that are typically transducers. However, these technologies struggle to produce efficient output power and are limited to certain areas of the body such as joints [8], [10]. Another area of energy harvesting that may solve this issue is body coupled power transmission to deliver power to the body and harvest energy from coupled ambient electromagnetic waves at the same time [10]. In [10], a body-coupling mechanism uses a TX and RX integrated circuits (IC) design for energy harvesting and power transmission for the entire body area independent of body placement. However, this mechanism operates at 40 MHz rather than 5G to minimize the path loss.

Another important topic of remotely monitored 5G biomedical devices is the wireless body area network (WBAN) as a wireless technology expected to revolutionize real-time monitoring capabilities of biomedical sensors [8]. WBAN is a subset of the Wireless Sensor Network (WSN) consisting of low power devices. It connects sensors situated on the body or implanted under the skin that typically applies to the whole human body with the sensors connected using a wireless communication channel [11]. The sensors collect, process, and send data to a medical server [8]. The sensor nodes gather medical parameters such as Electrocardiogram (ECG) and transmit to an intermediate router node or coordinator node [11]. Two types of communication occur either between the sensors or between the central node and an external access point [12].

1.1.2 Wearable 5G Antennas

Wearable antennas have special design constraints to accommodate to the human body. Current applicable 5G antenna designs include microstrip patch antennas, dual-band antennas, multiple-input multiple-output (MIMO) antennas, wide-band antennas, and radio frequency identification (RFID) tags [13]. They must be made of flexible, robust materials and perform with minimal degradation next to human tissue. Conductive textiles have potential for shielding electrical components and are a practical medium for antennas and circuits. Insulating textiles refer to substrates for antennas and include natural as well as synthetic materials [13]. Substrates typically consist of Flame Retardant-4 (FR4), Polydimethylsiloxane (PDMS), Polyethylene Terephtalate (PET), Indium Tin Oxide (ITO), or paper [14]. The conductive layer is typically Copper, Aluminum, Silver ink, Nickel/Copper fabrics, or Nickel-plated Polyester cloth [14]. Meta-materials are periodic artificial materials with electrical properties that depend on the material structure often used for high efficiency wearable medical systems [15]. Fabrication techniques of flexible antennas primarily consist of embroidery or printing technologies for seamless integration and light weight design. Wearable devices must also be compact in size, within safety limits for users, and provide efficient power transfer [13]. The antenna may also be deformed or bent when worn and performance must not be degraded. The coupling between the antenna and human body can cause dangerous electromagnetic exposure [16]. Though most 5G biomedical devices show safe SAR exposure levels at sub 6 GHz bands, higher frequencies require further assessment. However, a recent study shows safe SAR exposure limits with realistic input power levels for a wearable antenna operating at 26.5 GHz [12]. Another challenge is that human tissues are lossy and affect antenna efficiency and gain [2].

Microstrip rectangular patch antennas and arrays are often used at 5G frequencies and can use a polymer substrate and conductive nanoparticles for flexibility and robust performance. However, miniaturization of the materials is a challenge near mm-wave frequencies. A common solution is to increase the dielectric constant of the substrate which cannot be implemented with a textile material. A rectangular patch antenna is described in [14] which uses denim cloth with a dielectric constant of 1.7 and stacked photo paper with a dielectric constant of 5.2 as the textile materials for the substrates. The antenna shows optimal performance at 3 GHz and 6 GHz for denim and paper, respectively. The antenna fabricated with denim shows a gain of 8.71 dB for denim and 2.45 dB for photo paper [14]. An alternative solution to the constraints of the textile uses an electromagnetic band gap (EBG) structure to prevent propagation at certain frequencies [13]. A recent study uses two different single patch antennas with EBG applied in a mushroom pattern operating at 3.5 GHz and 26.5 GHz, respectively, to evaluate the SAR exposure for wearable devices [12]. The antennas are simulated using FDTD with 3D human body models and situated

on the surface of the chest with a 2 mm distance from the tissue to simulate a wearable device. The input power of the antennas are set to 1 W and exposure levels all comply with the International Commission on Non-Ionizing Radiation Protection (ICNIRP) guidelines [12]. Another recent design of a photo-acoustic patch uses VCSEL laser diodes and piezoelectric transducers to optimize optical energy intensity and image quality of bio-molecules in deep tissues, respectively [17]. The patch is made of a soft and flexible elastomer substrate for comfortable long-term monitoring of applications such as low blood perfusion that may cause organ dysfunction. Unlike many antenna designs, bending, twisting, and other mechanical deformations do not affect the performance [17]. The need for 5G antennas for biomedical applications operating at low power consumption has led to designs at higher frequencies. A recent design of a four-element patch antenna array with a self-switching Graphene diode operating at 28 GHz shows promising results with an RF input power of approximately 500 uW [18].

Circular patch antennas utilizing meta-materials are a recent design approach shown to have comparably higher efficiency for medical systems, better symmetry, and more effective ability to create circular polarization [15]. A stacked circular patch with a circular split-ring resonator (CSRR) operating at 2.6 GHz has been shown to have a gain of approximately 8.5 dB and 95% efficiency. For circular patch antennas with CSRR, the gain is 2 to 3 dB higher than without when considering the dielectric properties of the human tissues for placement on the patient's stomach [15].

Dual-band antennas operate at dual 5G frequencies and have minimal degradation when bent or shifted, which works well for wearable devices [13]. A design for a compact dual-band patch antenna for biomedical sensors operating at 2.4 and 5.4 GHz is described in [19] which uses a SRR and EBG to show a higher gain of 7.22 dB and 7.39 dB and efficiency of 62.3% and 64.7% at 2.4 and 5.4 GHz, respectively. When bent 22.3 degrees, the gain is 4.21 dB and 6.22 dB and efficiency is 37.3% and 52.45% for 2.4 and 5.4 GHz, respectively. The results are simulated on a geometric model of the human arm tissue including their dielectric properties [19]. A design for an ultra wide-band (UWB) flexible dual-band notched antenna with notches at 2.4 to 3.7 GHz and 5.15 to 5.725 GHz is proposed in [20]. The antenna covers a bandwidth of 2.05 to 14 GHz with a high gain of 12.7 dB at 8.4 GHz. The UWB design allows for an acceptable level of frequency shifting as bending of the structure occurs for biomedical device applications [20].

Wide-band antennas are also common for wearable applications due to the wide bandwidth and acceptable performance in gain and efficiency when bent about the human body [21]. A low-profile wide-band antenna operating at 2.4 GHz is shown in [21] and the bandwidth, gain, efficiency, and SAR 1 g values are compared for the free space and human body model. The design is a rectangular patch with rectangular slots added and a partial ground plane to improve the bandwidth. The parameters are simulated for the antenna on the chest, leg, and arm tissue. Experimental results show decreased fractional

bandwidths than free space but still optimal for wearable applications. The resonant frequency is lower than free space as expected due to the high permittivity of human tissue [21].

MIMO antennas are a new application of nanotechnology which utilize a flexible metallic mesh as the conductor, flexible dielectrics, and an overall compact design [13]. MIMO technology uses multiple receivers to receive a transmitted signal and the best among the receivers is processed for the data [13]. A wearable, two-dimensional meta-material MIMO antenna consisting of six elements operating at 5.6 GHz is proposed in [22] with a maximum gain of 7.95 dB and SAR values below the limit of less than 1.6 W/kg for 1 g of human tissue when simulated 10 mm from the surface of a human phantom model. Again, the human tissue model accounts for the dielectric properties of each tissue layer. A design for a silicone rubber wristband MIMO antenna is described in [23] covering a frequency range of 2.75 to 12 GHz. The gain is 3.41 dB, efficiency 89.3%, and SAR of 0.536 W/kg per 1 g of tissue. The wristband uses UWB up to 12 GHz as recommended for medical therapeutic technologies. The antenna is modeled with a cylindrical human wrist model consisting of the dielectric properties at 3, 6, and 10 GHz [23].

RFID technology is used in various industries including patient monitoring in the biomedical and healthcare sectors. Passive RFID tags do not have a power supply and use fixed readers for detection, whereas active RFID tags are battery powered. Chipless RFID is suggested to have lower cost and maintenance with lower power requirements. Passive RFID has incredible potential for sensors such as monitoring the patient's healing status by inserting the RFID tag close to the wounded tissue during the last stage of the surgery [24]. However, these tags often are considered for implantable technologies with biodegradable materials that may have lasting effects on patients after use. They are also often proposed for wearable devices such as a smartwatch with e-skin sensors using electric field coupling through the patient's body. Though most RFID tags used for this application operate in the ultra-high frequency (UHF) band, this passive RFID tag operated far below 5G at 13.6 MHz [25].

Another methodology for 5G wireless devices is implementing perfectly conducting targets above a human tissue model using a far-field source [16]. The model uses the electrical properties of muscle, and the source operates at 2.4 GHz and 28 GHz. The study aims to understand the role of unwanted objects, such as jewelry, close to a wearable antenna. The model uses a 2D cylindrical wave approach with cross sections of conductive cylinders, a plane-wave source, and the biological tissue. The results include cases for one, three, five, and seven cylinders of various radii sizes for 2.4 GHz and seven cylinders for 28 GHz. For TM polarization, the conductive cylinders have a shielding effect to penetration of the electric field source for the muscle tissue. For TE polarization, the penetration of the electric field is enhanced [16].

The approach with conductive cylinders can also be applied to dielectric cylinders. The study of the effects of a plane wave source on dielectric cylinders has several applications such as microwave heating and

near-field optics [26]. The formulation determines the plane-wave scattering by the dielectric cylinder on a plane surface to calculate the field inside the cylinder. Dielectric cylinders can also be used with a human tissue model to enhance focusing of the electric field source for wireless power transfer of wearable devices [27]. The formulation in [26] is applied to the human tissue model in [27] using the 2D cylindrical wave approach at 24 GHz for over 6 dB of gain. This work is further extended in this thesis.

1.1.3 Modeling Human Tissue

Several of the designs discussed thus far involve human tissue models for analysis of wearable antenna technologies. Most of these models focus on the dielectric properties of the tissues consisting of the electrical permittivity, conductivity, and loss tangent. The primary purpose has been to analyze the frequency, bandwidth, wireless power transfer, and SAR values for safe exposure limits.

A notable parameter to also consider is the dielectric dispersive nature of human tissues. FDTD modeling of antennas with human tissues is affected by such dispersive media and requires algorithms using either the Debye or Lorentz models. The Debye formulation is used in [28] to determine the necessary Debye parameters using a frequency domain approach. They are computed for each biological tissue at certain frequency ranges that can be applied to a human tissue model to account for the dispersion of the complex permittivity [28]. A similar model has been obtained confirming strong correlation between measured complex permittivity and relaxation time from human tissue phantoms scanned with MRI. The model provides insight into computing accurate dielectric properties based on application relaxation times of the human body [29]. The Cole-Cole model can also be used to fit the data for human tissues, however, implementation into FDTD is more difficult than using the Debye model [30]. The Debye model can change the fit of the data with a set number poles within the formulation. If the number of poles is increased, the accuracy of the fit is likely to increase. From poles two to four, the deviation of the Debye model is shown to decrease with a low relative error [30]. Increasing the poles above four does not significantly improve the fitting of the data. In [30], the measured complex permittivity for the human hand of 22 volunteers for a frequency range of 5 to 67 GHz is used to determine if there is an effect on 5G antenna performance. The antenna array operates at a band of 5.9 to 7.1 GHz. The S parameters and radiation efficiency are minimally affected by the variation in dielectric properties [30].

Another parameter is the impact of a human tissue model consisting of layers of tissue or a 3D voxel model of the human body. Most of the designs discussed here use a human tissue model with layers to account for a cross section of the human body. In [31], a wearable meandered loop antenna is simulated with an imported 3D voxel model as well as simplified human tissue model for 3D modeling in CST Microwave Studio. The results are in good agreement suggesting either approach can be used depending on

the biomedical application. In [32], the voxel model is constructed using transverse grey scale images of the human body with MRI scans. The images are re-scaled for applicable spatial resolution of the voxels.

1.2 Thesis Layout

The goal of this thesis is to provide practical analyses and validation for 5G biomedical applications. The biomedical applications described here include human tissue image processing based on MRI technologies, a human wrist phantom model, as well as optimization of wireless charging of wearable biomedical devices with 2D FDTD and 3D dispersive FDTD computational analyses [1].

The first step before addressing these applications is to analyze the dielectric properties of the human tissues, compute the necessary parameters for the analyses, and discretize the tissues. Chapter 2 describes these human tissue model characteristics. Human tissue characterization has been successfully performed from 100 MHz to 100 GHz and applied to the first higher frequency band of 5G [33]. The dielectric properties are provided for several allocated 5G frequency bands including 1 GHz to 5 GHz, 5 GHz to 20 GHz, 20 GHz to 30 GHz, 30 GHz to 40 GHz, and 40 GHz to 90 GHz. The Debye expansion coefficients are computed based on a two-step numerical solver and provided for 100 MHz to 2 GHz, 2 GHz to 20 GHz, and 20 GHz to 100 GHz [33]. These Debye parameters predict the complex permittivity of the experimental data to be used for FDTD applied to dispersive tissue mediums for analysis. The tissues are discretized in the computational domain at various resolutions based on MRI medical image processing.

The next step is to use the human tissue model for FDTD models. Chapter 3 describes the 2D FDTD applications. The FDTD method is used in a 2D domain at the higher 5G frequencies for wireless charging of wearable biomedical device applications. The results are validated for 28 GHz. Chapter 4 describes the 3D FDTD applications. The FDTD method and human tissue model are used for a 3D domain simulation for dispersive media using the Debye expansion coefficients. Chapter 5 includes the conclusion and future work. This thesis provides an example of the process and analysis tools required for the new biomedical technologies emerging at 5G frequencies of interest.

1.3 Main Contributions

The author's main contributions to this thesis consist of characterization of human tissues described here as well as implementation to FDTD simulations for the energy harvesting application of wireless charging near a human wrist tissue model for the 2D and 3D cases. The collection of the dielectric properties, computation of Debye parameters from 100 MHz to 100 GHz, and comparison for accuracy is the author's own work described in [33]. The author's Debye parameters are applied to the evaluation of a human head model to determine the SAR values and temperature rise in the head tissue up to 100 GHz as

described in [34]. The SAR_{1g}, SAR_{10g}, and temperature rise values are below the specified limits above which would cause physiological damage to the tissues [34]. The use of the Debye parameters and evaluation of the human wrist tissue model for image discretization accuracy in MATLAB are the author's contributions to the research described in [35]. The human tissue parameters and 3D model of the human wrist are then used to simulate a model setup with seven dielectric cylinders to determine the energy harvesting potential gain using the FDTD algorithm. This model is applied to non-dispersive 2D FDTD code as well as dispersive 3D FDTD code. The model setup with the human tissue parameters and evaluation of the relative gain for the respective cases is the author's own work.

CHAPTER 2

HUMAN TISSUE MODEL

Before the FDTD method can be used for biomedical applications, the human tissue model must first be studied to determine the properties of the tissues and proper discretization for accurate computational analysis. This process is conducted for 55 human tissues. The process consists of collecting the dielectric properties of the tissues, computing the Debye expansion coefficients to be used for dispersive models, and optimizing the imported human tissue model in MATLAB.

2.1 Human Tissue Characterization

First, the human tissue model must be characterized for various tissue parameters for accurate analysis. The first step is to collect the dielectric properties for each tissue obtained from available literature [36]. Next, the tissue properties are applied to a two-step numerical solver in MATLAB to obtain the equivalent Debye parameters that can be used for FDTD simulations requiring dispersive media [33]. The Debye model is particularly useful for providing computational efficiency for a large range of frequencies in a simulation. The process described here has been completed by the author in [33] for 55 human tissues from 100 MHz to 100 GHz.

2.1.1 Dielectric Properties

The properties for human tissues include the relative permittivity and electric conductivity for each frequency of interest. The tissues used for these biomedical applications include blood, bone cortical, bone marrow, fat, muscle, and skin. The dielectric properties are acquired from [36] based on measured data. The dielectric properties for blood are shown in Table 2.1 through Table 2.5. The dielectric properties for bone cortical are shown in Table 2.6 through Table 2.10. The dielectric properties for bone marrow are shown in Table 2.11 through Table 2.15. The dielectric properties for fat are shown in Table 2.16 through Table 2.20. The dielectric properties for muscle are shown in Table 2.21 through Table 2.25. The dielectric properties for skin dry are shown in Table 2.26 through Table 2.30. The dielectric properties for the rest of the human tissues are shown in APPENDIX A.

Table 2.1 Dielectric Properties of Blood from 1 GHz to 5 GHz

Frequency [GHz]	Permittivity	Conductivity [S/m]
1	61.063	1.583
2	59.022	2.186
3	57.34	3.058
4	55.665	4.142
5	53.94	5.403

Table 2.2 Dielectric Properties of Blood from 5 GHz to 20 GHz

Frequency [GHz]	Permittivity	Conductivity [S/m]
5	53.94	5.403
6	52.175	6.802
7	50.389	8.303
8	48.605	9.876
9	46.839	11.493
10	45.107	13.133
11	43.421	14.777
12	41.774	16.425
13	40.201	18.036
14	38.692	19.617
15	37.249	21.16
16	35.873	22.66
17	34.562	24.115
18	33.316	25.522
19	32.133	26.88
20	31.011	28.189

Table 2.3 Dielectric Properties of Blood from 20 GHz to 30 GHz

Frequency [GHz]	Permittivity	Conductivity [S/m]
20	31.011	28.189
21	29.946	29.451
22	28.937	30.664
23	27.982	31.831
24	27.077	32.951
25	26.219	34.027
26	25.407	34.061
27	24.637	36.053
28	23.907	37.006
29	23.215	37.922
30	22.559	38.801

Table 2.4 Dielectric Properties of Blood from 30 GHz to 40 GHz

Frequency [GHz]	Permittivity	Conductivity [S/m]
30	22.559	38.801
31	21.936	39.647
32	21.344	40.46
33	20.781	41.241
34	20.246	41.994
35	19.738	42.718
36	19.253	43.415
37	18.792	44.087
38	18.352	44.735
39	17.933	45.36
40	17.533	45.963

Table 2.5 Dielectric Properties of Blood from 40 GHz to 90 GHz

Frequency [GHz]	Permittivity	Conductivity [S/m]
40	17.533	45.963
50	14.376	50.997
60	12.275	54.716
70	10.804	57.585
80	9.733	59.88
90	8.925	61.77

Table 2.6 Dielectric Properties of Bone Cortical from 1 GHz to 5 GHz

Frequency [GHz]	Permittivity	Conductivity [S/m]
1	12.363	0.156
2	11.654	0.310
3	11.061	0.508
4	10.528	0.729
5	10.037	0.964

Table 2.7 Dielectric Properties of Bone Cortical from 5 GHz to 20 GHz

Frequency [GHz]	Permittivity	Conductivity [S/m]
5	10.037	0.964
6	9.585	1.204
7	9.169	1.444
8	8.789	1.681
9	8.439	1.912
10	8.119	2.136
11	7.826	2.352
12	7.554	2.562
13	7.307	2.762
14	7.079	2.953
15	6.869	3.136
16	6.675	3.312
17	6.495	3.480
18	6.329	3.641
19	6.174	3.796
20	6.030	3.944

Table 2.8 Dielectric Properties of Bone Cortical from 20 GHz to 30 GHz

Frequency [GHz]	Permittivity	Conductivity [S/m]
20	6.030	3.944
21	5.896	4.087
22	5.771	4.223
23	5.653	4.355
24	5.544	4.481
25	5.441	4.603
26	5.344	4.720
27	5.253	4.833
28	5.167	4.943
29	5.086	5.048
30	5.010	5.150

Table 2.9 Dielectric Properties of Bone Cortical from 30 GHz to 40 GHz

Frequency [GHz]	Permittivity	Conductivity [S/m]
30	5.010	5.150
31	4.937	5.249
32	4.869	5.344
33	4.804	5.437
34	4.742	5.527
35	4.684	5.614
36	4.628	5.698
37	4.575	5.780
38	4.524	5.860
39	4.476	5.938
40	4.430	6.013

Table 2.10 Dielectric Properties of Bone Cortical from 40 GHz to 90 GHz

Frequency [GHz]	Permittivity	Conductivity [S/m]
40	4.430	6.013
50	4.062	6.674
60	3.810	7.206
70	3.628	7.649
80	3.491	8.028
90	3.384	8.360

Table 2.11 Dielectric Properties of Bone Marrow from 1 GHz to 5 GHz

Frequency [GHz]	Permittivity	Conductivity [S/m]
1	5.485	0.043
2	5.348	0.076
3	5.237	0.121
4	5.135	0.175
5	5.037	0.234

Table 2.12 Dielectric Properties of Bone Marrow from 5 GHz to 20 GHz

Frequency [GHz]	Permittivity	Conductivity [S/m]
5	5.037	0.234
6	4.944	0.298
7	4.854	0.366
8	4.768	0.436
9	4.685	0.506
10	4.607	0.578
11	4.532	0.650
12	4.460	0.721
13	4.393	0.792
14	4.329	0.861
15	4.268	0.930
16	4.210	0.997
17	4.155	1.063
18	4.102	1.127
19	4.053	1.190
20	4.005	1.252

Table 2.13 Dielectric Properties of Bone Marrow from 20 GHz to 30 GHz

Frequency [GHz]	Permittivity	Conductivity [S/m]
20	4.005	1.252
21	3.961	1.312
22	3.918	1.371
23	3.877	1.428
24	3.838	1.483
25	3.801	1.538
26	3.766	1.591
27	3.732	1.642
28	3.700	1.692
29	3.670	1.741
30	3.640	1.789

Table 2.14 Dielectric Properties of Bone Marrow from 30 GHz to 40 GHz

Frequency [GHz]	Permittivity	Conductivity [S/m]
30	3.640	1.789
31	3.612	1.835
32	3.585	1.881
33	3.560	1.925
34	3.535	1.968
35	3.511	2.010
36	3.489	2.051
37	3.467	2.092
38	3.446	2.131
39	3.426	2.169
40	3.406	2.207

Table 2.15 Dielectric Properties of Bone Marrow from 40 GHz to 90 GHz

Frequency [GHz]	Permittivity	Conductivity [S/m]
40	3.406	2.207
50	3.247	2.539
60	3.133	2.811
70	3.049	3.040
80	2.983	3.236
90	2.932	3.408

Table 2.16 Dielectric Properties of Fat from 1 GHz to 5 GHz

Frequency [GHz]	Permittivity	Conductivity [S/m]
1	5.447	0.054
2	5.328	0.086
3	5.223	0.130
4	5.124	0.183
5	5.029	0.243

Table 2.17 Dielectric Properties of Fat from 5 GHz to 20 GHz

Frequency [GHz]	Permittivity	Conductivity [S/m]
5	5.029	0.243
6	4.936	0.307
7	4.847	0.374
8	4.762	0.443
9	4.680	0.514
10	4.602	0.585
11	4.527	0.657
12	4.456	0.728
13	4.389	0.799
14	4.325	0.868
15	4.264	0.937
16	4.207	1.004
17	4.152	1.069
18	4.100	1.134
19	4.050	1.197
20	4.003	1.258

Table 2.18 Dielectric Properties of Fat from 20 GHz to 30 GHz

Frequency [GHz]	Permittivity	Conductivity [S/m]
20	4.003	1.258
21	3.958	1.318
22	3.916	1.377
23	3.875	1.434
24	3.836	1.489
25	3.799	1.543
26	3.764	1.596
27	3.731	1.648
28	3.699	1.698
29	3.668	1.747
30	3.639	1.794

Table 2.19 Dielectric Properties of Fat from 30 GHz to 40 GHz

Frequency [GHz]	Permittivity	Conductivity [S/m]
30	3.639	1.794
31	3.611	1.841
32	3.584	1.886
33	3.558	1.930
34	3.533	1.973
35	3.510	2.015
36	3.487	2.057
37	3.465	2.097
38	3.444	2.136
39	3.424	2.174
40	3.405	2.211

Table 2.20 Dielectric Properties of Fat from 40 GHz to 90 GHz

Frequency [GHz]	Permittivity	Conductivity [S/m]
40	3.405	2.211
50	3.246	2.543
60	3.132	2.815
70	3.048	3.044
80	2.982	3.240
90	2.931	3.411

Table 2.21 Dielectric Properties of Muscle from 1 GHz to 5 GHz

Frequency [GHz]	Permittivity	Conductivity [S/m]
1	54.810	0.978
2	53.290	1.454
3	52.048	2.148
4	50.812	3.022
5	49.532	4.051

Table 2.22 Dielectric Properties of Muscle from 5 GHz to 20 GHz

Frequency [GHz]	Permittivity	Conductivity [S/m]
5	49.532	4.051
6	48.211	5.208
7	46.860	6.466
8	45.493	7.802
9	44.123	9.195
10	42.762	10.627
11	41.419	12.083
12	40.090	13.562
13	38.805	15.027
14	37.557	16.481
15	36.348	17.918
16	35.181	19.331
17	34.058	20.716
18	32.978	22.070
19	31.943	23.390
20	30.951	24.673

Table 2.23 Dielectric Properties of Muscle from 20 GHz to 30 GHz

Frequency [GHz]	Permittivity	Conductivity [S/m]
20	30.951	24.673
21	30.000	25.921
22	29.092	27.131
23	28.224	28.303
24	27.395	29.437
25	26.603	30.534
26	25.848	31.595
27	25.127	32.619
28	24.440	33.609
29	23.783	34.565
30	23.157	35.487

Table 2.24 Dielectric Properties of Muscle from 30 GHz to 40 GHz

Frequency [GHz]	Permittivity	Conductivity [S/m]
30	23.157	35.487
31	22.559	36.379
32	21.988	37.239
33	21.442	38.070
34	20.921	38.873
35	20.423	39.649
36	19.947	40.398
37	19.492	41.123
38	19.056	41.823
39	18.639	42.501
40	18.239	43.156

Table 2.25 Dielectric Properties of Muscle from 40 GHz to 90 GHz

Frequency [GHz]	Permittivity	Conductivity [S/m]
40	18.239	43.156
50	15.037	48.688
60	12.856	52.826
70	11.308	56.036
80	10.169	58.606
90	9.304	60.721

Table 2.26 Dielectric Properties of Skin Dry from 1 GHz to 5 GHz

Frequency [GHz]	Permittivity	Conductivity [S/m]
1	40.934	0.900
2	38.568	1.265
3	37.443	1.745
4	36.582	2.345
5	35.769	3.066

Table 2.27 Dielectric Properties of Skin Dry from 5 GHz to 20 GHz

Frequency [GHz]	Permittivity	Conductivity [S/m]
5	35.769	3.066
6	34.942	3.896
7	34.08	4.821
8	33.181	5.827
9	32.248	6.897
10	31.289	8.015
11	30.313	9.166
12	29.319	10.346
13	28.335	11.523
14	27.358	12.695
15	26.396	13.853
16	25.454	14.990
17	24.536	16.100
18	23.647	17.178
19	22.788	18.220
20	21.962	19.224

Table 2.28 Dielectric Properties of Skin Dry from 20 GHz to 30 GHz

Frequency [GHz]	Permittivity	Conductivity [S/m]
20	21.962	19.224
21	21.168	20.190
22	20.409	21.114
23	19.684	21.998
24	18.993	22.841
25	18.335	23.644
26	17.709	24.408
27	17.115	25.134
28	16.552	25.824
29	16.017	26.478
30	15.510	27.099

Table 2.29 Dielectric Properties of Skin Dry from 30 GHz to 40 GHz

Frequency [GHz]	Permittivity	Conductivity [S/m]
30	15.510	27.099
31	15.029	27.688
32	14.573	28.246
33	14.142	28.776
34	13.732	29.278
35	13.345	29.755
36	12.977	30.207
37	12.628	30.636
38	12.297	31.043
39	11.983	31.429
40	11.685	31.797

Table 2.30 Dielectric Properties of Skin Dry from 40 GHz to 90 GHz

Frequency [GHz]	Permittivity	Conductivity [S/m]
40	11.685	31.797
50	9.402	34.619
60	7.975	36.397
70	7.038	37.577
80	6.395	38.397
90	5.936	38.989

2.1.2 Debye Parameters of Human Tissues

The next step for human tissue characterization is to determine the Debye expansion coefficients using the dielectric properties. The Debye model is shown in compact form in equation 2.1 where N is the number of Debye terms, ϵ_∞ is the permittivity at high frequency, $\Delta\epsilon_k$ is the pole weight, and τ_k is the relaxation time [33].

$$\epsilon_r(\omega) = \epsilon_\infty + \sum_{k=1}^{N} \frac{\Delta\epsilon_k}{1 + j\omega\tau_k}, \Delta\epsilon_k = A_k(\epsilon_s - \epsilon_\infty) \tag{2.1}$$

Equation 2.1 is used with the tissue parameters to calculate the Debye parameters. The relative permittivity and conductivity for each human tissue is used to calculate the complex permittivity by finding the real and imaginary parts of the permittivity given by equation 2.2. The necessary number of points are interpolated and the frequency transfer function of the complex permittivity is obtained and shown in equation 2.3 where N is the number of poles for the numerical fit and a_k and b_k are coefficients. The transfer function can then be used to determine the poles and weights for the Debye parameters in MATLAB using the "invfreqs" function [33].

$$\epsilon_r(\omega) = \epsilon' - j\epsilon'' \tag{2.2}$$

$$\epsilon_r(\omega) = \frac{\sum_{k=1}^{N} b_{k=1}\omega^{k=1}}{\sum_{k=1}^{N+1} a_{k=1}\omega^{k=1}} \tag{2.3}$$

The coefficients produced from the "invfreqs" function are then used to perform partial fraction expansion as shown in equation 2.4 using the "residues" function in MATLAB [33]. The residues, poles, and constant term produced are used to calculate the values of the Debye parameters. The ϵ_∞ is given by the constant term and the values of $\Delta\epsilon$ and τ are calcuated using the residues and poles [33]. The Debye parameters are then re-evaluated using equation 2.1 for comparison to ensure accurate fitting of the model as shown in Figure 2.1.

$$\epsilon_r(\omega) = R + \frac{r_N}{(j\omega) - p_N} + \frac{r_{N-1}}{(j\omega) - p_{N-1}} + ... + \frac{r_1}{(j\omega) - p_1} \tag{2.4}$$

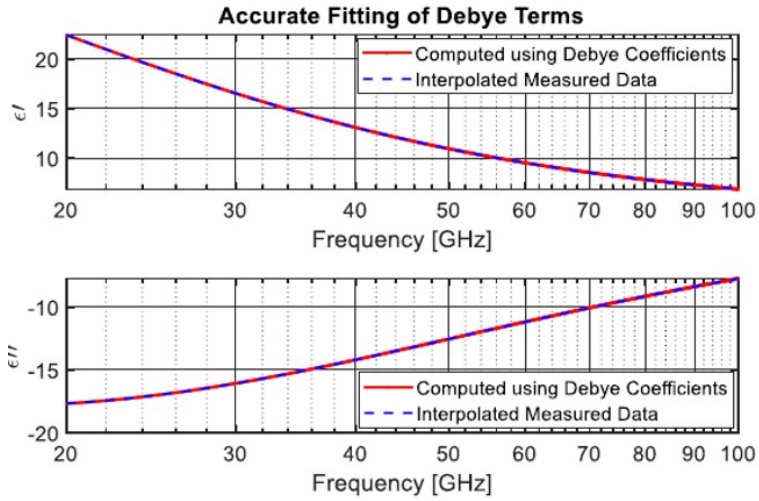

Figure 2.1 The Debye parameters based on measured data are compared to the computed parameters for the real and imaginary permittivity for the aorta tissue from 20 to 100 GHz [33].

Once accurate fitting is confirmed for all the tissues, the maximum percent error for the real and imaginary components of the complex permittivity is collected for each tissue. The final three-term Debye parameters and maximum real and imaginary errors are shown in Table 2.31 through Table 2.33 for all 55 human tissues from 100 MHz to 100 GHz [33].

Table 2.31 Debye Parameters from 100 MHz to 2 GHz

Tissue	ϵ_∞	$\Delta\epsilon_1$	$\Delta\epsilon_2$	$\Delta\epsilon_3$	$\tau_1[e^{-9}]$	$\tau_2[e^{-9}]$	$\tau_3[e^{-9}]$	Re[%]	Im[%]
Aorta	24.7	19.9	10.2	960.3	0.02478	0.7992	19.11	0.5126	1.252
Bladder	10.53	8.297	2.39	1690	0.02394	0.5471	51.4	0.3673	0.9379
Blood	33.1	27.87	9.087	6379	0.02375	0.5866	46.23	0.4125	0.8723
BloodVessel	24.7	19.9	10.27	960.3	0.02478	0.7992	19.11	0.5126	1.252
BodyFluid	4.242	64.77	0.04378	2107000	0.007269	0.6161	12410	0.002546	0.00754
BoneCancelllous	11.05	9.606	4.265	301.5	0.03801	0.485	15.79	0.5389	1.561
BoneCortical	6.915	5.487	1.653	94.31	0.03378	0.4537	13.19	0.3855	1.772
BoneMarrow	4.162	1.321	0.4162	26.08	0.02899	0.501	10.14	0.2234	1.35
BrainGreyMatter	31.79	20.03	14.85	638.5	0.03123	0.5744	10.24	0.6013	1.508
BrainWhiteMatter	23.68	14.57	9.495	323.1	0.03072	0.5444	8.889	0.5489	1.668
BreastFat	3.208	2.23	0.1457	253.3	0.0261	0.3441	75.37	0.1064	0.598
Cartilage	20.43	22.02	7.746	1135	0.03186	0.527	21.51	0.4988	1.123
Cerebellum	30.95	17.3	21.36	845.2	0.03889	0.6029	9.594	0.7802	1.319
CerebralFluid	33.52	34.97	34.48	121800	0.01843	1.426	534.2	0.1367	0.367
Cervix	27.08	22.46	5.644	3149	0.02201	0.5786	37.78	0.3488	0.931
Colon	34.76	22.32	15.12	1285	0.03087	0.5667	17.1	0.6	1.434
Cornea	33.11	21.43	13.5	3641	0.02986	0.5813	31.58	0.5909	1.136
Duodenum	34.71	30.03	7.386	4018	0.02195	0.5593	39.93	0.3374	0.958
Dura	26.41	17.83	7.700	1811	0.02735	0.6939	22.02	0.5037	1.049
EyeSclera	30.66	24.26	7.66	4343	0.0234	0.5725	42.95	0.3904	0.961
Fat	4.113	1.341	0.2853	119.3	0.02728	0.4887	29.28	0.1986	1.067
GallBladder	22.41	36.42	37.7	62890	0.01285	1.525	613.2	0.06222	0.286
GallBladderBile	25.98	43.81	47.27	130700	0.01282	1.53	821.2	0.06094	0.246
Gland	31.2	28.25	5.498	4707	0.0209	0.5381	52.9	0.2895	0.893
Heart	36.73	22.03	20.28	1181	0.03574	0.5659	14.65	0.71	1.473
Kidney	36.46	20.85	25.46	1099	0.04118	0.575	12.35	0.8162	1.515
Lens	25.09	21.28	4.771	2627	0.02135	0.5625	39.11	0.3106	0.938
Liver	27.45	18.57	14.11	698.6	0.03305	0.56	13.02	0.6477	1.525
LungDeflated	30.13	20.73	10.15	1379	0.02733	0.5585	22.28	0.4968	1.362
LungInflated	13.75	7.931	6.006	633	0.03199	0.5813	18.71	0.6173	1.337
Lymph	31.2	28.25	5.498	4707	0.0209	0.5381	52.9	0.2895	0.893
MucousMembrane	28.12	17.26	12.6	903.2	0.03132	0.5755	15.65	0.6096	1.458
Muscle	31.45	23.27	6.746	3101	0.02212	0.5729	39.26	0.3504	1.04
Nail	6.915	5.487	1.653	94.31	0.03378	0.4537	13.19	0.3855	1.772
Nerve	20.51	11.48	9.357	506.1	0.0333	0.5663	13.58	0.6227	1.513
Oesophagus	34.71	30.03	7.386	4018	0.02195	0.5593	39.93	0.3374	0.958
Ovary	30.42	19.03	23.32	999.7	0.04421	0.5884	12.12	0.8647	1.506
Pancreas	31.2	28.25	5.498	4707	0.0209	0.5381	52.9	0.2895	0.893
Prostate	33.7	26.43	9.073	3634	0.0239	0.5762	35.75	0.4115	1.036
Retina	30.66	24.26	7.66	4343	0.0234	0.5725	42.95	0.3904	0.961
SkinDry	27.44	12.73	17.1	417.9	0.0366	0.5684	7.581	0.7085	1.635
Skin	28.12	17.26	12.6	903.2	0.03132	0.5755	15.65	0.6096	1.458
SmallIntestine	37.16	21.26	23.62	5010	0.03722	0.6228	27.28	0.8121	1.002
SpinalCord	20.51	11.48	9.357	506.1	0.0333	0.5663	13.58	0.6227	1.513
Spleen	35.13	20.93	19.78	1163	0.03508	0.5828	13.11	0.7042	1.395
Stomach	34.71	30.03	7.386	4018	0.02195	0.5593	39.93	0.3374	0.958
Tendon	19.2	26.69	3.937	1733	0.02353	0.5869	31.6	0.3248	0.880
Testis	33.7	26.43	9.073	3634	0.0239	0.5762	35.75	0.4115	1.036
Thymus	31.2	28.25	5.498	4707	0.0209	0.5381	52.9	0.2895	0.893
Thyroid	31.2	28.25	5.498	4707	0.0209	0.5381	52.9	0.2895	0.893
Tongue	30.57	24.34	7.567	2354	0.02328	0.5664	31.32	0.3824	1.099
Tooth	6.915	5.487	1.653	94.31	0.03378	0.4537	13.19	0.3855	1.772
Trachea	23.68	17.97	6.957	1897	0.02526	0.5573	31.12	0.4453	1.177
Uterus	34.76	25.81	10.72	2891	0.02542	0.5807	27.5	0.4648	1.105
VitreousHumor	4.242	64.77	0.04378	2107000	0.007269	0.6161	12410	0.002546	0.0075

Table 2.32 Debye Parameters from 2 GHz to 20 GHz

Tissue	ϵ_∞	$\Delta\epsilon_1$	$\Delta\epsilon_2$	$\Delta\epsilon_3$	$\tau_1[e^{-9}]$	$\tau_2[e^{-9}]$	$\tau_3[e^{-9}]$	Re[%]	Im[%]
Aorta	5.819	26.080	11.258	53.960	0.007	0.018	0.709	0.116	1.396
Bladder	3.247	10.599	4.413	41.039	0.007	0.019	0.967	0.121	1.230
Blood	6.713	37.992	14.367	201.858	0.007	0.018	1.183	0.124	1.099
BloodVessel	5.819	26.080	11.258	53.960	0.007	0.018	0.709	0.116	1.396
BodyFluid	-91950	91950	64.974	2.1e8	0.000	0.007	1.2e6	0.004	0.004
BoneCancelllous	3.896	7.689	7.343	14.049	0.007	0.024	0.319	0.222	2.040
BoneCortical	3.176	4.255	4.161	4.913	0.007	0.023	0.261	0.176	2.096
BoneMarrow	2.793	1.660	0.872	1.759	0.006	0.020	0.355	0.092	2.274
BrainGreyMatter	6.384	32.024	10.792	59.363	0.007	0.019	0.532	0.135	1.558
BrainWhiteMatter	5.728	22.838	7.788	32.142	0.007	0.019	0.452	0.130	1.680
BreastFat	2.576	1.049	1.703	2.698	0.010	0.023	0.556	0.085	1.226
Cartilage	5.932	17.545	16.476	43.234	0.008	0.022	0.479	0.193	1.642
Cerebellum	6.237	29.242	9.442	93.588	0.007	0.021	0.618	0.159	1.366
CerebralFluid	7.169	44.000	16.091	708.896	0.007	0.017	2.688	0.103	0.690
Cervix	6.253	31.035	10.926	106.461	0.007	0.018	1.009	0.113	1.246
Colon	6.660	35.631	11.957	72.886	0.007	0.019	0.574	0.138	1.535
Cornea	6.552	34.203	11.316	139.747	0.007	0.019	0.874	0.140	1.252
Duodenum	6.999	41.358	14.592	119.872	0.007	0.018	0.918	0.115	1.309
Dura	6.996	24.648	10.924	95.339	0.006	0.019	0.878	0.148	1.453
EyeSclera	6.527	34.692	12.042	130.552	0.007	0.018	1.007	0.119	1.226
Fat	2.796	1.666	0.858	3.261	0.006	0.020	0.548	0.096	2.026
GallBladder	5.354	43.362	9.641	351.276	0.007	0.015	2.663	0.052	0.541
GallBladderBile	5.626	52.059	11.543	642.375	0.007	0.015	3.285	0.053	0.468
Gland	6.736	37.787	13.432	106.528	0.007	0.018	0.940	0.112	1.317
Heart	6.771	36.303	11.957	78.334	0.007	0.020	0.527	0.153	1.555
Kidney	6.720	34.780	11.305	89.380	0.007	0.021	0.523	0.169	1.502
Lens	6.086	28.850	10.254	79.431	0.007	0.018	0.915	0.110	1.318
Liver	5.927	26.720	10.724	50.459	0.007	0.020	0.494	0.146	1.571
LungDeflated	6.331	31.639	10.839	59.528	0.007	0.019	0.603	0.127	1.543
LungInflated	3.464	12.883	4.264	35.470	0.007	0.019	0.664	0.136	1.420
Lymph	6.736	37.787	13.432	106.528	0.007	0.018	0.940	0.112	1.317
MucousMembrane	6.060	27.752	9.311	56.367	0.007	0.019	0.567	0.135	1.528
Muscle	6.706	35.825	10.710	92.328	0.006	0.017	0.884	0.108	1.356
Nail	3.176	4.255	4.161	4.913	0.007	0.023	0.261	0.176	2.096
Nerve	5.401	18.661	6.223	35.601	0.007	0.020	0.518	0.134	1.578
Oesophagus	6.999	41.358	14.592	119.872	0.007	0.018	0.918	0.115	1.309
Ovary	7.079	25.127	12.690	79.958	0.007	0.022	0.499	0.208	1.622
Pancreas	6.736	37.787	13.432	106.528	0.007	0.018	0.940	0.112	1.317
Prostate	6.782	38.191	13.251	122.390	0.007	0.018	0.908	0.120	1.287
Retina	6.527	34.692	12.042	130.552	0.007	0.018	1.007	0.119	1.226
SkinDry	4.124	32.553	1.934	82.391	0.007	0.048	0.854	0.039	0.250
Skin	6.060	27.752	9.311	56.367	0.007	0.019	0.567	0.135	1.528
SmallIntestine	6.768	36.417	11.573	252.957	0.007	0.020	1.006	0.162	1.063
SpinalCord	5.401	18.661	6.223	35.601	0.007	0.020	0.518	0.134	1.578
Spleen	6.624	34.695	11.376	90.449	0.007	0.020	0.597	0.150	1.455
Stomach	6.999	41.358	14.592	119.872	0.007	0.018	0.918	0.115	1.309
Tendon	5.446	21.617	17.416	53.271	0.008	0.020	0.712	0.134	1.314
Testis	6.782	38.191	13.251	122.390	0.007	0.018	0.908	0.120	1.287
Thymus	6.736	37.787	13.432	106.528	0.007	0.018	0.940	0.112	1.317
Thyroid	6.736	37.787	13.432	106.528	0.007	0.018	0.940	0.112	1.317
Tongue	6.512	34.588	12.139	81.015	0.007	0.018	0.779	0.116	1.400
Tooth	3.176	4.255	4.161	4.913	0.007	0.023	0.261	0.176	2.096
Trachea	4.449	26.562	9.147	64.550	0.007	0.018	0.742	0.126	1.420
Uterus	6.818	38.444	13.181	123.441	0.007	0.018	0.864	0.125	1.302
VitreousHumor	-91950	91950	64.974	2.1e8	0.000	0.007	1.2e6	0.004	0.004

Table 2.33 Debye Parameters from 20 GHz to 100 GHz

Tissue	ϵ_∞	$\Delta\epsilon_1$	$\Delta\epsilon_2$	$\Delta\epsilon_3$	$\tau_1[e^{-9}]$	$\tau_2[e^{-9}]$	$\tau_3[e^{-9}]$	Re[%]	Im[%]
Aorta	4.325	2.311	20.134	19.363	0.002	0.006	0.017	0.068	0.127
Bladder	2.635	0.969	8.610	7.917	0.002	0.006	0.019	0.063	0.122
Blood	4.498	3.684	32.111	26.674	0.002	0.006	0.021	0.079	0.126
BloodVessel	4.325	2.311	20.134	19.363	0.002	0.006	0.017	0.068	0.127
BodyFluid	3.999	32.423	32.423	21010	0.007	0.007	116.700	0.009	5.1e-3
BoneCancelllous	2.817	1.411	4.954	11.316	0.001	0.006	0.021	0.084	0.212
BoneCortical	2.647	0.695	2.683	6.163	0.001	0.006	0.019	0.060	0.190
BoneMarrow	2.565	0.335	1.158	1.407	0.001	0.005	0.016	0.032	0.261
BrainGreyMatter	4.428	3.123	25.887	20.355	0.002	0.006	0.019	0.073	0.141
BrainWhiteMatter	4.315	2.212	18.093	14.502	0.002	0.006	0.018	0.068	0.146
BreastFat	2.513	0.074	0.555	2.391	0.002	0.007	0.021	0.016	0.062
Cartilage	4.371	2.030	11.251	25.934	0.001	0.006	0.020	0.084	0.132
Cerebellum	4.403	2.954	24.443	20.383	0.002	0.006	0.023	0.078	0.124
CerebralFluid	4.614	4.717	39.895	31.694	0.002	0.006	0.024	0.084	0.119
Cervix	4.410	3.058	25.632	19.530	0.002	0.006	0.018	0.073	0.139
Colon	4.477	3.485	28.886	22.688	0.002	0.006	0.019	0.075	0.139
Cornea	4.465	3.452	28.828	22.807	0.002	0.006	0.022	0.078	0.129
Duodenum	4.542	4.036	33.756	25.919	0.002	0.006	0.018	0.075	0.142
Dura	4.602	3.754	19.037	19.513	0.001	0.006	0.019	0.087	0.207
EyeSclera	4.460	3.447	28.933	22.031	0.002	0.006	0.019	0.075	0.137
Fat	2.566	0.339	1.182	1.424	0.001	0.005	0.017	0.034	0.271
GallBladder	4.246	2.373	42.606	16.075	0.002	0.007	0.024	0.049	0.057
Gland	4.494	3.673	30.674	23.645	0.002	0.006	0.017	0.073	0.143
Heart	4.499	3.591	29.594	23.813	0.002	0.006	0.020	0.078	0.136
Kidney	4.491	3.497	28.628	24.139	0.002	0.006	0.022	0.080	0.128
Lens	4.376	2.803	23.427	18.053	0.002	0.006	0.017	0.070	0.143
Liver	4.345	2.401	20.938	20.001	0.002	0.006	0.019	0.073	0.125
LungDeflated	4.418	3.061	25.394	19.870	0.002	0.006	0.018	0.072	0.141
LungInflated	2.674	1.279	10.640	8.385	0.002	0.006	0.020	0.067	0.135
Lymph	4.494	3.673	30.674	23.645	0.002	0.006	0.017	0.073	0.143
MucousMembrane	4.368	2.711	22.538	17.662	0.002	0.006	0.019	0.072	0.141
Muscle	4.490	3.793	29.742	19.355	0.002	0.006	0.017	0.071	0.157
Nail	2.647	0.695	2.683	6.163	0.001	0.006	0.019	0.060	0.190
Nerve	4.251	1.827	15.117	11.972	0.002	0.006	0.019	0.067	0.135
Oesophagus	4.542	4.036	33.756	25.919	0.002	0.006	0.018	0.075	0.142
Ovary	4.618	3.608	19.036	24.768	0.002	0.006	0.022	0.095	0.181
Pancreas	4.494	3.673	30.674	23.645	0.002	0.006	0.017	0.073	0.143
Prostate	4.504	3.766	31.554	24.101	0.002	0.006	0.019	0.075	0.139
Retina	4.460	3.447	28.933	22.031	0.002	0.006	0.019	0.075	0.137
SkinDry	4.030	0.125	32.419	22.833	0.001	0.007	0.161	0.008	0.008
Skin	4.368	2.711	22.538	17.662	0.002	0.006	0.019	0.072	0.141
SmallIntestine	4.506	3.796	31.520	28.688	0.002	0.006	0.027	0.083	0.106
SpinalCord	4.251	1.827	15.117	11.972	0.002	0.006	0.019	0.067	0.135
Spleen	4.472	3.454	28.636	22.944	0.002	0.006	0.021	0.078	0.132
Stomach	4.542	4.036	33.756	25.919	0.002	0.006	0.018	0.075	0.142
Tendon	4.251	1.611	14.119	27.539	0.002	0.007	0.018	0.068	0.090
Testis	4.504	3.766	31.554	24.101	0.002	0.006	0.019	0.075	0.139
Thymus	4.494	3.673	30.674	23.645	0.002	0.006	0.017	0.073	0.143
Thyroid	4.494	3.673	30.674	23.645	0.002	0.006	0.017	0.073	0.143
Tongue	4.451	3.348	27.925	21.646	0.002	0.006	0.017	0.072	0.144
Tooth	2.647	0.695	2.683	6.163	0.001	0.006	0.019	0.060	0.190
Trachea	2.851	2.590	21.581	16.693	0.002	0.006	0.018	0.077	0.143
Uterus	4.511	3.804	31.844	24.425	0.002	0.006	0.019	0.076	0.138
VitreousHumor	2.603	18.869	74.775	-11802	0.004	0.014	5.215	3.047	3.958

2.2 Human Tissue Discretization

Once the dielectric properties and Debye parameters have been determined, the next step requires discretization of the tissues in the computational domain. This methodology for the human tissue model can be used for various biomedical applications.

The specific application used to illustrate this discretization is a wrist phantom model that consists of skin, fat, muscle, blood, bone cortical, and bone marrow. The three-term Debye parameters are used from Table 2.32 in the dispersive FDTD method [35].

2.2.1 Image Processing

The tissue model is based on a 3D voxel volume model from [32] that uses the colormap command in MATLAB. The image source is an MRI image of the cross-section of a human wrist. The MRI 3D model is accessed using an online database and is imported into MATLAB [35]. The 3D model is first evaluated as a 2D cross section for optimal cell resolution and model accuracy. The cell resolution is assigned using the number of cells in the x, y, and z coordinates. The image cells corresponding to each tissue are assigned a value which corresponds to colors based on the appropriate RGB values as shown in Figure 2.2. The image resolution shown is 2 mm per cell. The images are processed for both the horizontal cross section in the x-y plane as well as the vertical cross section in the x-z plane as shown in Figure 2.3.

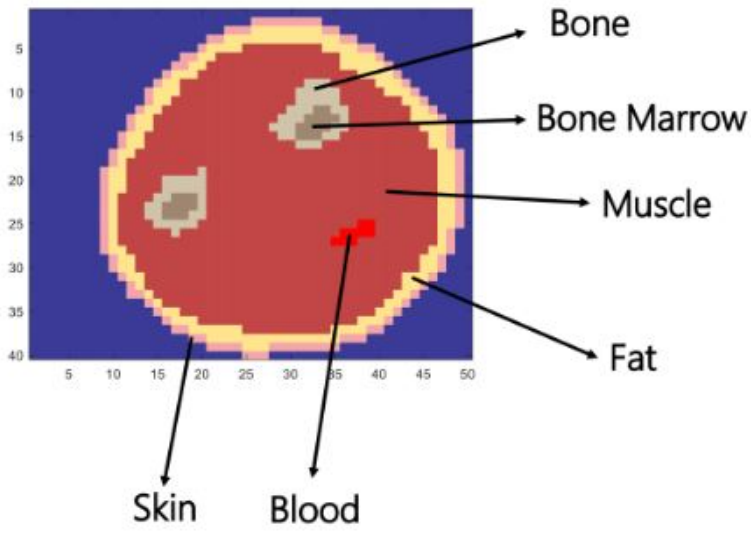

Figure 2.2 Wrist image at 2 mm resolution labeled with the corresponding human tissues [35].

The images are also analyzed using 3.6 mm resolution per cell for comparison. The same procedure is used to assign the cells for each tissue to a value that then is used with colormap to assign the colors. As expected, the detail is much less defined for the tissues as shown in Figure 2.4. The 2 mm resolution model

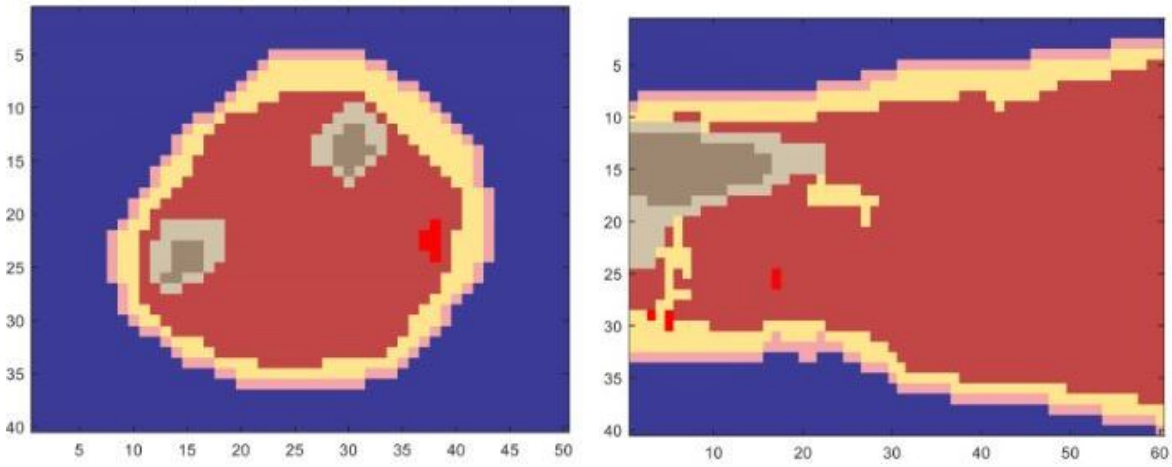

(a) Horizontal Cross Section (b) Vertical Cross Section

Figure 2.3 Wrist images using 2 mm resolution of male voxel model (a) Horizontal Cross Section of x-y plane. (b) Vertical Cross Section of x-z plane [35].

is more useful for biomedical applications requiring fine detail of the cells to detect cancer tissue and other abnormalities. Further resolutions of 0.5 mm are achieved with this model for FDTD formulations [35]. The 3D voxel model is imported into the computational electromagnetics simulator (CEMS) as a series of layers of tissues of cells. The Debye parameters of the human tissues are entered into the model for the frequency range of 20 to 100 GHz. The model is successfully run for 7000 time steps at this resolution of x = 0.5 mm, y = 0.5 mm, and z = 0.5mm for a dual-band textile antenna model at 2.4 and 5.8 GHz in [35] with the wrist model shown in Figure 2.5.

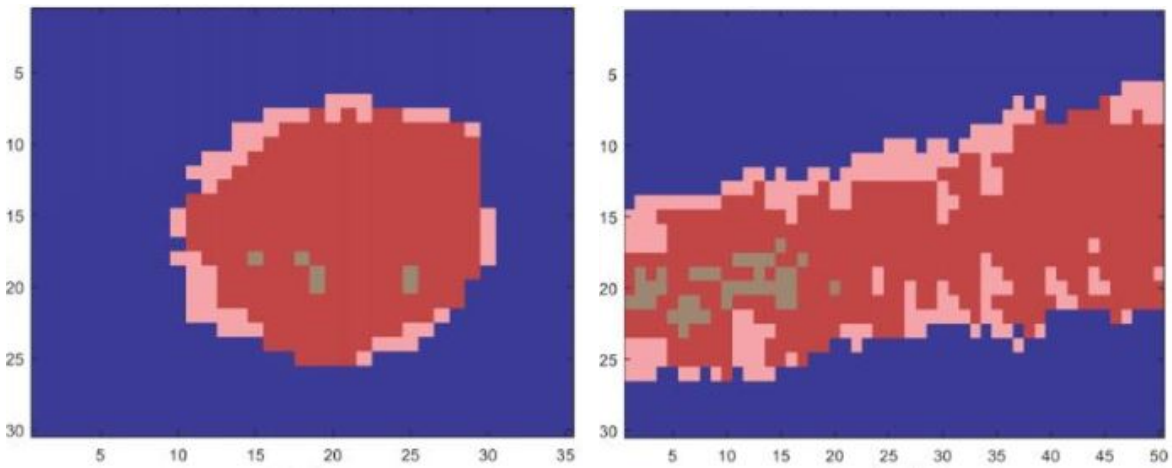

(a) Horizontal Cross Section (b) Vertical Cross Section

Figure 2.4 Wrist images using 3.6 mm resolution of male voxel model (a) Horizontal Cross Section of x-y plane. (b) Vertical Cross Section of x-z plane [35].

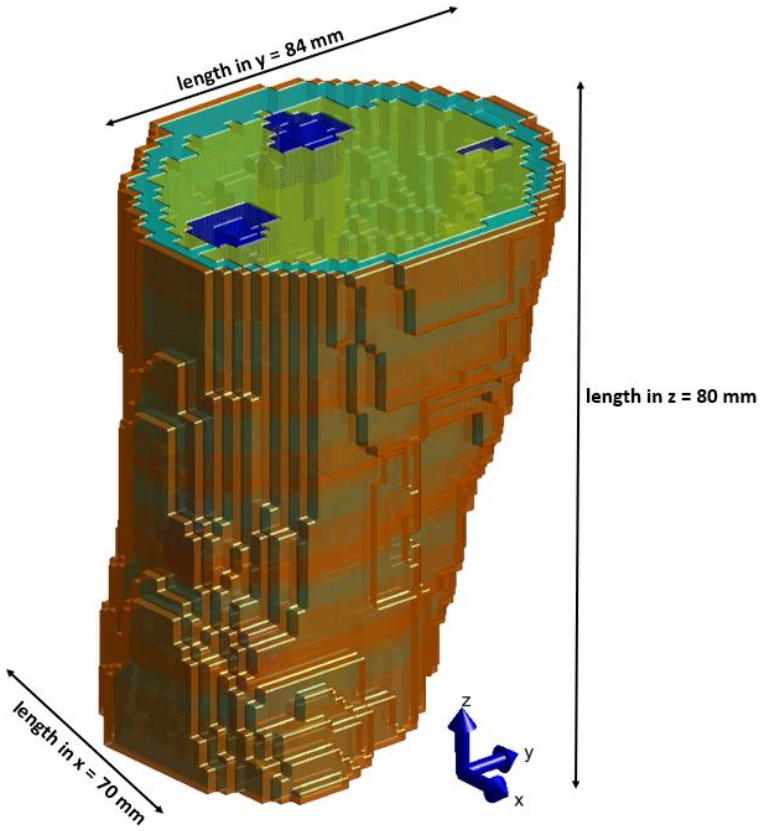

Figure 2.5 The CEMS 3D human wrist model with the general dimensions in mm.

This application demonstrates how the human tissue MRI image can be set up using the tissue parameters in the computational domain with specific resolution for further analysis with 2D or 3D FDTD programs. Please see APPENDIX B for the MATLAB code for the 2 mm resolution of the x-z plane.

CHAPTER 3

2D FDTD BIOMEDICAL APPLICATIONS

The FDTD formulation requires an understanding of the Yee grid of the electromagnetic field components and materials within the domain [37]. A Yee grid is used for FDTD simulations to discretize the domain with Yee cells that designates the field and material components for 2D and 3D simulations as shown in Figure 3.1.

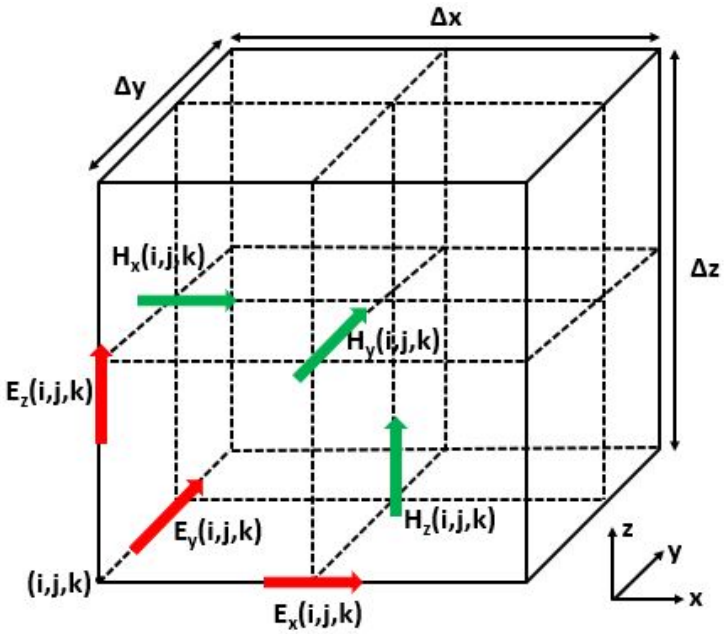

Figure 3.1 The Yee grid for the E-field and H-field components based on formulation described in [37].

3.1 Maxwell's Equations

The best place to start when describing electromagnetic solvers such as FDTD is Maxwell's equations. For computational electromagnetics, they are solved by using approximations to the exact formulation. Equations 3.1, 3.2, 3.3, and 3.4 show Maxwell's equations in the time domain where $\vec{H}$ is the magnetic field strength vector, $\vec{D}$ is the electric displacement vector in [C/m], $\vec{J}$ is the electric current density in [A/m^2], $\vec{E}$ is the electric field vector in [V/m], $\vec{B}$ is the magnetic flux density vector in [T], $\vec{M}$ is the magnetic current density vector in [V/m^2], ρ_e is the electric charge density, and ρ_m is the virtual magnetic charge density. Equations 3.5 and 3.6 show the relations used for how electromagnetic fields penetrate certain mediums where ϵ is the permittivity and μ is the permeability of the material.

$$\nabla \times \vec{H} = \frac{\partial \vec{D}}{\partial t} + \vec{J} \tag{3.1}$$

$$\nabla \times \vec{E} = -\frac{\partial \vec{B}}{\partial t} + \vec{M} \tag{3.2}$$

$$\nabla \cdot \vec{D} = \rho_e \tag{3.3}$$

$$\nabla \cdot \vec{B} = \rho_m \tag{3.4}$$

$$\vec{D} = \epsilon \vec{E} \tag{3.5}$$

$$\vec{B} = \mu \vec{H} \tag{3.6}$$

Maxwell's equations are then applied in the FDTD method in component form from vector form using equations 3.7 through 3.12, calculus-based derivative approximations can then be applied with a computational domain discretized with the necessary number of cells to achieve accurate response of the fields.

$$\frac{\partial E_x}{\partial t} = \frac{1}{\epsilon_x}\left(\frac{\partial H_z}{\partial y} - \frac{\partial H_y}{\partial z} - \sigma_x^e E_x - J_{i_x}\right) \tag{3.7}$$

$$\frac{\partial E_y}{\partial t} = \frac{1}{\epsilon_y}\left(\frac{\partial H_x}{\partial z} - \frac{\partial H_z}{\partial x} - \sigma_y^e E_y - J_{i_y}\right) \tag{3.8}$$

$$\frac{\partial E_z}{\partial t} = \frac{1}{\epsilon_z}\left(\frac{\partial H_y}{\partial x} - \frac{\partial H_x}{\partial y} - \sigma_z^e E_z - J_{i_z}\right) \tag{3.9}$$

$$\frac{\partial H_x}{\partial t} = \frac{1}{\mu_x}\left(\frac{\partial E_y}{\partial z} - \frac{\partial E_z}{\partial y} - \sigma_x^m H_x - M_{i_x}\right) \tag{3.10}$$

$$\frac{\partial H_y}{\partial t} = \frac{1}{\mu_y}\left(\frac{\partial E_z}{\partial x} - \frac{\partial E_x}{\partial z} - \sigma_y^m H_y - M_{i_y}\right) \tag{3.11}$$

$$\frac{\partial H_z}{\partial t} = \frac{1}{\mu_z}(\frac{\partial E_x}{\partial y} - \frac{\partial E_y}{\partial x} - \sigma_z^m H_z - M_{i_z}) \tag{3.12}$$

The equations for FDTD are applied to the 2D case by simplifying for no variation in the z direction. This means the derivative with respect to z is 0. In addition, the equations can be applied for either the transverse electric (TE) or transverse magnetic (TM) wave propagation cases. In this case, TM propagation is used where the magnetic field is perpendicular to the incident wave. Thus, the E_z, H_x, and H_y fields are solved using the updating equations shown in 3.13 through 3.15.

$$\epsilon_z \frac{\partial E_z}{\partial t} + \sigma_z^e \times E_z = \frac{\partial H_y}{\partial x} - \frac{\partial H_x}{\partial y} \tag{3.13}$$

$$\mu_x \frac{\partial H_x}{\partial t} + \sigma_x^m \times H_x = -\frac{\partial E_z}{\partial y} \tag{3.14}$$

$$\mu_y \frac{\partial H_y}{\partial t} + \sigma_y^m \times H_y = \frac{\partial E_z}{\partial x} \tag{3.15}$$

3.2 Advantages of FDTD

The FDTD method is useful for solving Maxwell's equations because it applies a complete time domain solution to a wide frequency range in a single run. Some solvers apply Maxwell's equations using the frequency domain, which requires less computational resources, however, they only solve for one frequency per simulation. This is the case for the finite-difference frequency-domain (FDFD) or the commonly used method of moments (MoM) formulation. Since FDTD uses the time domain, only one simulation is required to compute at all time steps the field components' responses, which are converted to the frequency domain using a Fourier transform at the target frequencies [1].

3.3 FDTD Approximations

In order to solve Maxwell's equations in the computational domain, a numerical technique must be applied to solve the differential equations using approximations. Finite difference can be used to approximate the numerical derivatives. The derivations can be formulated to be accurate up to second order with a minimal error rate [37].

The approximation for the derivative is based on the Taylor series expansion for a point x with spacing Δx. The approximation for the FDTD central difference After simplifying the Taylor series terms, the general second order approximation is given in equation 3.16 [37].

$$f'(x) \approx \frac{f(x + \Delta x - f(x - \Delta x)}{2\Delta x} \tag{3.16}$$

Applying the second order derivative approximation to FDTD analysis, the Taylor series is calculated for each point [37]. It is used for the space and time derivatives. The finite differences can then be used to

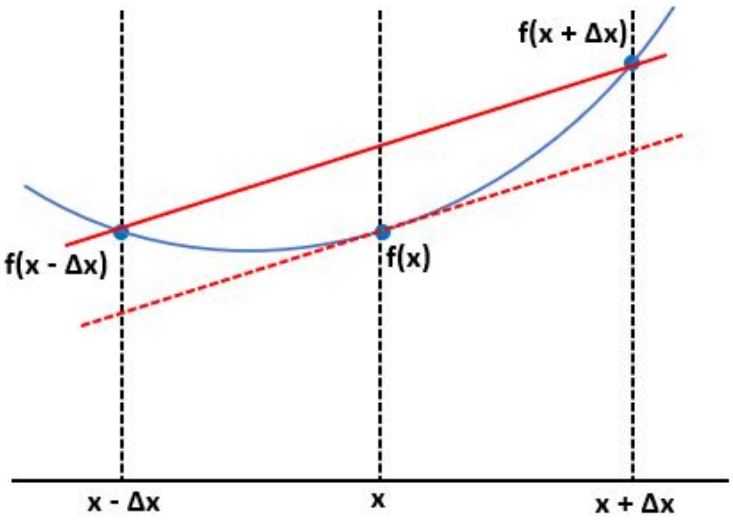

Figure 3.2 The approximation for the FDTD central difference based on the Taylor series for a point centered at x with spacing Δx as described in [37].

formulate the 6 FDTD updating equations for the 3D electric and magnetic fields shown in equations 3.17 through 3.22. Note that the coefficients such as C_{exe} represent the compact form of the updating equations. For more details, please see chapter 1 in [1].

$$\begin{aligned} E_x^{n+1}(i,j,k) = C_{exe}(i,j,k)E_x^n(i,j,k) + C_{exhz}(i,j,k)(H_z^{n+\frac{1}{2}}(i,j,k) - H_z^{n+\frac{1}{2}}(i,j-1,k)) \\ + C_{exhy}(i,j,k)(H_y^{n+\frac{1}{2}}(i,j,k) - H_y^{n+\frac{1}{2}}(i,j,k-1)) + C_{exj}(i,j,k)J_{ix}^{n+\frac{1}{2}}(i,j,k) \end{aligned} \tag{3.17}$$

$$\begin{aligned} E_y^{n+1}(i,j,k) = C_{eye}(i,j,k)E_y^n(i,j,k) + C_{eyhx}(i,j,k)(H_x^{n+\frac{1}{2}}(i,j,k) - H_x^{n+\frac{1}{2}}(i,j,k-1)) \\ + C_{eyhz}(i,j,k)(H_z^{n+\frac{1}{2}}(i,j,k) - H_z^{n+\frac{1}{2}}(i-1,j,k)) + C_{eyj}(i,j,k)J_{iy}^{n+\frac{1}{2}}(i,j,k) \end{aligned} \tag{3.18}$$

$$\begin{aligned} E_z^{n+1}(i,j,k) = C_{eze}(i,j,k)E_z^n(i,j,k) + C_{ezhy}(i,j,k)(H_y^{n+\frac{1}{2}}(i,j,k) - H_y^{n+\frac{1}{2}}(i-1,j,k)) \\ + C_{ezhx}(i,j,k)(H_x^{n+\frac{1}{2}}(i,j,k) - H_x^{n+\frac{1}{2}}(i,j-1,k)) + C_{ezj}(i,j,k)J_{iz}^{n+\frac{1}{2}}(i,j,k) \end{aligned} \tag{3.19}$$

$$\begin{aligned} H_x^{n+\frac{1}{2}}(i,j,k) = C_{hxh}(i,j,k)H_x^{n-\frac{1}{2}}(i,j,k) + C_{hxey}(i,j,k)(E_y^n(i,j,k+1) - E_y^n(i,j,k)) \\ + C_{hxez}(i,j,k)(E_z^n(i,j+1,k) - E_z^n(i,j,k)) + C_{hxm}(i,j,k)M_{ix}^n(i,j,k) \end{aligned} \tag{3.20}$$

$$\begin{aligned} H_y^{n+\frac{1}{2}}(i,j,k) = C_{hyh}(i,j,k)H_y^{n-\frac{1}{2}}(i,j,k) + C_{hyez}(i,j,k)(E_z^n(i+1,j,k) - E_z^n(i,j,k)) \\ + C_{hyex}(i,j,k)(E_x^n(i,j,k+1) - E_x^n(i,j,k)) + C_{hym}(i,j,k)M_{iy}^n(i,j,k) \end{aligned} \tag{3.21}$$

$$\begin{aligned} H_z^{n+\frac{1}{2}}(i,j,k) = C_{hzh}(i,j,k)H_z^{n-\frac{1}{2}}(i,j,k) + C_{hzex}(i,j,k)(E_x^n(i,j+1,k) - E_x^n(i,j,k)) \\ + C_{hzey}(i,j,k)(E_y^n(i+1,j,k) - E_y^n(i,j,k)) + C_{hzm}(i,j,k)M_{iz}^n(i,j,k) \end{aligned} \tag{3.22}$$

The updating equations are applied to the 2D case for TM wave propagation for the E_z, H_x, and H_y fields as shown in 3.23 through 3.25.

$$\begin{aligned} E_z^{n+1}(i,j,k) = C_{eze}(m)E_z^n(i,j,k) + C_{ezhy}(m)(H_y^{n+\frac{1}{2}}(i,j,k) - H_y^{n+\frac{1}{2}}(i-1,j,k)) \\ -C_{ezhx}(m)(H_x^{n+\frac{1}{2}}(i,j,k) - H_x^{n+\frac{1}{2}}(i,j-1,k)) - C_{ezj}(m)J_{zi}^{n+\frac{1}{2}}(i,j,k) \end{aligned} \tag{3.23}$$

$$\begin{aligned} H_x^{n+\frac{1}{2}}(i,j,k) = C_{hxh}(m)H_x^{n-\frac{1}{2}}(i,j,k) + C_{hxey}(m)(E_y^n(i,j,k+1) - E_y^n(i,j,k)) \\ -C_{hxez}(m)(E_z^n(i,j+1,k) - E_z^n(i,j,k)) - C_{hxm}(m)M_{xi}^n(i,j,k) \end{aligned} \tag{3.24}$$

$$\begin{aligned} H_y^{n+\frac{1}{2}}(i,j,k) = C_{hyh}(m)sH_y^{n-\frac{1}{2}}(i,j,k) + C_{hyez}(m)(E_z^n(i+1,j,k) - E_z^n(i,j,k)) \\ -C_{hyex}(m)(E_x^n(i,j,k+1) - E_x^n(i,j,k)) - C_{hym}(m)M_{yi}^n(i,j,k) \end{aligned} \tag{3.25}$$

3.4 Wireless Charging Application - 2D Model

In recent years, the focus of many 5G applications has been centered around wearable, miniaturized biomedical devices that can be wirelessly charged for efficient utilization. Such devices would allow healthcare providers to monitor their patients' health remotely, even from home. This technology could be life changing for patients suffering from chronic diseases and provide a means of reducing the physical and economic burden placed on hospitals. This research usually involves the analysis using human tissue parameters or their approximation. At high frequencies, the accurate analysis of the depth of wave penetration in such frequency dependent tissues is challenging.

In this work, we present a numerical solution for focusing the fields due to an incident electromagnetic wave on a group of dielectric cylinders positioned above a medium comprised of parallel layers characterized as human tissues using the FDTD technique [1]. The analysis is conducted at two 5G frequencies, namely, 28 GHz and 29 GHz. A similar model is used in [27] but at 24 GHz for wireless charging applications for biomedical devices. In [27] a different configuration for the cylinders and a different methodology for the solution based on a much more complex analytical solution for a fixed configuration is presented. This reported method is not easy to adapt for different configurations as wearable antennas are changing in shape over time based on applications. Thus, the use of a FDTD method with accurate tissue parameters would be much more practical for such applications. The results based on the FDTD method with the optimized configuration of the cylinders and their properties along with the proper tissue parameters at higher frequencies show a gain of 8 dB of focused electric field which is a 2 dB enhancement over reported data for charging wearable sensors and antennas [27].

The model analyzed here is composed of a multi-layered medium to solve for the E-field that is focused above and within the first layer [27]. The medium consists of cotton, skin, fat, and muscle layers. The layers are assigned their dielectric properties consisting of the relative permittivity and electric conductivity that depend on the frequency of interest shown in Table 3.1, which are based on the work

reported in [33]. The dielectric cylinders are assigned relative permittivities that range from 2 to 10 with the most dielectric constant cylinder at the center. The tapered distribution of the dielectric constant is considered for enhancing the focusing gain. The cylinders are identified by the letters "a" to "g" with the center cylinder identified as cylinder "d". The radius of cylinder "d" is 0.4 mm and its center is located at (0.4,0). The radius of cylinders "c" and "e" is 0.3 mm. The radius of cylinders "b" and "f" is 0.2 mm. The radius of cylinders "a" and "g" is 0.1 mm. The total width of the cylinders is $x = 3.2$ mm and the length is $y = 20$ mm. Again, the tapered radius of cylinders helps in focusing the field along the negative x direction. All cylinders are positioned such that they are touching each other and touching the y axis which is the first boundary of the cotton layer. The source of the electromagnetic field is a line source positioned along the x axis with $x = 3$ mm and radiates a cylindrical wave towards the multi-layer tissue structure. The radiated E-field is solved using the FDTD method for TM wave propagation and the frequency domain values of the E field are computed at 28 GHz and 29 GHz. These frequencies are chosen to support one of the upper bands for 5G of n257 and n261 bands [2]. The dielectric properties consisting of the relative permittivity and electrical conductivity are entered for each human tissue at 28 and 29 GHz, respectively. Thus, each simulation is run at the target frequency of either 28 or 29 GHz depending on the human tissue model. The FDTD simulations are performed with a cell resolution of x and $y = 0.02$ mm to provide the necessary cells per wavelength. For an approximate frequency of 30 GHz and relative permittivity of 25, this is 2 mm for the wavelength. Thus, this resolution allows for approximately 100 cells per wavelength in the x and y planes. The smallest radius of the cylinders is 0.1 mm which allows for 10 cells across the diameter. Thus, all cylinders are accounted for in the model for this resolution. The source waveform is selected to support the desired frequencies of interest. Each simulation is executed for 4,000 time steps to ensure sufficient decay of the energy injected in the system. The resulting E-field is sampled for positions E1 through E4 within the different tissues as pointed out in Figure 3.3.

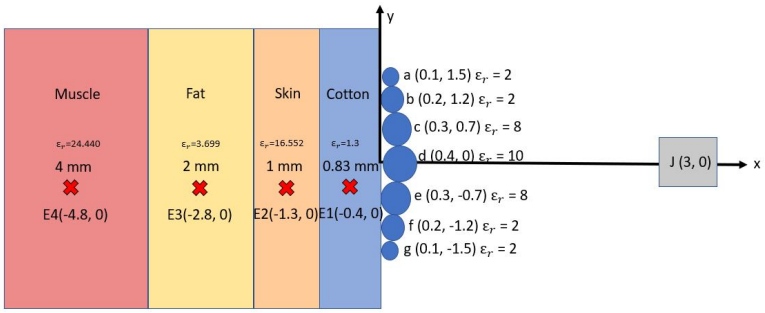

Figure 3.3 The model used for 2D analysis with the multilayer medium, dielectric cylinders, and source. The positions of the sampled fields are identified by each x.

The results for six different cases are computed and tabulated, starting with the source radiating in free space for case 1. Case 2 includes the tissue layers. Case 3 adds the dielectric cylinders. Case 4 includes a source radiating in free space but with a reflector antenna included to focus the field in the negative x direction. Case 5 adds the tissue layers to case four while case 6 adds the cylinders to case 5 and is considered the main configuration of this work. All cases are analyzed for 28 GHz and 29 GHz separately using the respective frequency dependent tissue parameters listed in Table 3.1.

Table 3.1 Dielectric Properties of Application Tissues from 28 GHz to 29 GHz

Frequency [GHz]	Tissue	Permittivity	Conductivity [S/m]
	Cotton	1.3	0
28	Skin Dry	16.552	25.824
29	Skin Dry	16.017	26.478
28	Fat	3.699	1.698
29	Fat	3.668	1.747
28	Muscle	24.44	33.609
29	Muscle	23.783	34.565

The results for the six cases are provided for 28 and 29 GHz. The E-field values are normalized using the maximum incident wave source. For cases 1 through 3, this source is without the reflector placed 3 mm from the model. For cases 4 through 6, this source includes the reflector antenna, which focuses the E-field. The E-field values for the incident wave source for cases 1 and 4 in free space are shown in Table 3.2. The summary of the results from the six cases are shown in Table 3.3 and Table 3.4 for 28 GHz and 29 GHz, respectively. Following the procedure in [27], the E-field gain is calculated using case 1 as well as case 2 results as a baseline against the rest of the cases. Note that the sampled E1 field decreases from case 1 to case 2 but increases in case 3, as expected since case 3 includes the dielectric cylinders. The same trend occurs for cases 4 through 6. Note that the E-field decreases more from cases 4 to 5 and increases more for case 6 than case 3 due to the reflector antenna placed at the source. The gain is approximately 6 dB for case 3 against case 2 for both 28 and 29 GHz. The gain is greater than 8 dB for case 6 with the reflector antenna and dielectric cylinders. Table 3.5 shows the comparison of these results relative to those reported in [27]. Both models have the same dimensions and dielectric properties for the tissue models and use the TM mode for the wave propagation to solve for the E-field. In [27], the 2D cylindrical wave approach is used to analyze six dielectric cylinders placed at the surface of the model with different dimensions and dielectric properties for the cylinders compared to the seven dielectric cylinders presented here. Note that better results are achieved in this model with a gain of 8 dB at E1 position which is a good representation for a wearable antenna position.

This analysis demonstrates that the 6 dB E-field gain previously reported can be increased to 8 dB to achieved better charging of biomedical devices placed just above the skin layer for 5G bands of 28 and 29 GHz. This enhancement of E-field gain is achieved by using the proper selection of the dielectric cylinders' permittivity and the placing of the conductive reflector behind the source.

Table 3.2 Cases 1 through 6 at 28 GHz

Case	E_{inc} at 28 GHz [e$^{-17}V/m$]	E_{inc} at 29 GHz [e$^{-17}V/m$]
C1	1.455	1.481
C4	1.055	1.158

Table 3.3 Cases 1 through 6 at 28 GHz

Case	E1	Gain C/C1 [dB]	Gain C/C2 [dB]
C1	1.000	0	3.451
C2	0.672	-3.451	0
C3	1.346	2.579	6.030
C4	1.000	-2.792	0.659
C5	0.451	-9.701	-6.250
C6	2.500	5.168	8.620

Table 3.4 Cases 1 through 6 at 29 GHz

Case	E1	Gain C/C1 [dB]	Gain C/C2 [dB]
C1	1.000	0	3.342
C2	0.681	-3.342	0
C3	1.317	2.39	5.731
C4	1.000	-2.137	1.205
C5	0.539	-7.506	-4.164
C6	2.212	4.757	8.099

Table 3.5 Results Comparison at 28 and 29 GHz with Results from [27]

Gain C6/C2 at 28 GHz [dB]	Gain C6/C2 at 29 GHz [dB]	Gain $x = 0.4$ mm at 24 GHz [dB] [27]
8.620	8.099	6.431

The first case is case 1 at 28 GHz in free space with the source as identified as J_1 in Figure 3.4. This case is used as a baseline for calculating the focused gain at the sampled E-field points E1 through E4. Figure 3.5 shows the results for the E-field in the x-y plane. As expected, these results do not change for all frequencies. The E-field decreases from E1 to E4 further away from the source.

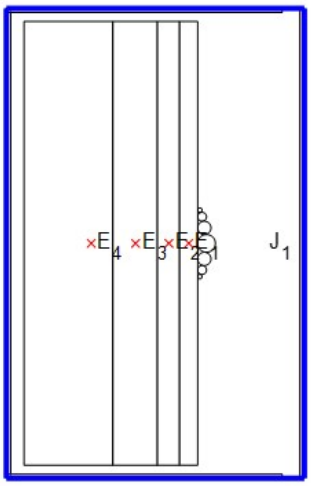

Figure 3.4 Case 1 setup for model.

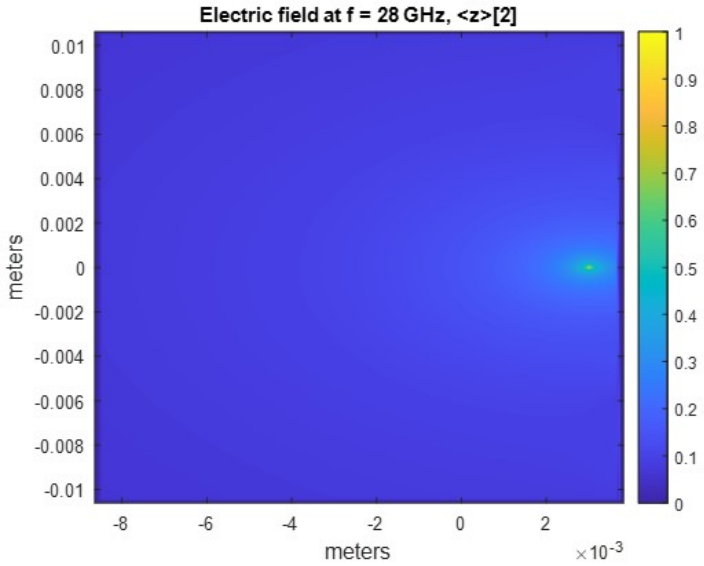

Figure 3.5 E-field 2D results for case 1 at 28 GHz.

The next case is case 1 at 29 GHz in free space. Again, this case is used as a baseline for calculating the focused gain at the sampled E-field points E1 through E4. The results are very similar for case 1 for 28 and 29 GHz. Figure 3.6 shows the E-field results at 29 GHz for the model geometry in the x-y plane.

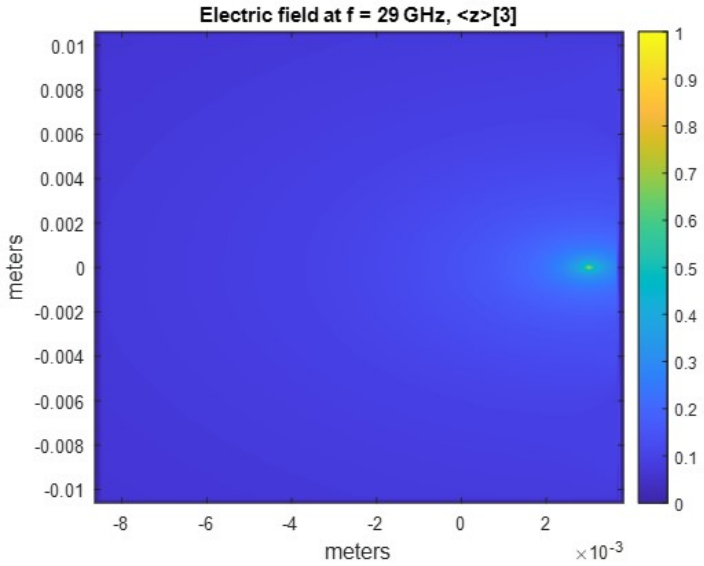

Figure 3.6 E-field 2D results for case 1 at 29 GHz.

The next case is case 2 for 28 GHz with the tissue layers of the medium. The layers are assigned the dielectric properties at this frequency. Figure 3.7 shows the model geometry for case 2. Figure 3.8 shows the E-field results at 28 GHz in the x-y plane. As expected, the sampled E-field is less than case 1 due to the absorption of the scattered E-field within the medium.

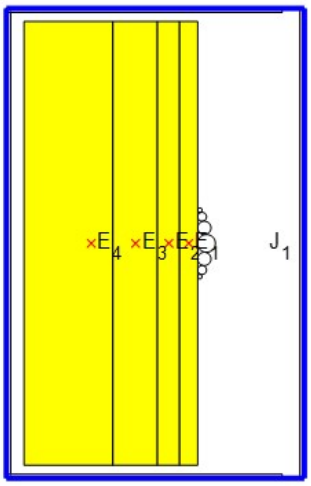

Figure 3.7 Case 2 setup for model.

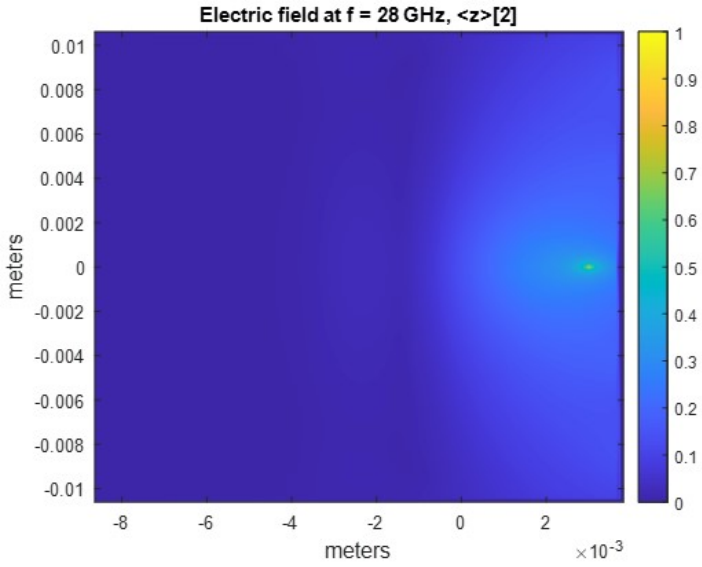

Figure 3.8 E-field 2D results for case 2 at 28 GHz.

The next case is case 2 for 29 GHz with the tissue layers of the medium. The layers are assigned the dielectric properties at this frequency. Figure 3.9 shows the scattered E-field for 29 GHz which is very similar to 28 GHz. As expected, the sampled E-field is less than case 1 due to the absorption of the scattered E-field within the medium.

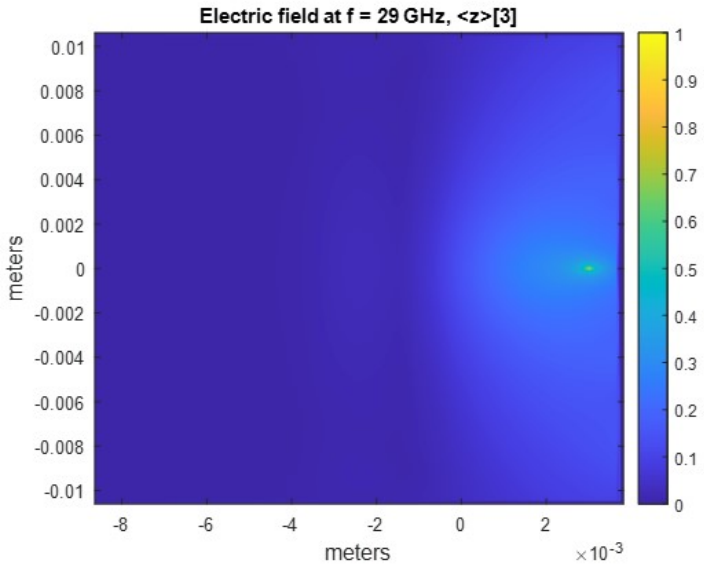

Figure 3.9 E-field 2D results for case 2 at 29 GHz.

The next case is case 3 for 28 GHz with the tissue layers of the medium. Figure 3.10 shows model geometry for case 3. The layers are assigned the dielectric properties at this frequency and the dielectric cylinders are included. Figure 3.11 shows the E-field results for the model setup in the x-y plane. Note that the E-field is focused just above (0, 0) at the surface of the medium. As expected, the sampled E-field is greater than the previous cases due to the presence of the cylinders.

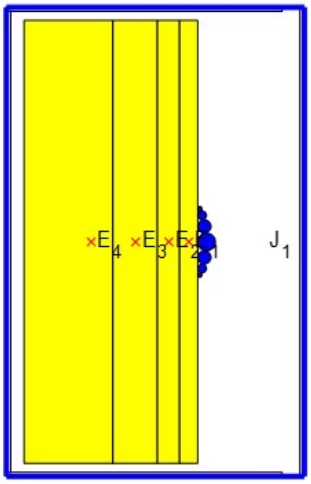

Figure 3.10 Case 3 setup for model.

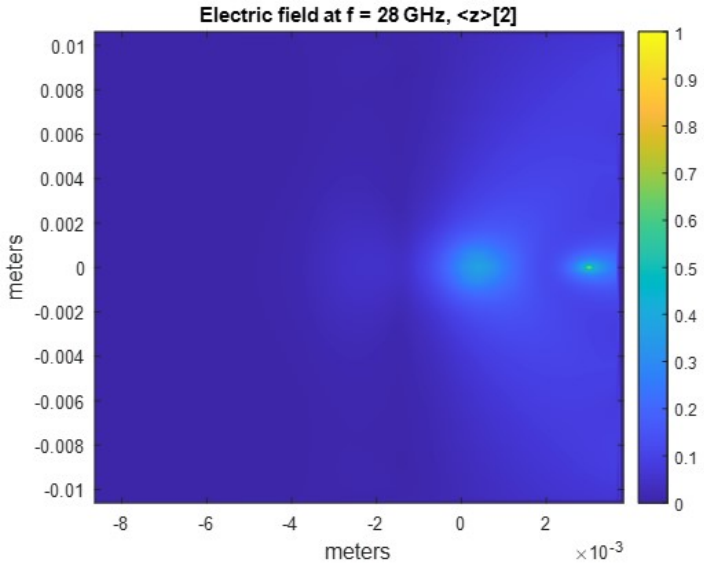

Figure 3.11 E-field 2D results for case 3 at 28 GHz.

The next case is case 3 for 29 GHz with the tissue layers of the medium. The layers are assigned the dielectric properties at this frequency and the dielectric cylinders are included. Figure 3.12 shows the E-field results at 29 GHz for the model in the x-y plane. Again, the E-field is focused just above the surface of the medium. As expected, the sampled E-field is greater than the previous cases due to the presence of the cylinders.

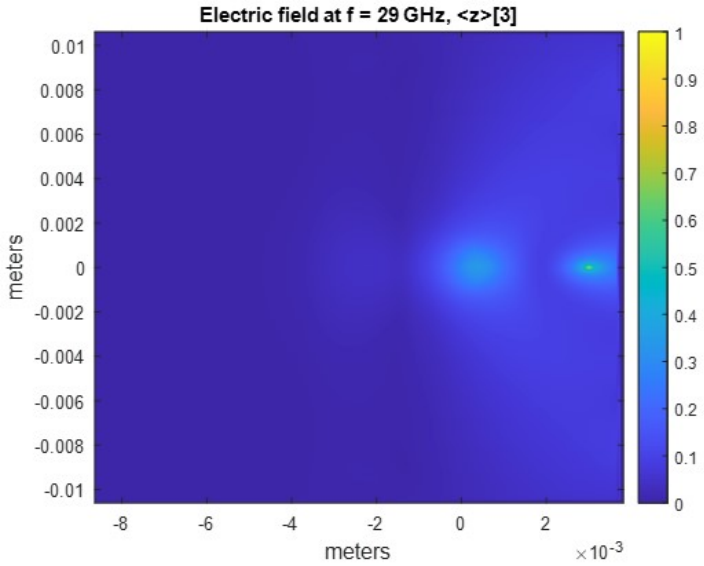

Figure 3.12 E-field 2D results for case 3 at 29 GHz.

The next case is case 4 for 28 GHz with free space and the reflector antenna. Figure 3.13 shows model geometry for case 4. Figure 3.14 shows the E-field results for the model setup in the x-y plane. The E-field is less than case 1 due to the presence of the reflector.

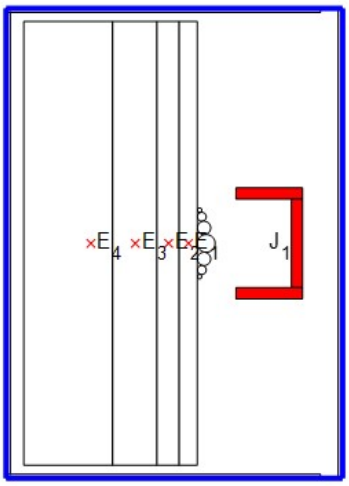

Figure 3.13 Case 4 setup for model.

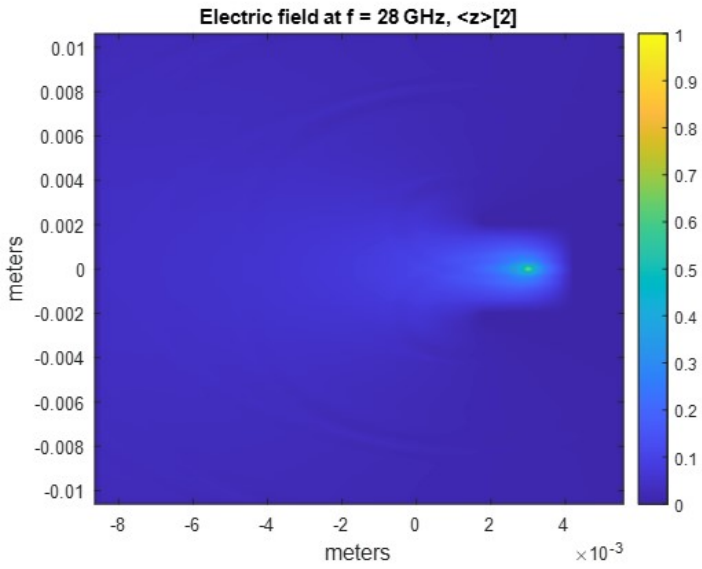

Figure 3.14 E-field 2D results for case 4 at 28 GHz.

The next case is case 4 for 29 GHz with free space and the reflector antenna. Figure 3.15 shows model geometry for case 4 in the x-y plane. Again, the E-field is focused at (0, 0) at the surface of the medium.

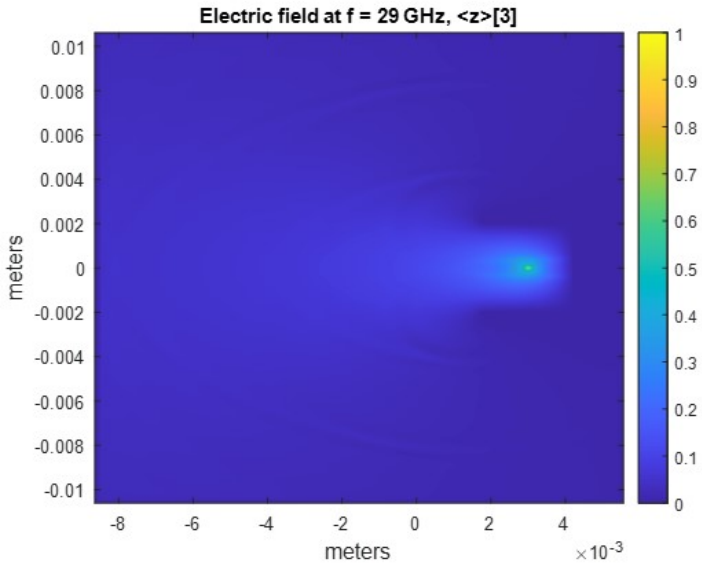

Figure 3.15 E-field 2D results for case 4 at 29 GHz.

The next case is case 5 for 28 GHz with the layers of the medium included and the reflector antenna. Figure 3.16 shows model geometry for case 5. Figure 3.17 shows the E-field results for the model setup in the x-y plane. The E-field is less than case 4 due to the dielectric tissue layers of the medium.

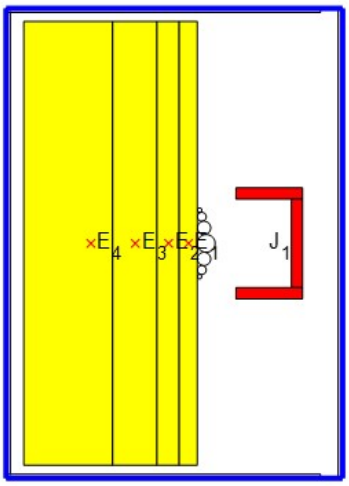

Figure 3.16 Case 5 setup for model.

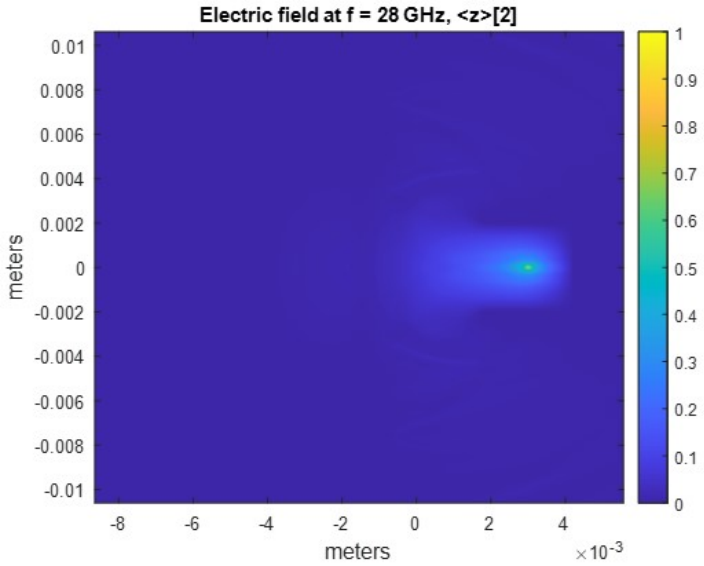

Figure 3.17 E-field 2D results for case 5 at 28 GHz.

The next case is case 5 for 29 GHz with the layers of the medium included and the reflector antenna. Figure 3.18 shows the E-field results for the model in the x-y plane.

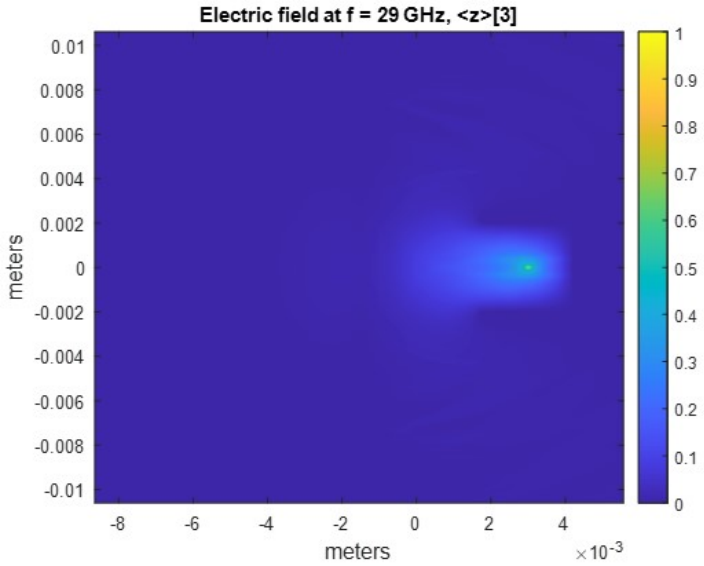

Figure 3.18 E-field 2D results for case 5 at 29 GHz.

The next case is case 6 for 28 GHz with the dielectric cylinders, layers of the medium, and the reflector antenna. Figure 3.19 shows model geometry for case 6. Figure 3.20 shows the E-field results for the model setup in the x-y plane. Note that the E-field is concentrated above the tissue layers at approximately (0,0). The E-field is greater than case 4 and case 5 due to the presence of the dielectric cylinders.

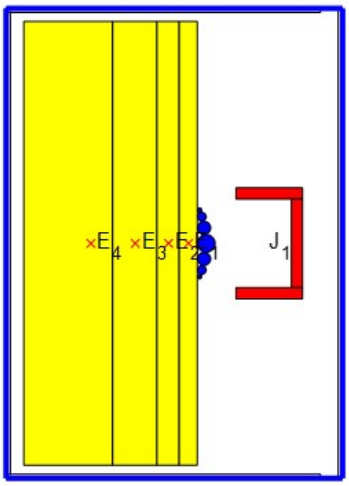

Figure 3.19 Case 6 setup for model.

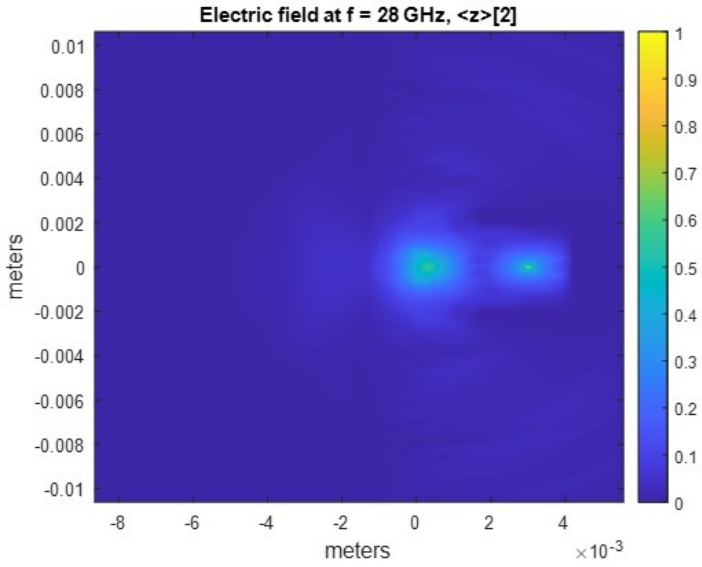

Figure 3.20 E-field 2D results for case 6 at 28 GHz.

The last case is case 6 for 29 GHz with the dielectric cylinders, layers of the medium, and the reflector antenna. Figure 3.21 shows the E-field results for the model setup in the x-y plane. Again, the E-field is concentrated above the tissue layers at approximately (0,0).

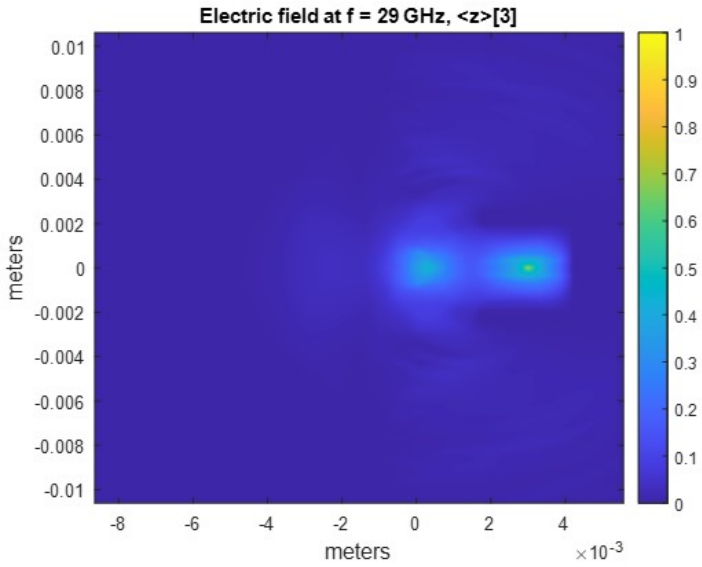

Figure 3.21 E-field 2D results for case 6 at 29 GHz.

CHAPTER 4

3D FDTD BIOMEDICAL APPLICATIONS

4.1 FDTD Simulations with Dispersive Media

Human tissues are one of the well-known categories of materials that are characterized as dispersive media. Their electromagnetic properties change depending on the frequency of the source.

Dispersive media can be evaluated using a variety of models, including the Lorentz model, Drude model, Cole-Cole model, and Debye model. The Debye model is commonly used for biological tissue simulations to improve computational efficiency for a wide range of frequencies.

For the dispersive FDTD formulation, the electric flux density changes depending on the permittivity as shown in equation 3.5. The E-fields change based on the permittivities of the human tissues. Thus, the FDTD algorithm is adapted to include updating equations for the D-fields so the Debye model can be applied to develop the E-fields using an auxilary differential equation (ADE) procedure for the updating equation of the E-field as shown in 4.1 and polarization current J as shown in 4.2 as described for the algorithm in chapter 13 in [1].

$$\bar{J}_k^{n+1} = \frac{(2\tau_k - \Delta t)}{(2\tau_k + \Delta t)}\bar{J}_k^n + \frac{2\zeta_k}{(2\tau_k + \Delta t)}(\bar{E}^{n+1} - \bar{E}^n) \tag{4.1}$$

$$\bar{E}^{n+1} = \frac{2\Delta t}{2\epsilon_0\epsilon_\infty + \sigma\Delta t + \xi}\nabla \times \bar{H}^{n+0.5} + \frac{2\epsilon_0\epsilon_\infty - \sigma\Delta t + \xi}{2\epsilon_0\epsilon_\infty + \sigma\Delta t + \xi}\bar{E}^n - \frac{2\Delta t}{2\epsilon_0\epsilon_\infty + \sigma\Delta t + \xi}\sum_{k=1}^{p}\frac{2\tau_k}{2\tau_k + \Delta t}\bar{J}_k^n \tag{4.2}$$

4.2 Wireless Charging Application - 3D Model

The next application to consider is the more realistic 3D dispersive analysis of the tissue model setup as an extension to the 2D wireless charging application. The 2D model uses the traditional FDTD algorithm along the x and y planes. The 3D model, however, uses the dispersive FDTD algorithm with the Debye parameters listed in chapter 2 for human tissues. The Debye parameters are used for the frequency range of 20 to 100 GHz to account for the target frequencies of 28 and 29 GHz. Each simulation is run to capture the E-fields for 28 and 29 GHz at the same time rather than separately as for the 2D application. The plane wave source is set up for the same incident direction as in the 2D simulation cases.

The analysis is performed using CEMS as in [1] rather than the developed 2D MATLAB code to allow for realistic 3D modeling of the application. The material parameters are set for each tissue layer of dispersive model using the ϵ_∞, $\Delta\epsilon_1$, $\Delta\epsilon_2$, $\Delta\epsilon_3$, τ_1, τ_2, τ_3 terms which can be set from 20 to 100 GHz.

The wrist model is imported into CEMS from the 3D voxel model described in [35] and described in chapter 2. The model consists of six tissue layers of skin, fat, muscle, blood, bone cortical, and bone marrow as shown in Figure 4.1. The x, y, and z dimensions are based on a scan of an actual human wrist. The general dimensions are $x = 70$ mm, $y = 84$ mm, and $z = 80$ mm. The data is collected by scanning an average human body and the cell resolution for the cubic voxels is originally 2 mm per cell [32]. The resolution used for this model is determined based on the dimensions of the dielectric cylinders. The dielectric cylinders have a length of 15 mm along the z direction and width of 10 mm. The general setup is shown in Figure 4.2. The dielectric cylinders are assigned the same relative permittivities as for the 2D model that range from 2 to 10 with the most dielectric constant cylinder at the center. The dimensions of each cylinder radius are adapted based on the procedure developed in the 2D model. The cylinders are placed 1 mm away from the surface of the wrist to account for a layer of fabric such as cotton that is not present in this simulation. The cylinders are identified by the letters "a" to "g" with the center cylinder identified as cylinder "d". The radius of cylinder "d" is 0.9 mm. The radius of cylinders "c" and "e" is 0.8 mm. The radius of cylinders "b" and "f" is 0.7 mm. The radius of cylinders "a" and "g" is 0.6 mm. As with the 2D model, the tapered radius of cylinders helps focus the field along the negative x direction. The cell resolution for this analysis is set to $x = 0.1$ mm, $y = 0.1$ mm, and $z = 0.25$ mm. This resolution satisfies the necessary cells per wavelength based on the largest relative permittivity of the tissues, muscle, at the frequencies of interest. For an approximate frequency of 30 GHz and relative permittivity of 25, this is 2 mm for the wavelength. Thus, this resolution allows for approximately 20 cells per wavelength in the x and y planes and 8 cells per wavelength in the z plane. The smallest dielectric cylinder has a radius of 0.6 mm which allows for 12 cells across the diameter of the cylinder in the x and y planes. At this resolution, all seven cylinders are included in the material mesh for the simulations. The total problem space size is 217,535,736 cells, which requires approximately 9 hours of CPU run time per simulation.

The simulations consist of seven different positions of the cylinders around the wrist model. The cylinders are adapted to the same general position along z but different positions in x and y around the wrist as shown in Figure 4.3. Each position is shown in Figure 4.4 through Figure 4.10. This setup accounts for the effects of the tissues and bones on the E-field and thus the achieved gain. For each position, the same cases 1, 2, and 3 are executed for the 2D model. The output sampled E-fields for E1 through E4 are set at the same approximate locations as for the 2D model. However, this thesis will focus here on presenting results for the field values at E1 from case 1, 2, and 3. At these dimensions and cell resolution, the model is set to run for 7,000 time steps to ensure convergence in the time domain as shown in Figure 4.11.

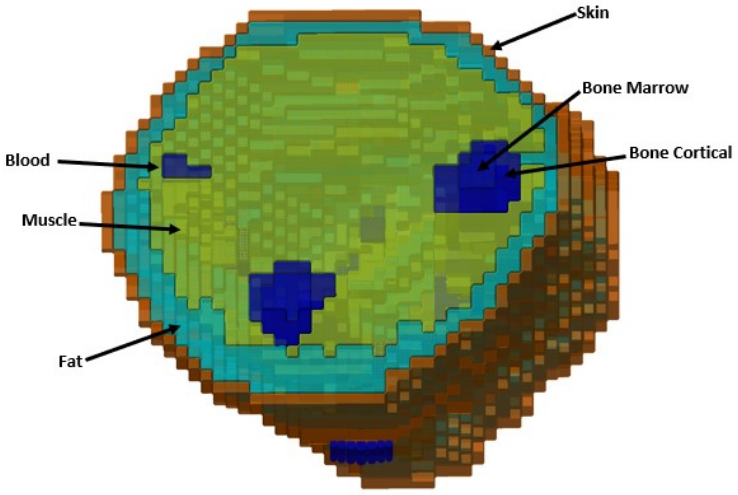

Figure 4.1 The tissue layers in the cross section of the 3D wrist model.

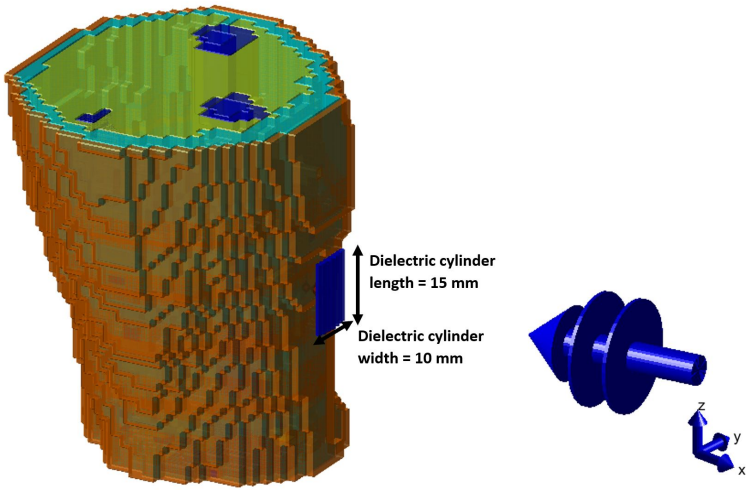

Figure 4.2 The setup for the wrist model, cylinders, and plane wave excitation.

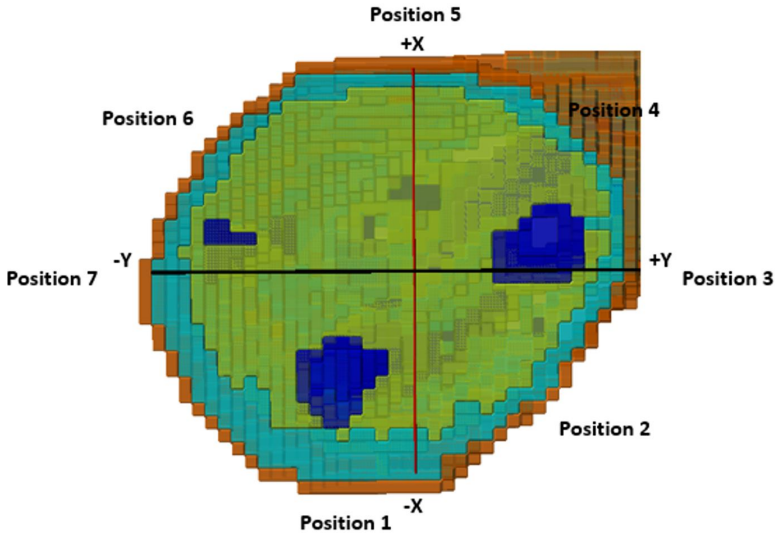

Figure 4.3 The seven positions of the dielectric cylinders for the simulations.

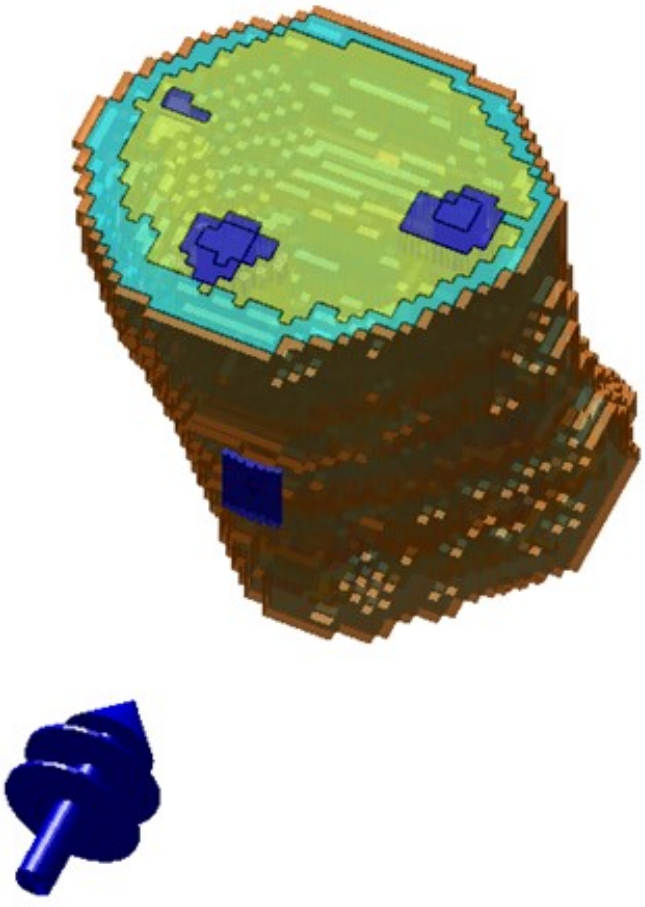

Figure 4.4 Position 1 setup for tissues, cylinders, and the plane wave excitation model.

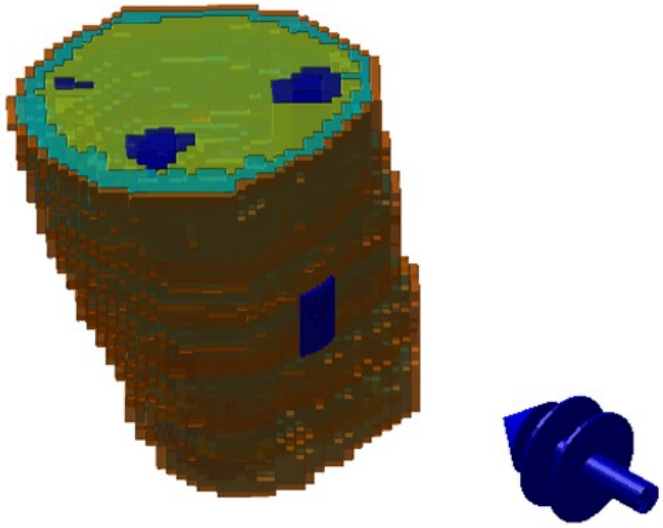

Figure 4.5 Position 2 setup for tissues, cylinders, and the plane wave excitation model.

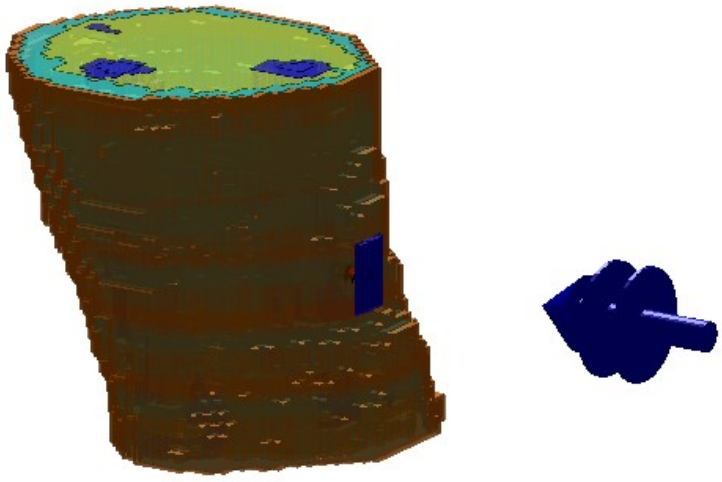

Figure 4.6 Position 3 setup for tissues, cylinders, and the plane wave excitation model.

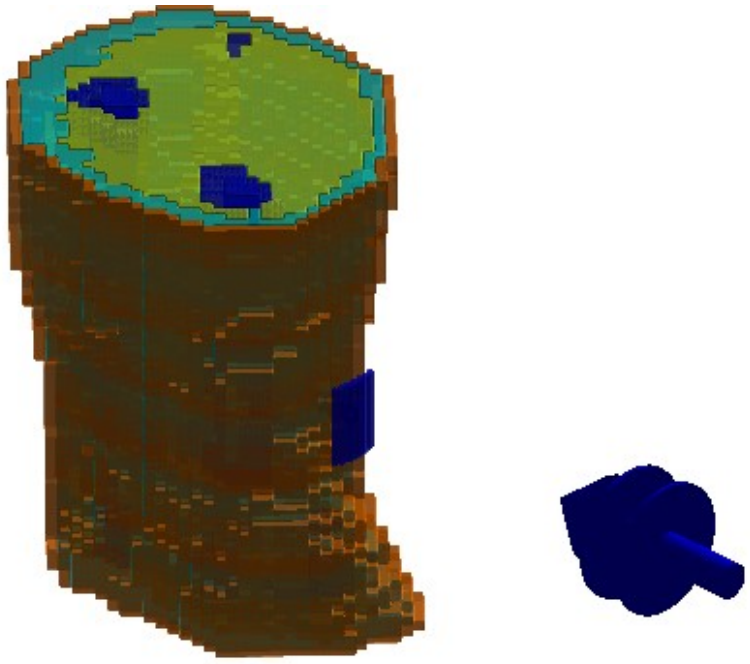

Figure 4.7 Position 4 setup for tissues, cylinders, and the plane wave excitation model.

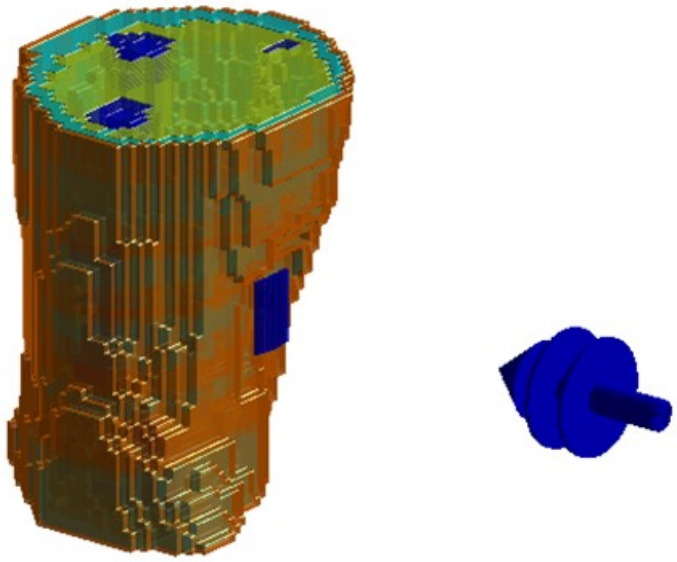

Figure 4.8 Position 5 setup for tissues, cylinders, and the plane wave excitation model.

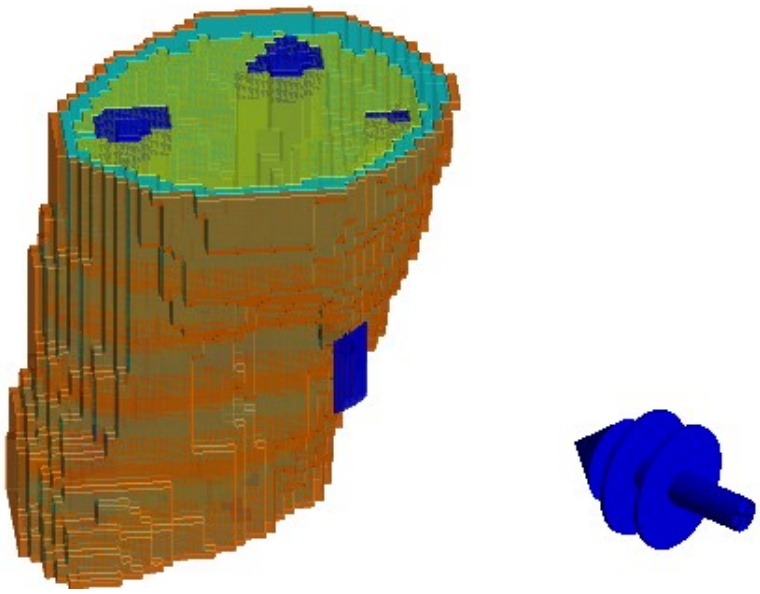

Figure 4.9 Position 6 setup for tissues, cylinders, and the plane wave excitation model.

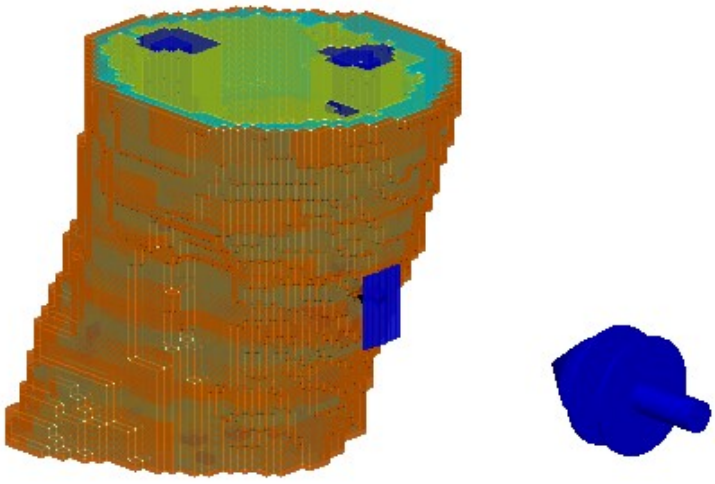

Figure 4.10 Position 7 setup for tissues, cylinders, and the plane wave excitation model.

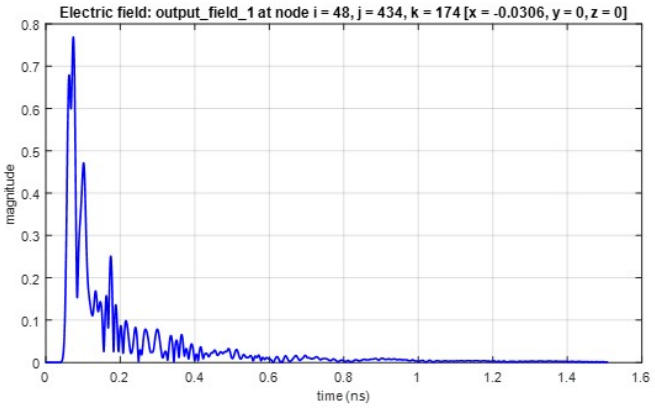

Figure 4.11 Position 1 case 3 time domain data for 7,000 time steps.

The results for cases 1 through 3 with the plane wave excitation are provided for all seven positions. Table 4.1 and Table 4.2 show the summary of the gains at 28 and 29 GHz for the seven positions. The results of cases 1 through 3 for each position are shown in Table 4.3 through Table 4.16 for 28 GHz and 29 GHz, respectively. The E-field values are normalized using the E-field values of the maximum incident plane wave at 28 and 29 GHz shown in Figure 4.12. The E-field for the incident plane wave is calculated in the time domain and transformed to the frequency domain just like the output E-field values for the model. Following the procedure in [27], the E-field gain is calculated using case 2 as a baseline against the rest of the cases. The maximum gain values are for case 3 for both 28 and 29 GHz as expected. The positions with the largest gains are position 1, 3, and 4, and these cases also have the largest attenuation due to the dielectric tissues. Position 1 has the largest gain for case 3 against case 2 of approximately 10 dB for both 28 GHz and 29 GHz. Position 1 also has the largest attenuation of case 2 against case 1 of approximately -10 dB as expected.

Table 4.1 Gain for Positions 1 through 7 at 28 GHz

Position	Gain C2/C1 [dB]	Gain C3/C2 [dB]
1	-10.308	9.426
2	-5.041	2.472
3	-6.220	5.921
4	-6.301	6.287
5	-4.743	1.543
6	-2.905	5.513
7	-2.066	4.416

Table 4.2 Gain for Positions 1 through 7 at 29 GHz

Position	Gain C2/C1 [dB]	Gain C3/C2 [dB]
1	-10.014	9.848
2	-5.354	2.688
3	-7.882	7.920
4	-5.468	3.992
5	-4.413	2.192
6	-3.140	2.924
7	-1.728	3.915

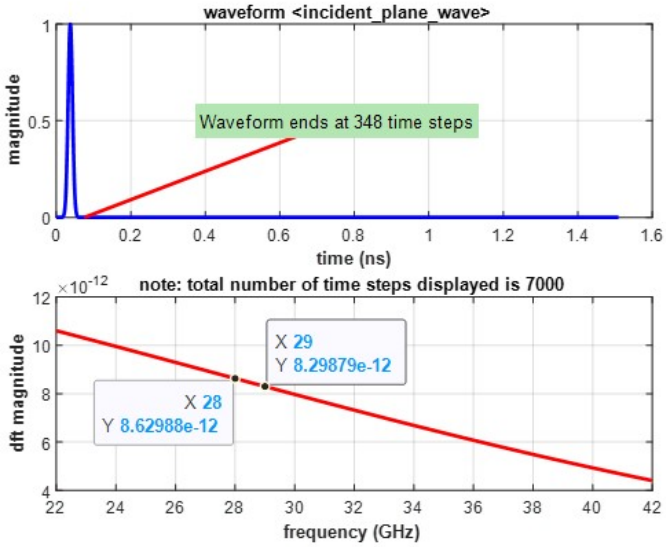

Figure 4.12 The incident plane wave source for 7,000 time steps at 28 and 29 GHz.

Table 4.3 Position 1 Cases 1 through 3 at 28 GHz

Case	E1	Gain C/C1 [dB]	Gain C/C2 [dB]
C1	1.000	0	10.308
C2	0.305	-10.308	0
C3	0.903	-0.882	9.426

Table 4.4 Position 1 Cases 1 through 3 at 29 GHz

Case	E1	Gain C/C1 [dB]	Gain C/C2 [dB]
C1	1.000	0	10.014
C2	0.316	-10.014	0
C3	0.981	-0.167	9.848

Table 4.5 Position 2 Cases 1 through 3 at 28 GHz

Case	E1	Gain C/C1 [dB]	Gain C/C2 [dB]
C1	1.000	0	5.041
C2	0.560	-5.041	0
C3	0.744	-2.570	2.472

Table 4.6 Position 2 Cases 1 through 3 at 29 GHz

Case	E1	Gain C/C1 [dB]	Gain C/C2 [dB]
C1	1.000	0	5.354
C2	0.540	-5.354	0
C3	0.736	-2.666	2.688

Table 4.7 Position 3 Cases 1 through 3 at 28 GHz

Case	E1	Gain C/C1 [dB]	Gain C/C2 [dB]
C1	1.000	0	6.220
C2	0.489	-6.220	0
C3	0.966	-0.300	5.921

Table 4.8 Position 3 Cases 1 through 3 at 29 GHz

Case	E1	Gain C/C1 [dB]	Gain C/C2 [dB]
C1	1.000	0	7.882
C2	0.404	-7.882	0
C3	1.004	0.038	7.920

Table 4.9 Position 4 Cases 1 through 3 at 28 GHz

Case	E1	Gain C/C1 [dB]	Gain C/C2 [dB]
C1	1.000	0	6.301
C2	0.484	-6.301	0
C3	0.998	-0.014	6.287

Table 4.10 Position 4 Cases 1 through 3 at 29 GHz

Case	E1	Gain C/C1 [dB]	Gain C/C2 [dB]
C1	1.000	0	5.468
C2	0.533	-5.468	0
C3	0.844	-1.476	3.992

Table 4.11 Position 5 Cases 1 through 3 at 28 GHz

Case	E1	Gain C/C1 [dB]	Gain C/C2 [dB]
C1	1.000	0	4.743
C2	0.579	-4.743	0
C3	0.692	-3.199	1.543

Table 4.12 Position 5 Cases 1 through 3 at 29 GHz

Case	E1	Gain C/C1 [dB]	Gain C/C2 [dB]
C1	1.000	0	4.413
C2	0.602	-4.413	0
C3	0.774	-2.222	2.192

Table 4.13 Position 6 Cases 1 through 3 at 28 GHz

Case	E1	Gain C/C1 [dB]	Gain C/C2 [dB]
C1	1.000	0	2.905
C2	0.716	-2.905	0
C3	1.350	2.609	5.513

Table 4.14 Position 6 Cases 1 through 3 at 29 GHz

Case	E1	Gain C/C1 [dB]	Gain C/C2 [dB]
C1	1.000	0	3.140
C2	0.697	-3.140	0
C3	0.975	-0.216	2.924

Table 4.15 Position 7 Cases 1 through 3 at 28 GHz

Case	E1	Gain C/C1 [dB]	Gain C/C2 [dB]
C1	1.000	0	2.066
C2	0.788	-2.066	0
C3	1.311	2.350	4.416

Table 4.16 Position 7 Cases 1 through 3 at 29 GHz

Case	E1	Gain C/C1 [dB]	Gain C/C2 [dB]
C1	1.000	0	1.728
C2	0.820	-1.728	0
C3	1.286	2.188	3.915

In comparison at 28 GHz, the gain is approximately 10 dB for case 3 against case 2, improved from 6 dB for the 2D application. This change in the results is affected by the more accurate representation of the wrist tissue model using the dispersive FDTD approach. The 3D model accounts for more tissues, including bone cortical and bone marrow, which affects the reflection of the E-field through the tissue. Note that the largest gains are achieved for positions 1, 3, and 4. These positions are the closest to the bone tissues as shown for position 1 in Figure 4.13. The E-field is reflected due to the bone tissues, increasing the gain. The smallest gains occur at positions 2 and 5 further from the bone tissues as shown for position 2 in Figure 4.14. As the E-field penetrates through the lossy tissue model, less gain is achieved for these positions.

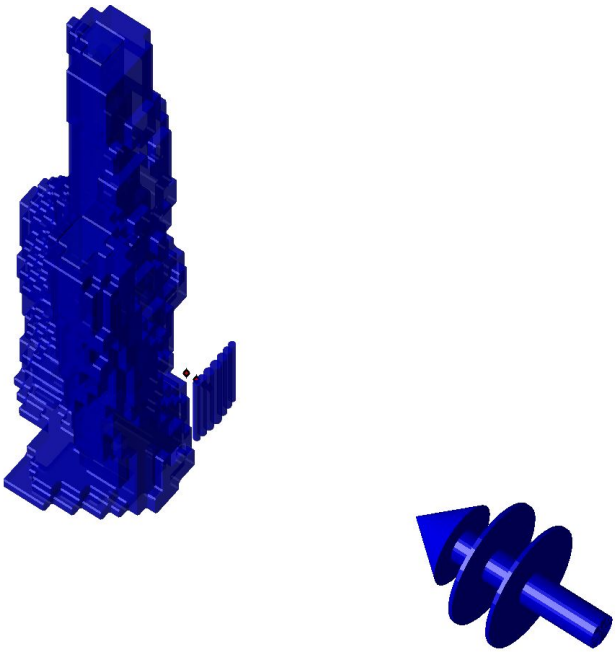

Figure 4.13 Position 1 setup with just the bone tissues shown.

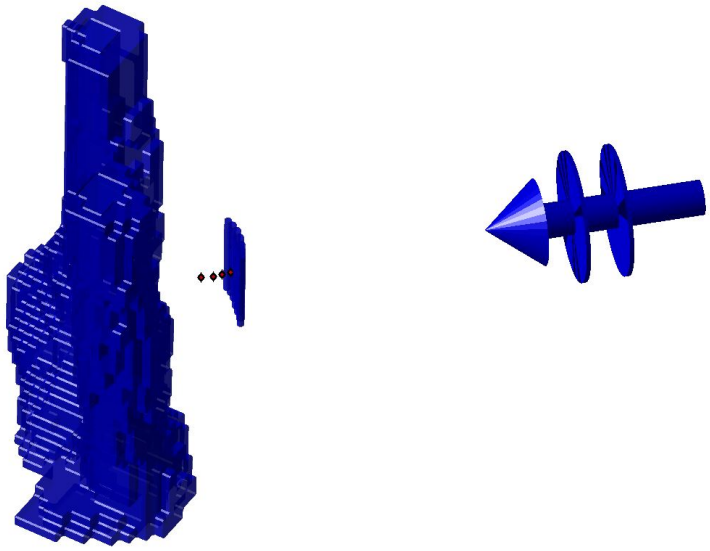

Figure 4.14 Position 2 setup with just the bone tissues shown.

The 3D application consists of simulations of the wrist model for seven different positions to determine the output E-fields E1 through E4. The largest gain achieved is 10 dB for both 28 and 29 GHz for case 3 against case 2 for position 1. The results demonstrate effective maximum gain can be achieved using an accurate dispersive FDTD simulation with tissues and bones imported from a realistic wrist model.

CHAPTER 5
CONCLUSIONS AND FUTURE WORK

This thesis has accomplished many aspects of accurate implementation of human tissues for wearable 5G biomedical wireless applications. However, there are still areas where future work is required.

5.1 Accomplishments

This thesis demonstrates practical implementation of the FDTD algorithm to biomedical wireless charging applications at 5G frequencies. As the biomedical wireless device industry grows, so will the need for efficient power transfer to these devices. Some of the challenges with higher frequency devices include higher path loss, increased sensitivity to manufacturing defects and tolerances, and health concerns regarding specific absorption rate (SAR) with no standard in place at frequencies above 24 GHz. This technology not only requires efficient design of wireless technologies, but also a thorough understanding of the effects on human tissues.

The human tissues described in this thesis are characterized according to their dielectric properties. The relative permittivity and conductivity for each tissue are collected based on measured data in [36] for frequencies from 100 MHz to 100 GHz. This data is very useful as biomedical applications are moving into higher frequencies in the 5G bands. The dielectric properties are then used to calculate the Debye coefficients using the methodology described in [33]. The Debye parameters are required for each tissue to run the FDTD algorithm for dispersive mediums and more accurate modeling.

The human tissues are then discretized into the computational domain. This step determines proper setup of the 3D human tissue model and image processing. The images are processed for both the horizontal cross section in the x-y plane as well as the vertical cross section in the x-z plane Figure 2.3. The 3D voxel model of the human wrist is imported from [32] into CEMS. The Debye parameters of the tissues are entered into the model. The cell resolution, time steps, and other factors are adjusted to allow for accurate results.

The 2D and 3D models in this thesis successfully analyze the E-field results of a plane wave source due to human tissues of the wrist and their dielectric properties. The models replicate the effects of a wireless sensor attached to a user's wrist. Both models utilize dielectric cylinders placed above the wrist that provide intensification of the E-field for power transmission. Dielectric cylinders are chosen because they can easily be integrated into the fabric of a user's clothing. The 2D model uses cylinders with a width of x = 3.2 mm and length of y = 20 mm. The 3D model uses cylinders with a width of 10 mm and length of z = 15 mm. Thus, both models are compact in size yet still have great potential for fabrication. The gain

achieved for the 2D model is 8 dB, 2 dB higher than the gain achieved in the comparable model described in [27]. The 3D model shows a gain of up to 10 dB depending on the position of the cylinders above the wrist.

The 3D model accounts for the effects of tissue as well as bone within a realistic human wrist. Thus, the high maximum gain is due to the effects of bone on the reflection of the E-field. Most of the research with wearable antennas or other similar applications in this area utilize simplified human tissue models with cross sections of human tissue rather than more realistic 3D models using the approach in this thesis. This thesis demonstrates an application where an accurate 3D model is used to allow for more thorough understanding of the potential gain that can be achieved for charging a wireless biomedical device.

5.2 Future Work

While many aspects of the FDTD algorithm and human tissue model were explored for this application, future work is needed.

The models explored only account for wearable technologies and do not include the potential of embedded devices. Many biomedical applications are moving towards embedded bio-compatible devices. An understanding of the potential power transfer of embedded devices could apply to improvement of common devices such as pacemakers. However, embedded technologies are more complex as far as size limitations, path loss, safety, and other factors.

The models also require further optimization. The 2D model reflector antenna design could be improved by using a corner reflector for a more focused beam and hence higher gain. The 3D model could include a fabric substrate layer and more experimentation with the output E-field point placements within the wrist tissue. Placing the output E-field points deeper into the tissue would provide more detail on the reflection and transmission of the E-field through the wrist. Such a model would require a very large number of time steps to eliminate the error of the output E-fields.

The extension of this study is to calculate the SAR and temperature rise in the human tissues to understand the safety limitations of the 5G wireless device similar to the work in [38]. The maximum SAR_{1g}, SAR_{10g}, and temperature rise values in the head are obtained for the antenna placed in two different positions in a pair of smart glasses. The model also uses the dispersive FDTD algorithm to compute the results. The SAR_{1g}, SAR_{10g}, and temperature rise values would determine the best position of the dielectric cylinders and the input power that could be used to stay within the RF exposure guidelines and standards [38].

REFERENCES

[1] A. Z. Elsherbeni and V. Demir. *The Finite-Difference Time-Domain Method for Electromagnetics with MATLAB Simulations*. SciTech Publishing, an Imprint of IET, Edison, NJ, 2015.

[2] M.F. Lateef A.S.M. Alqadami M. Ikram, K. Sultan. A Road towards 6G Communication: A Review of 5G Antennas, Arrays, and Wearable Devices. *Electronics*, 11(1):169, 2022.

[3] M. Tahir A. Ahad and K. A. Yau. 5G-Based Smart Healthcare Network: Architecture, Taxonomy, Challenges and Future Research Directions. *IEEE Access*, 7:100747–100762, 2019.

[4] L. Matekovits L. Kouhalvandi and I. Peter. Magic of 5G Technology and Optimization Methods Applied to Biomedical Devices: A Survey. *Applied Sciences*, 12(14):7096, 2022.

[5] K. Johnsson A. Turlikov S. Andreev O. Galinina, A. Pyattaev and Y. Koucheryavy. Assessing System-Level Energy Efficiency of mmWave-Based Wearable Networks. *IEEE Journal on Selected Areas in Communications*, 34(4):923–937, 2016.

[6] M. A. Rojavin and M. C. Ziskin. Medical application of millimetre waves. *QJM: An International Journal of Medicine*, 91(1):57–66, 1998.

[7] A. S. Weddell S. Beeby M. Wagih, G. S. Hilton. Millimeter-Wave Power Transmission for Compact and Large-Area Wearable IoT Devices Based on a Higher Order Mode Wearable Antenna. *Internet of Things Journal*, 9(7), 2022.

[8] T. Islam P. Kunkolienker S. Roy M. M. Rahman S. Ghos S. Dey D. Mitra T. Nusrat, F. S. Dawod and B. D. Braaten. A Comprehensive Study on Next-Generation Electromagnetics Devices and Techniques for Internet of Everything (IoE. *Electronics*, 11(20):3341, 2022.

[9] J. L. Leiva O. Masso J. Tonnesen E. Rindalsholt R. Brandsegg R. Gaddi J. Anguera, A. Andujar. Reconfigurable Multiband Operation for Wireless Devices Embedding Antenna Boosters. *Electronics*, 10(7):808, 2021.

[10] J. H. Park L. Lin T. Tang J. Li, Y. Dong and J. Yoo. Body-Area Powering With Human Body-Coupled Power Transmission and Energy Harvesting ICs. *IEEE Transactions on Biomedical Circuits and Systems*, 14(6):1263–1273, 2020.

[11] J. Y. Khan K. M. S. Thotahewa and M. R. Yuce. Power Efficient Ultra Wide Band Based Wireless Body Area Networks with Narrowband Feedback Path. *IEEE Transactions on Mobile Computing*, 13 (8):1829–1842, 2014.

[12] M. Benini E. Chiaramello S. Fiocchi G. Tognola S. Gallucci, M. Bonato and M. Parazzini. Assessment of EMF Human Exposure Levels Due to Wearable Antennas at 5G Frequency Band. *Sensors*, 23(1): 104, 2023.

[13] Y. Rahmat-Samii and L. Song. Advances in Communication and Biomedical Antenna Developments at the UCLA Antenna Lab: Handheld, Wearable, Ingestible, and Implantable [Bioelectromagnetics]. *IEEE Antennas and Propagation Magazine*, 63(5):102–115, 2021.

[14] S. S. Balpande N. Jattalwar and J. A. Shrawankar. Assessment of Denim and Photo Paper Substrate-Based Microstrip Antennas for Wearable Biomedical Sensing. *Wireless Personal Communications*, 115(3):1993–2003, 2020.

[15] A. Sabban. New Compact Wearable Metamaterials Circular Patch Antennas for IoT, Medical and 5G Applications. *Applied System Innovation*, 3(4):42, 2020.

[16] L. Tognolatti C. Ponti and G. Schettini. Electromagnetic Scattering by Metallic Targets Above a Biological Medium With a Spectral-Domain Approach. *IEEE Open Journal of Antennas and Propagation*, 2:230–237, 2021.

[17] B. Schweber. Flexible Skin Patch Merges VCSELs, Ultrasound for Deep-Tissue Blood Sensing, 2023. URL https://www.electronicdesign.com/technologies/test-measurement/article/21259598/electronic-design-flexible-skin-patch-merges-vcsels-ultrasound-for-deeptissue-blood-sensing?utm_source=EG+ED+Today&utm_medium=email&utm_campaign=CPS230208025&o_eid=7596C6158345A7R&rdx.ident[pull]=omeda|7596C6158345A7R&oly_enc_id=7596C6158345A7R.

[18] M. Dragoman A. Dinescu M. Bozzi S. Iordanescu M. Yasir, M. Aldrigo and D. Vasilache. Integration of Antenna Array and Self-Switching Graphene Diode for Detection at 28 GHz. *IEEE Electron Device Letters*, 40(4):628–631, 2019.

[19] S. Ullah D. Choi A. Wajid, A. Ahmad and F. U. Islam. Performance Analysis of Wearable Dual Band Patch Antenna Based on EBG and SRR Surfaces. *Sensors*, 22(14):5208, 2022.

[20] M. D. Geyikoglu. A novel UWB flexible antenna with dual notch bands for wearable biomedical devices. *Analog Integrated Circuits and Signal Processing*, pages 1–12, 2023.

[21] A. J. Alazemi M. I. Waly R. Ghayoula A. Smida, A. Iqbal and S. Kim. Wideband Wearable Antenna for Biomedical Telemetry Applications. *IEEE Access*, 8:15687–15694, 2020.

[22] J. Dong R. Wu and M. Wang. Wearable Polarization Conversion Metasurface MIMO Antenna for Biomedical Applications in 5GHz WBAN. *Bioensors*, 13(1):73, 2023.

[23] M. Kanagasabai T. R. Rao M. G. N. Alsath S. Kumar S. Velan M. Marey T. Govindan, S. K. Palaniswamy and A. Aggarwal. On the design and performance analysis of wristband MIMO/diversity antenna for smart wearable communication applications. *Scientific Reports*, 11(1): 21917, 2021.

[24] C. J. Davenport J. M. Rigelsford, B. F. Al-Azzawi and P. Novodvorsky. A Passive Biodegradable Implant for Subcutaneous Soft-Tissue Trauma Monitoring. *IEEE Journal of Biomedical and Health Informatics*, 19(3):901–909, 2015.

[25] K. H. Park M. J. Jeong J. J. Baek, S. W. Kim and Y. T. Kim. Design and Performance Evaluation of 13.56-mhz Passive RFID for E-Skin Sensor Application. *IEEE Microwave and Wireless Components Letters*, 28(12):1074–1076, 2018.

[26] F. Frezza R. Borghi, M. Santarsiero and G. Schettini. Plane-wave scattering by a dielectric circular cylinder parallel to a general reflecting flat surface. *Journal of the Optical Society of America. A, Optics, image science, and vision*, 14(7):1500, 1997.

[27] L. Tognolatti C. Ponti and G. Schettini. Use of a Set of Wearable Dielectric Scatterers to Improve Electromagnetic Transmission for a Body Power Transfer System. *IEEE Journal of Electromagnetics, RF, and Microwaves in Medicine and Biology*, 6(2):280–286, 2022.

[28] M. Mrozowski and M. A. Stuchly. Parameterization of Media Dispersive Properties for FDTD. *IEEE Transactions on Antennas and Propagation*, 45(9):1438–1439, 1997.

[29] D. Hernandez and K. Kim. Correlation analysis between the complex electrical permittivity and relaxation time of tissue mimicking phantoms in 7 t mri. *Scientific Reports*, 12(1):15444, 2022.

[30] O. Franek S. S. Zhekov and G. F. Pedersen. Dielectric Properties of Human Hand Tissue for Handheld Devices Testing. *IEEE Access*, 7:61949–61959, 2019.

[31] O. Franek S. S. Zhekov and G. F. Pedersen. An Approach to Improve the Misalignment and Wireless Power Transfer into Biomedical Implants Using Meandered Wearable Loop Antenna. *Wireless Power Transfer*, 2021, 2021.

[32] K. Sakurai E. Kunieda S. Watanabe M. Taki T. Nagaoka, S. Watanabe and Y. Yamanaka. Development of realistic high-resolution whole-body voxel models of japanese adult males and females of average height and weight, and application of models to radio-frequency electromagnetic-field dosimetry. *Phys. Med. Biol*, 49(1):1–15, 2004.

[33] R. Lumnitzer A. Tanner A. Z. Elsherbeni. Debye Coefficients for Biological Tissues From 100 MHz to 100 GHz. *2020 International Applied Computational Electromagnetics Society Symposium (ACES)*, pages 1–2, 2020.

[34] F. Kaburcuk A. Z. Elsherbeni R. Lumnitzer A. Tanner. Electromagnetic Waves Interaction with a Human Head Model for Frequencies up to 100 GHz. *Applied Computational Electromagnetics Society (ACES) Journal*, 35(6):613–621, 2020.

[35] F. Kaburcuk Y. Chen R. Lumnitzer A. Z. Elsherbeni A. Shamim V. Demir. Human Tissues Parameters and Resolution for Accurate Simulations of Wearable Antennas. *2021 International Applied Computational Electromagnetics Society Symposium (ACES)*, pages 1–4, 2021.

[36] D. Andreuccetti. An Internet resource for the calculation of the Dielectric Properties of Body Tissues in the frequency range 10 Hz - 100 GHz, 2019. URL http://niremf.ifac.cnr.it/tissprop/.

[37] Antonio Thomson. Critical Analysis of a Practical Fourth Order Finite-Difference Time-Domain Algorithm for the Solution of Maxwell's Equations. Master's thesis, Colorado School of Mines, 2020.

[38] F. Kaburcuk and A. Z. Elsherbeni. Efficient Electromagnetic Analysis of a Dispersive Head Model Due to Smart Glasses Embedded Antennas at Wi-Fi and 5G Frequencies. *Applied Computational Electromagnetics Society (ACES) Journal*, 36(2):159–167, 2021.

APPENDIX A

HUMAN TISSUE PARAMETERS

A.1 Dielectric Properties of Human Tissues

Table A.1 Dielectric Properties of Aorta from 1 GHz to 5 GHz

Frequency [GHz]	Permittivity	Conductivity [S/m]
1	44.56	0.729
2	43.089	1.171
3	41.855	1.808
4	40.597	2.607
5	39.295	3.533

Table A.2 Dielectric Properties of Aorta from 5 GHz to 20 GHz

Frequency [GHz]	Permittivity	Conductivity [S/m]
5	39.295	3.533
6	37.963	4.556
7	36.619	5.649
8	35.28	6.787
9	33.961	7.952
10	32.673	9.127
11	31.425	10.298
12	30.223	11.456
13	29.07	12.593
14	27.97	13.703
15	26.922	14.782
16	25.926	15.827
17	24.982	16.835
18	24.089	17.807
19	23.244	18.742
20	22.445	19.64

Table A.3 Dielectric Properties of Aorta from 20 GHz to 30 GHz

Frequency [GHz]	Permittivity	Conductivity [S/m]
20	22.445	19.64
21	21.691	20.501
22	20.978	21.328
23	20.305	22.12
24	19.67	22.879
25	19.069	23.606
26	18.502	24.303
27	17.966	24.971
28	17.458	25.611
29	16.978	26.225
30	16.524	26.814

Table A.4 Dielectric Properties of Aorta from 30 GHz to 40 GHz

Frequency [GHz]	Permittivity	Conductivity [S/m]
30	16.524	26.814
31	16.093	27.379
32	15.685	27.921
33	15.298	28.442
34	14.931	28.943
35	14.581	29.424
36	14.25	29.887
37	13.934	30.333
38	13.634	30.762
39	13.348	31.176
40	13.075	31.575

Table A.5 Dielectric Properties of Aorta from 40 GHz to 90 GHz

Frequency [GHz]	Permittivity	Conductivity [S/m]
40	13.075	31.575
50	10.934	34.895
60	9.52	37.34
70	8.535	39.224
80	7.819	40.731
90	7.281	41.973

Table A.6 Dielectric Properties of Bladder from 1 GHz to 5 GHz

Frequency [GHz]	Permittivity	Conductivity [S/m]
1	18.85	0.397
2	18.234	0.578
3	17.716	0.838
4	17.2	1.161
5	16.671	1.533

Table A.7 Dielectric Properties of Bladder from 5 GHz to 20 GHz

Frequency [GHz]	Permittivity	Conductivity [S/m]
5	16.671	1.533
6	16.132	1.944
7	15.59	2.382
8	15.051	2.839
9	14.52	3.306
10	14.003	3.776
11	13.453	4.292
12	13.02	4.71
13	12.557	5.165
14	12.116	5.609
15	11.696	6.041
16	11.297	6.46
17	10.915	6.867
18	10.557	7.256
19	10.218	7.631
20	9.899	7.99

Table A.8 Dielectric Properties of Bladder from 20 GHz to 30 GHz

Frequency [GHz]	Permittivity	Conductivity [S/m]
20	9.899	7.99
21	9.596	8.335
22	9.31	8.667
23	9.04	8.984
24	8.786	9.288
25	8.545	9.58
26	8.318	9.859
27	8.103	10.127
28	7.899	10.384
29	7.707	10.63
30	7.525	10.866

Table A.9 Dielectric Properties of Bladder from 30 GHz to 40 GHz

Frequency [GHz]	Permittivity	Conductivity [S/m]
30	7.525	10.866
31	7.352	11.092
32	7.189	11.31
33	7.033	11.518
34	6.886	11.719
35	6.746	11.912
36	6.613	12.098
37	6.487	12.277
38	6.366	12.449
39	6.252	12.615
40	6.142	12.775

Table A.10 Dielectric Properties of Bladder from 40 GHz to 90 GHz

Frequency [GHz]	Permittivity	Conductivity [S/m]
40	6.142	12.775
50	5.284	14.107
60	4.717	15.088
70	4.322	15.844
80	4.035	16.45
90	3.819	16.949

Table A.11 Dielectric Properties of Blood Vessel from 1 GHz to 5 GHz

Frequency [GHz]	Permittivity	Conductivity [S/m]
1	44.560	0.729
2	43.089	1.171
3	41.845	1.814
4	40.588	2.613
5	39.287	3.539

Table A.12 Dielectric Properties of Blood Vessel from 5 GHz to 20 GHz

Frequency [GHz]	Permittivity	Conductivity [S/m]
5	39.287	3.539
6	37.956	4.562
7	36.613	5.653
8	35.276	6.791
9	33.958	7.955
10	32.672	9.128
11	31.425	10.298
12	30.214	11.466
13	29.062	12.601
14	27.963	13.710
15	26.916	14.787
16	25.922	15.831
17	24.979	16.838
18	24.087	17.809
19	23.243	18.743
20	22.445	19.640

Table A.13 Dielectric Properties of Blood Vessel from 20 GHz to 30 GHz

Frequency [GHz]	Permittivity	Conductivity [S/m]
20	22.445	19.640
21	21.691	20.501
22	20.978	21.328
23	20.305	22.120
24	19.670	22.879
25	19.069	23.606
26	18.502	24.303
27	17.966	24.971
28	17.458	25.611
29	16.978	26.225
30	16.524	26.814

Table A.14 Dielectric Properties of Blood Vessel from 30 GHz to 40 GHz

Frequency [GHz]	Permittivity	Conductivity [S/m]
30	16.524	26.814
31	16.093	27.379
32	15.685	27.921
33	15.298	28.442
34	14.931	28.943
35	14.581	29.424
36	14.250	29.887
37	13.934	30.333
38	13.634	30.762
39	13.348	31.176
40	13.075	31.575

Table A.15 Dielectric Properties of Blood Vessel from 40 GHz to 90 GHz

Frequency [GHz]	Permittivity	Conductivity [S/m]
40	13.075	31.575
50	10.934	34.895
60	9.520	37.340
70	8.535	39.224
80	7.819	40.731
90	7.281	41.973

Table A.16 Dielectric Properties of Body Fluid from 1 GHz to 5 GHz

Frequency [GHz]	Permittivity	Conductivity [S/m]
1	68.875	1.668
2	68.472	2.156
3	67.811	2.963
4	66.916	4.058
5	65.803	5.420

Table A.17 Dielectric Properties of Body Fluid from 5 GHz to 20 GHz

Frequency [GHz]	Permittivity	Conductivity [S/m]
5	65.803	5.420
6	64.495	7.020
7	63.020	8.825
8	61.406	10.801
9	59.680	12.913
10	57.870	15.128
11	56.002	17.414
12	54.082	19.764
13	52.166	22.109
14	50.255	24.448
15	48.365	26.761
16	46.508	29.034
17	44.695	31.253
18	42.934	33.408
19	41.231	35.493
20	39.590	37.501

Table A.18 Dielectric Properties of Body Fluid from 20 GHz to 30 GHz

Frequency [GHz]	Permittivity	Conductivity [S/m]
20	39.590	37.501
21	38.013	39.432
22	36.502	41.281
23	35.058	43.048
24	33.681	44.733
25	32.370	46.338
26	31.123	47.865
27	29.938	49.315
28	28.813	50.692
29	27.745	51.999
30	26.733	53.238

Table A.19 Dielectric Properties of Body Fluid from 30 GHz to 40 GHz

Frequency [GHz]	Permittivity	Conductivity [S/m]
30	26.733	53.238
31	25.773	54.412
32	24.864	55.525
33	24.002	56.581
34	23.184	57.581
35	22.410	58.529
36	21.676	59.427
37	20.979	60.280
38	20.319	61.088
39	19.692	61.855
40	19.097	62.583

Table A.20 Dielectric Properties of Body Fluid from 40 GHz to 90 GHz

Frequency [GHz]	Permittivity	Conductivity [S/m]
40	19.097	62.583
50	14.544	68.156
60	11.704	71.632
70	9.844	73.909
80	8.571	75.467
90	7.665	76.575

Table A.21 Dielectric Properties of Bone Cancellous from 1 GHz to 5 GHz

Frequency [GHz]	Permittivity	Conductivity [S/m]
1	20.583	0.364
2	19.086	0.652
3	17.935	1.009
4	16.939	1.402
5	16.045	1.814

Table A.22 Dielectric Properties of Bone Cancellous from 5 GHz to 20 GHz

Frequency [GHz]	Permittivity	Conductivity [S/m]
5	16.045	1.814
6	15.235	2.234
7	14.499	2.653
8	13.829	3.066
9	13.218	3.468
10	12.661	3.860
11	12.150	4.238
12	11.679	4.605
13	11.249	4.956
14	10.854	5.293
15	10.489	5.617
16	10.152	5.929
17	9.840	6.228
18	9.550	6.516
19	9.281	6.792
20	9.030	7.059

Table A.23 Dielectric Properties of Bone Cancellous from 20 GHz to 30 GHz

Frequency [GHz]	Permittivity	Conductivity [S/m]
20	9.030	7.059
21	8.795	7.315
22	8.576	7.563
23	8.370	7.801
24	8.177	8.031
25	7.996	8.253
26	7.826	8.468
27	7.665	8.675
28	7.513	8.876
29	7.370	9.071
30	7.234	9.259

Table A.24 Dielectric Properties of Bone Cancellous from 30 GHz to 40 GHz

Frequency [GHz]	Permittivity	Conductivity [S/m]
30	7.234	9.259
31	7.106	9.442
32	6.983	9.620
33	6.867	9.792
34	6.757	9.960
35	6.652	10.123
36	6.552	10.281
37	6.457	10.436
38	6.366	10.586
39	6.279	10.733
40	6.196	10.876

Table A.25 Dielectric Properties of Bone Cancellous from 40 GHz to 90 GHz

Frequency [GHz]	Permittivity	Conductivity [S/m]
40	6.196	10.876
50	5.528	12.137
60	5.065	13.167
70	4.726	14.036
80	4.468	14.787
90	4.266	15.449

Table A.26 Dielectric Properties of Brain Grey Matter from 1 GHz to 5 GHz

Frequency [GHz]	Permittivity	Conductivity [S/m]
1	52.280	0.986
2	49.692	1.511
3	48.037	2.225
4	46.570	3.097
5	45.138	4.106

Table A.27 Dielectric Properties of Brain Grey Matter from 5 GHz to 20 GHz

Frequency [GHz]	Permittivity	Conductivity [S/m]
5	45.138	4.106
6	43.712	5.223
7	42.288	6.424
8	40.874	7.685
9	39.479	8.987
10	38.111	10.311
11	36.777	11.645
12	35.472	12.987
13	34.222	14.305
14	33.020	15.603
15	31.866	16.875
16	30.762	18.117
17	29.708	19.325
18	28.703	20.498
19	27.745	21.634
20	26.834	22.732

Table A.28 Dielectric Properties of Brain Grey Matter from 20 GHz to 30 GHz

Frequency [GHz]	Permittivity	Conductivity [S/m]
20	26.834	22.732
21	25.967	23.794
22	25.143	24.818
23	24.361	25.805
24	23.618	26.755
25	22.912	27.670
26	22.242	28.551
27	21.606	29.399
28	21.002	30.214
29	20.427	30.999
30	19.881	31.755

Table A.29 Dielectric Properties of Brain Grey Matter from 30 GHz to 40 GHz

Frequency [GHz]	Permittivity	Conductivity [S/m]
30	19.881	31.755
31	19.362	32.482
32	18.867	33.183
33	18.397	33.858
34	17.949	34.508
35	17.522	35.134
36	17.116	35.738
37	16.728	36.321
38	16.357	36.884
39	16.004	37.427
40	15.666	37.952

Table A.30 Dielectric Properties of Brain Grey Matter from 40 GHz to 90 GHz

Frequency [GHz]	Permittivity	Conductivity [S/m]
40	15.666	37.952
50	12.986	42.350
60	11.188	45.617
70	9.924	48.144
80	8.998	5.017
90	8.299	5.184

Table A.31 Dielectric Properties of Brain White Matter from 1 GHz to 5 GHz

Frequency [GHz]	Permittivity	Conductivity [S/m]
1	38.576	0.622
2	36.732	1.001
3	35.532	1.515
4	34.471	2.141
5	33.437	2.863

Table A.32 Dielectric Properties of Brain White Matter from 5 GHz to 20 GHz

Frequency [GHz]	Permittivity	Conductivity [S/m]
5	33.437	2.863
6	32.411	3.663
7	31.388	4.522
8	30.374	54.229
9	29.374	63.526
10	28.394	7.299
11	27.440	8.251
12	26.506	9.209
13	25.613	10.150
14	24.754	11.077
15	23.930	11.985
16	23.142	12.871
17	22.389	13.733
18	21.671	14.571
19	20.987	15.381
20	20.337	16.165

Table A.33 Dielectric Properties of Brain White Matter from 20 GHz to 30 GHz

Frequency [GHz]	Permittivity	Conductivity [S/m]
20	20.337	16.165
21	19.718	16.923
22	19.130	17.654
23	18.571	18.359
24	18.041	19.037
25	17.537	19.691
26	17.059	20.320
27	16.605	20.925
28	16.173	21.508
29	15.763	22.068
30	15.374	22.608

Table A.34 Dielectric Properties of Brain White Matter from 30 GHz to 40 GHz

Frequency [GHz]	Permittivity	Conductivity [S/m]
30	15.374	22.608
31	15.003	23.128
32	14.650	23.628
33	14.314	24.110
34	13.995	24.575
35	13.690	25.023
36	13.400	25.455
37	13.123	25.871
38	12.858	26.274
39	12.606	26.662
40	12.365	27.037

Table A.35 Dielectric Properties of Brain White Matter from 40 GHz to 90 GHz

Frequency [GHz]	Permittivity	Conductivity [S/m]
40	12.365	27.037
50	10.451	30.185
60	9.167	32.525
70	8.263	34.339
80	7.602	35.794
90	7.101	36.995

Table A.36 Dielectric Properties of Breast Fat from 1 GHz to 5 GHz

Frequency [GHz]	Permittivity	Conductivity [S/m]
1	5.408	0.053
2	5.232	0.106
3	5.037	0.180
4	4.838	0.263
5	4.644	0.350

Table A.37 Dielectric Properties of Breast Fat from 5 GHz to 20 GHz

Frequency [GHz]	Permittivity	Conductivity [S/m]
5	4.644	0.350
6	4.461	0.437
7	4.293	0.521
8	4.140	0.601
9	4.003	0.675
10	3.880	0.743
11	3.771	0.807
12	3.672	0.865
13	3.585	0.918
14	3.507	0.967
15	3.437	1.012
16	3.374	1.054
17	3.318	1.092
18	3.267	1.127
19	3.221	1.160
20	3.179	1.190

Table A.38 Dielectric Properties of Breast Fat from 20 GHz to 30 GHz

Frequency [GHz]	Permittivity	Conductivity [S/m]
20	3.179	1.190
21	3.141	1.219
22	3.106	1.245
23	3.075	1.270
24	3.045	1.293
25	3.019	1.315
26	2.994	1.335
27	2.971	1.354
28	2.950	1.372
29	2.931	1.390
30	2.913	1.406

Table A.39 Dielectric Properties of Breast Fat from 30 GHz to 40 GHz

Frequency [GHz]	Permittivity	Conductivity [S/m]
30	2.913	1.406
31	2.900	1.422
32	2.880	1.436
33	2.866	1.450
34	2.852	1.464
35	2.839	1.476
36	2.827	1.489
37	2.816	1.500
38	2.805	1.512
39	2.795	1.522
40	2.785	1.533

Table A.40 Dielectric Properties of Breast Fat from 40 GHz to 90 GHz

Frequency [GHz]	Permittivity	Conductivity [S/m]
40	2.785	1.533
50	2.714	1.618
60	2.669	1.682
70	2.639	1.731
80	2.618	1.772
90	2.602	1.806

Table A.41 Dielectric Properties of Cartilage from 1 GHz to 5 GHz

Frequency [GHz]	Permittivity	Conductivity [S/m]
1	42.315	0.829
2	39.759	1.423
3	37.589	2.212
4	35.553	3.116
5	33.614	4.091

Table A.42 Dielectric Properties of Cartilage from 5 GHz to 20 GHz

Frequency [GHz]	Permittivity	Conductivity [S/m]
5	33.614	4.091
6	31.782	5.099
7	30.066	6.112
8	28.469	7.111
9	26.992	8.084
10	25.629	9.024
11	24.374	9.925
12	23.211	10.793
13	22.151	11.612
14	21.177	12.391
15	20.280	13.130
16	19.455	13.832
17	18.693	14.498
18	17.991	15.130
19	17.341	15.730
20	16.739	16.301

Table A.43 Dielectric Properties of Cartilage from 20 GHz to 30 GHz

Frequency [GHz]	Permittivity	Conductivity [S/m]
20	16.739	16.301
21	16.180	16.844
22	15.661	17.360
23	15.178	17.853
24	14.727	18.322
25	14.307	18.771
26	13.915	19.199
27	13.547	19.609
28	13.202	20.002
29	12.879	20.378
30	12.575	20.739

Table A.44 Dielectric Properties of Cartilage from 30 GHz to 40 GHz

Frequency [GHz]	Permittivity	Conductivity [S/m]
30	12.575	20.739
31	12.288	21.086
32	12.018	21.419
33	11.764	21.740
34	11.523	22.049
35	11.295	22.347
36	11.080	22.635
37	10.875	22.912
38	10.681	23.181
39	10.496	23.440
40	10.321	23.692

Table A.45 Dielectric Properties of Cartilage from 40 GHz to 90 GHz

Frequency [GHz]	Permittivity	Conductivity [S/m]
40	10.321	23.692
50	8.951	25.831
60	8.045	27.482
70	7.408	28.816
80	6.938	29.930
90	6.580	30.885

Table A.46 Dielectric Properties of Cerebellum from 1 GHz to 5 GHz

Frequency [GHz]	Permittivity	Conductivity [S/m]
1	48.855	1.308
2	45.668	1.823
3	43.883	2.488
4	42.417	3.286
5	41.045	4.200

Table A.47 Dielectric Properties of Cerebellum from 5 GHz to 20 GHz

Frequency [GHz]	Permittivity	Conductivity [S/m]
5	41.045	4.200
6	39.708	5.208
7	38.392	6.289
8	37.097	7.422
9	35.826	8.589
10	34.586	9.776
11	33.379	10.970
12	32.201	12.172
13	31.076	13.351
14	29.995	14.511
15	28.958	15.649
16	27.967	16.759
17	27.021	17.839
18	26.119	18.887
19	25.261	19.902
20	24.444	20.884

Table A.48 Dielectric Properties of Cerebellum from 20 GHz to 30 GHz

Frequency [GHz]	Permittivity	Conductivity [S/m]
20	24.444	20.884
21	23.668	21.833
22	22.930	22.747
23	22.230	23.629
24	21.565	24.479
25	20.933	25.296
26	20.334	26.083
27	19.764	26.841
28	19.223	27.570
29	18.709	28.271
30	18.221	28.947

Table A.49 Dielectric Properties of Cerebellum from 30 GHz to 40 GHz

Frequency [GHz]	Permittivity	Conductivity [S/m]
30	18.221	28.947
31	17.756	29.597
32	17.315	30.223
33	16.894	30.826
34	16.493	31.407
35	16.112	31.967
36	15.748	32.508
37	15.401	33.029
38	15.070	33.532
39	14.754	34.018
40	14.452	34.487

Table A.50 Dielectric Properties of Cerebellum from 40 GHz to 90 GHz

Frequency [GHz]	Permittivity	Conductivity [S/m]
40	14.452	34.487
50	12.055	38.422
60	10.448	41.348
70	9.317	43.613
80	8.489	45.430
90	7.863	46.929

Table A.51 Dielectric Properties of Cerebral Spinal Fluid from 1 GHz to 5 GHz

Frequency [GHz]	Permittivity	Conductivity [S/m]
1	68.437	2.455
2	66.910	3.074
3	65.378	4.014
4	63.718	5.205
5	61.941	6.606

Table A.52 Dielectric Properties of Cerebral Spinal Fluid from 5 GHz to 20 GHz

Frequency [GHz]	Permittivity	Conductivity [S/m]
5	61.941	6.606
6	60.083	8.172
7	58.176	9.866
8	56.250	11.650
9	54.327	13.497
10	52.426	15.380
11	50.562	17.278
12	48.730	19.191
13	46.971	21.071
14	45.274	22.923
15	43.643	24.738
16	42.079	26.512
17	40.584	28.238
18	39.156	29.914
19	37.796	31.537
20	36.500	33.106

Table A.53 Dielectric Properties of Cerebral Spinal Fluid from 20 GHz to 30 GHz

Frequency [GHz]	Permittivity	Conductivity [S/m]
20	36.500	33.106
21	35.267	34.623
22	34.094	36.087
23	32.980	37.497
24	31.921	38.856
25	30.916	40.163
26	29.960	41.422
27	29.053	42.633
28	28.191	43.798
29	27.371	44.920
30	26.592	45.999

Table A.54 Dielectric Properties of Cerebral Spinal Fluid from 30 GHz to 40 GHz

Frequency [GHz]	Permittivity	Conductivity [S/m]
30	26.592	45.999
31	25.851	47.038
32	25.146	48.038
33	24.474	49.002
34	23.835	49.930
35	23.226	50.824
36	22.645	51.687
37	22.091	52.519
38	21.563	53.321
39	21.058	54.096
40	20.576	54.844

Table A.55 Dielectric Properties of Cerebral Spinal Fluid from 40 GHz to 90 GHz

Frequency [GHz]	Permittivity	Conductivity [S/m]
40	20.576	54.844
50	16.750	61.111
60	14.184	65.757
70	12.381	69.344
80	11.063	72.212
90	10.067	74.571

Table A.56 Dielectric Properties of Cervix from 1 GHz to 5 GHz

Frequency [GHz]	Permittivity	Conductivity [S/m]
1	49.582	0.993
2	48.161	1.451
3	46.946	2.115
4	45.706	2.953
5	44.416	3.935

Table A.57 Dielectric Properties of Cervix from 5 GHz to 20 GHz

Frequency [GHz]	Permittivity	Conductivity [S/m]
5	44.416	3.935
6	43.088	5.030
7	41.736	6.211
8	40.378	7.455
9	39.026	8.742
10	37.693	10.053
11	36.389	11.374
12	35.120	12.693
13	33.891	14.000
14	32.707	15.288
15	31.569	16.551
16	30.479	17.784
17	29.437	18.984
18	28.443	20.149
19	27.495	21.278
20	26.593	22.369

Table A.58 Dielectric Properties of Cervix from 20 GHz to 30 GHz

Frequency [GHz]	Permittivity	Conductivity [S/m]
20	26.593	22.369
21	25.736	23.422
22	24.920	24.439
23	24.146	25.418
24	23.410	26.361
25	22.711	27.269
26	22.047	28.143
27	21.417	28.984
28	20.817	29.794
29	20.248	30.572
30	19.707	31.322

Table A.59 Dielectric Properties of Cervix from 30 GHz to 40 GHz

Frequency [GHz]	Permittivity	Conductivity [S/m]
30	19.707	31.322
31	19.192	32.043
32	18.702	32.738
33	18.236	33.407
34	17.792	34.052
35	17.368	34.673
36	16.965	35.272
37	16.580	35.850
38	16.213	36.408
39	15.862	36.946
40	15.527	37.466

Table A.60 Dielectric Properties of Cervix from 40 GHz to 90 GHz

Frequency [GHz]	Permittivity	Conductivity [S/m]
40	15.527	37.466
50	12.870	41.821
60	11.088	45.051
70	9.835	47.546
80	8.919	49.542
90	8.227	51.185

Table A.61 Dielectric Properties of Colon from 1 GHz to 5 GHz

Frequency [GHz]	Permittivity	Conductivity [S/m]
1	57.482	1.127
2	54.729	1.709
3	52.932	2.495
4	51.310	3.464
5	49.723	4.585

Table A.62 Dielectric Properties of Colon from 5 GHz to 20 GHz

Frequency [GHz]	Permittivity	Conductivity [S/m]
5	49.723	4.585
6	48.139	5.827
7	46.557	7.162
8	44.985	8.565
9	43.434	10.013
10	41.912	11.486
11	40.429	12.970
12	38.990	14.450
13	37.600	15.916
14	36.262	17.360
15	34.979	18.775
16	33.750	20.157
17	32.577	21.502
18	31.459	22.806
19	30.394	24.070
20	29.380	25.292

Table A.63 Dielectric Properties of Colon from 20 GHz to 30 GHz

Frequency [GHz]	Permittivity	Conductivity [S/m]
20	29.380	25.292
21	28.417	26.472
22	27.501	27.610
23	26.632	28.707
24	25.806	29.763
25	25.022	30.780
26	24.278	31.759
27	23.571	32.701
28	22.899	33.608
29	22.260	34.480
30	21.653	35.320

Table A.64 Dielectric Properties of Colon from 30 GHz to 40 GHz

Frequency [GHz]	Permittivity	Conductivity [S/m]
30	21.653	35.320
31	21.076	36.128
32	20.527	36.907
33	20.004	37.657
34	19.507	38.379
35	19.032	39.076
36	18.580	39.747
37	18.149	40.395
38	17.737	41.021
39	17.344	41.624
40	16.969	42.207

Table A.65 Dielectric Properties of Colon from 40 GHz to 90 GHz

Frequency [GHz]	Permittivity	Conductivity [S/m]
40	16.969	42.207
50	13.990	47.097
60	11.992	50.728
70	10.587	53.538
80	9.559	55.790
90	8.782	57.646

Table A.66 Dielectric Properties of Cornea from 1 GHz to 5 GHz

Frequency [GHz]	Permittivity	Conductivity [S/m]
1	54.835	1.438
2	52.390	1.984
3	50.742	2.729
4	49.229	3.652
5	47.733	4.722

Table A.67 Dielectric Properties of Cornea from 5 GHz to 20 GHz

Frequency [GHz]	Permittivity	Conductivity [S/m]
5	47.733	4.722
6	46.232	5.910
7	44.728	7.188
8	43.231	8.530
9	41.751	9.916
10	40.298	11.327
11	38.881	12.748
12	37.505	14.166
13	36.175	15.571
14	34.895	16.955
15	33.667	18.311
16	32.491	19.635
17	31.368	20.923
18	30.297	22.174
19	29.277	23.385
20	28.306	24.556

Table A.68 Dielectric Properties of Cornea from 20 GHz to 30 GHz

Frequency [GHz]	Permittivity	Conductivity [S/m]
20	28.306	24.556
21	27.384	25.687
22	26.507	26.777
23	25.674	27.828
24	24.883	28.841
25	24.132	29.815
26	23.418	30.753
27	22.741	31.656
28	22.097	32.525
29	21.485	33.361
30	20.904	34.166

Table A.69 Dielectric Properties of Cornea from 30 GHz to 40 GHz

Frequency [GHz]	Permittivity	Conductivity [S/m]
30	20.904	34.166
31	20.351	34.940
32	19.825	35.686
33	19.324	36.405
34	18.847	37.097
35	18.392	37.765
36	17.959	38.408
37	17.546	39.029
38	17.151	39.628
39	16.775	40.206
40	16.415	40.765

Table A.70 Dielectric Properties of Cornea from 40 GHz to 90 GHz

Frequency [GHz]	Permittivity	Conductivity [S/m]
40	16.415	40.765
50	13.561	45.448
60	11.647	48.924
70	10.300	51.614
80	9.316	53.768
90	8.571	55.543

Table A.71 Dielectric Properties of Duodenum from 1 GHz to 5 GHz

Frequency [GHz]	Permittivity	Conductivity [S/m]
1	64.797	1.232
2	62.892	1.844
3	61.268	2.729
4	59.611	3.848
5	57.890	5.157

Table A.72 Dielectric Properties of Duodenum from 5 GHz to 20 GHz

Frequency [GHz]	Permittivity	Conductivity [S/m]
5	57.890	5.157
6	56.118	6.617
7	54.315	8.192
8	52.503	9.851
9	50.700	11.566
10	48.923	13.314
11	47.184	15.075
12	45.491	16.834
13	43.853	18.577
14	42.274	20.295
15	40.757	21.978
16	39.304	23.623
17	37.914	25.223
18	36.588	26.776
19	35.325	28.280
20	34.123	29.735

Table A.73 Dielectric Properties of Duodenum from 20 GHz to 30 GHz

Frequency [GHz]	Permittivity	Conductivity [S/m]
20	34.123	29.735
21	32.979	31.140
22	31.892	32.495
23	30.859	33.800
24	29.878	35.058
25	28.946	36.269
26	28.061	37.434
27	27.220	38.555
28	26.421	39.634
29	25.662	40.673
30	24.940	41.672

Table A.74 Dielectric Properties of Duodenum from 30 GHz to 40 GHz

Frequency [GHz]	Permittivity	Conductivity [S/m]
30	24.940	41.672
31	24.254	42.634
32	23.601	43.560
33	22.979	44.452
34	22.387	45.312
35	21.823	46.140
36	21.285	46.939
37	20.772	47.709
38	20.282	48.453
39	19.815	49.170
40	19.368	49.863

Table A.75 Dielectric Properties of Duodenum from 40 GHz to 90 GHz

Frequency [GHz]	Permittivity	Conductivity [S/m]
40	19.368	49.863
50	15.825	55.670
60	13.449	59.975
70	11.778	63.302
80	10.557	65.964
90	9.634	68.154

Table A.76 Dielectric Properties of Duodenum from 1 GHz to 5 GHz

Frequency [GHz]	Permittivity	Conductivity [S/m]
1	44.201	0.993
2	42.622	1.420
3	41.340	2.015
4	40.096	2.746
5	38.859	3.582

Table A.77 Dielectric Properties of Dura from 5 GHz to 20 GHz

Frequency [GHz]	Permittivity	Conductivity [S/m]
5	38.859	3.582
6	37.632	4.498
7	36.421	5.473
8	35.235	6.488
9	34.081	7.529
10	32.963	8.584
11	31.884	9.643
12	30.848	10.698
13	29.854	11.743
14	28.904	12.773
15	27.997	13.785
16	27.132	14.775
17	26.308	15.743
18	25.523	16.686
19	24.777	17.604
20	24.067	18.497

Table A.78 Dielectric Properties of Dura from 20 GHz to 30 GHz

Frequency [GHz]	Permittivity	Conductivity [S/m]
20	24.067	18.497
21	23.392	19.363
22	22.750	20.204
23	22.139	21.020
24	21.558	21.810
25	21.006	22.577
26	20.479	23.319
27	19.978	24.039
28	19.500	24.736
29	19.045	25.412
30	18.611	26.067

Table A.79 Dielectric Properties of Dura from 30 GHz to 40 GHz

Frequency [GHz]	Permittivity	Conductivity [S/m]
30	18.611	26.067
31	18.197	26.702
32	17.802	27.318
33	17.424	27.915
34	17.063	28.494
35	16.718	29.056
36	16.388	29.602
37	16.071	30.132
38	15.769	30.647
39	15.478	31.147
40	15.200	31.634

Table A.80 Dielectric Properties of Dura from 40 GHz to 90 GHz

Frequency [GHz]	Permittivity	Conductivity [S/m]
40	15.200	31.634
50	12.950	35.845
60	11.386	39.146
70	10.252	41.819
80	9.400	44.044
90	8.739	45.937

Table A.81 Dielectric Properties of Eye Sclera from 1 GHz to 5 GHz

Frequency [GHz]	Permittivity	Conductivity [S/m]
1	55.017	1.206
2	53.271	1.725
3	51.859	2.468
4	50.448	3.404
5	48.996	4.499

Table A.82 Dielectric Properties of Eye Sclera from 5 GHz to 20 GHz

Frequency [GHz]	Permittivity	Conductivity [S/m]
5	48.996	4.499
6	47.506	5.718
7	45.994	7.033
8	44.477	8.418
9	42.969	9.849
10	41.484	11.308
11	40.030	12.777
12	38.617	14.244
13	37.249	15.698
14	35.931	17.131
15	34.664	18.535
16	33.451	19.906
17	32.292	21.241
18	31.186	22.536
19	30.132	23.791
20	29.128	25.004

Table A.83 Dielectric Properties of Eye Sclera from 20 GHz to 30 GHz

Frequency [GHz]	Permittivity	Conductivity [S/m]
20	29.128	25.004
21	28.174	26.175
22	27.267	27.305
23	26.406	28.394
24	25.587	29.443
25	24.810	30.453
26	24.072	31.424
27	23.370	32.360
28	22.704	33.260
29	22.071	34.126
30	21.469	34.959

Table A.84 Dielectric Properties of Eye Sclera from 30 GHz to 40 GHz

Frequency [GHz]	Permittivity	Conductivity [S/m]
30	21.469	34.959
31	20.896	35.761
32	20.351	36.534
33	19.833	37.278
34	19.339	37.995
35	18.868	38.685
36	18.420	39.352
37	17.992	39.994
38	17.584	40.614
39	17.194	41.213
40	16.821	41.791

Table A.85 Dielectric Properties of Eye Sclera from 40 GHz to 90 GHz

Frequency [GHz]	Permittivity	Conductivity [S/m]
40	16.821	41.791
50	13.866	46.634
60	11.884	50.226
70	10.491	53.002
80	9.472	55.222
90	8.702	57.050

Table A.86 Dielectric Properties of Gall Bladder from 1 GHz to 5 GHz

Frequency [GHz]	Permittivity	Conductivity [S/m]
1	58.997	1.288
2	58.039	1.758
3	57.100	2.496
4	56.006	3.472
5	54.763	4.653

Table A.87 Dielectric Properties of Gall Bladder from 5 GHz to 20 GHz

Frequency [GHz]	Permittivity	Conductivity [S/m]
5	54.763	4.653
6	53.398	6.006
7	51.936	7.500
8	50.405	9.104
9	48.829	10.788
10	47.229	12.528
11	45.623	14.301
12	44.027	16.087
13	42.454	17.869
14	40.913	19.634
15	39.414	21.370
16	37.961	23.068
17	36.560	24.723
18	35.212	26.328
19	33.919	27.881
20	32.682	29.380

Table A.88 Dielectric Properties of Gall Bladder from 20 GHz to 30 GHz

Frequency [GHz]	Permittivity	Conductivity [S/m]
20	32.682	29.380
21	31.501	30.822
22	30.374	32.208
23	29.302	33.538
24	28.281	34.813
25	27.311	36.034
26	26.389	37.202
27	25.513	38.319
28	24.682	39.388
29	23.892	40.409
30	23.143	41.386

Table A.89 Dielectric Properties of Gall Bladder from 30 GHz to 40 GHz

Frequency [GHz]	Permittivity	Conductivity [S/m]
30	23.143	41.386
31	22.431	42.319
32	21.755	43.211
33	21.113	44.065
34	20.503	44.881
35	19.923	45.661
36	19.372	46.408
37	18.848	47.124
38	18.348	47.809
39	17.873	48.465
40	17.421	49.094

Table A.90 Dielectric Properties of Gall Bladder from 40 GHz to 90 GHz

Frequency [GHz]	Permittivity	Conductivity [S/m]
40	17.421	49.094
50	13.890	54.164
60	11.601	57.666
70	10.043	60.203
80	8.937	62.119
90	8.124	63.618

Table A.91 Dielectric Properties of Gall Bladder Bile from 1 GHz to 5 GHz

Frequency [GHz]	Permittivity	Conductivity [S/m]
1	70.010	1.876
2	68.849	2.440
3	67.719	3.325
4	66.406	4.496
5	64.915	5.913

Table A.92 Dielectric Properties of Gall Bladder Bile from 5 GHz to 20 GHz

Frequency [GHz]	Permittivity	Conductivity [S/m]
5	64.915	5.913
6	63.277	7.537
7	61.523	9.330
8	59.686	11.254
9	57.794	13.276
10	55.874	15.364
11	53.947	17.491
12	52.032	19.634
13	50.144	21.772
14	48.296	23.890
15	46.496	25.973
16	44.753	28.011
17	43.071	29.997
18	41.454	31.923
19	39.902	33.787
20	38.418	35.585

Table A.93 Dielectric Properties of Gall Bladder Bile from 20 GHz to 30 GHz

Frequency [GHz]	Permittivity	Conductivity [S/m]
20	38.418	35.585
21	37.000	37.316
22	35.649	38.979
23	34.362	40.575
24	33.137	42.105
25	31.973	43.570
26	30.866	44.971
27	29.816	46.312
28	28.818	47.595
29	27.871	48.820
30	26.971	49.992

Table A.94 Dielectric Properties of Gall Bladder Bile from 30 GHz to 40 GHz

Frequency [GHz]	Permittivity	Conductivity [S/m]
30	26.971	49.992
31	26.117	51.112
32	25.306	52.183
33	24.535	53.207
34	23.803	54.186
35	23.108	55.123
36	22.446	56.019
37	21.817	56.877
38	21.218	57.699
39	20.648	58.487
40	20.105	59.242

Table A.95 Dielectric Properties of Gall Bladder Bile from 40 GHz to 90 GHz

Frequency [GHz]	Permittivity	Conductivity [S/m]
40	20.105	59.242
50	15.868	65.326
60	13.121	69.528
70	11.251	72.572
80	9.924	74.871
90	8.949	76.670

Table A.96 Dielectric Properties of Gland from 1 GHz to 5 GHz

Frequency [GHz]	Permittivity	Conductivity [S/m]
1	59.470	1.079
2	57.850	1.633
3	56.403	2.441
4	54.906	3.464
5	53.342	4.661

Table A.97 Dielectric Properties of Gland from 5 GHz to 20 GHz

Frequency [GHz]	Permittivity	Conductivity [S/m]
5	53.342	4.661
6	51.726	5.998
7	50.080	7.440
8	48.424	8.960
9	46.776	10.531
10	45.150	12.132
11	43.558	13.746
12	42.008	15.357
13	40.509	16.954
14	39.063	18.527
15	37.673	20.070
16	36.342	21.576
17	35.070	23.043
18	33.855	24.466
19	32.698	25.844
20	31.597	27.177

Table A.98 Dielectric Properties of Gland from 20 GHz to 30 GHz

Frequency [GHz]	Permittivity	Conductivity [S/m]
20	31.597	27.177
21	30.549	28.464
22	29.553	29.706
23	28.607	30.902
24	27.708	32.054
25	26.855	33.164
26	26.044	34.232
27	25.273	35.259
28	24.542	36.248
29	23.846	37.199
30	23.185	38.115

Table A.99 Dielectric Properties of Gland from 30 GHz to 40 GHz

Frequency [GHz]	Permittivity	Conductivity [S/m]
30	23.185	38.115
31	22.556	38.996
32	21.957	39.845
33	21.388	40.662
34	20.845	41.450
35	20.328	42.209
36	19.835	42.941
37	19.365	43.646
38	18.917	44.328
39	18.488	44.985
40	18.079	45.620

Table A.100 Dielectric Properties of Gland from 40 GHz to 90 GHz

Frequency [GHz]	Permittivity	Conductivity [S/m]
40	18.079	45.620
50	14.833	50.940
60	12.656	54.885
70	11.125	57.933
80	10.006	60.370
90	9.161	62.377

Table A.101 Dielectric Properties of Heart from 1 GHz to 5 GHz

Frequency [GHz]	Permittivity	Conductivity [S/m]
1	59.290	1.284
2	55.816	1.912
3	53.737	2.729
4	51.961	3.722
5	50.274	4.863

Table A.102 Dielectric Properties of Heart from 5 GHz to 20 GHz

Frequency [GHz]	Permittivity	Conductivity [S/m]
5	50.274	4.863
6	48.620	6.122
7	46.986	7.473
8	45.374	8.889
9	43.790	10.350
10	42.241	11.835
11	40.735	13.329
12	39.277	14.819
13	37.870	16.295
14	36.518	17.747
15	35.222	19.171
16	33.982	20.561
17	32.799	21.913
18	31.671	23.225
19	30.597	24.496
20	29.576	25.724

Table A.103 Dielectric Properties of Heart from 20 GHz to 30 GHz

Frequency [GHz]	Permittivity	Conductivity [S/m]
20	29.576	25.724
21	28.606	26.910
22	27.684	28.055
23	26.809	29.157
24	25.978	30.220
25	25.188	31.242
26	24.439	32.227
27	23.727	33.174
28	23.051	34.086
29	22.409	34.963
30	21.798	35.808

Table A.104 Dielectric Properties of Heart from 30 GHz to 40 GHz

Frequency [GHz]	Permittivity	Conductivity [S/m]
30	21.798	35.808
31	21.218	36.622
32	20.665	37.405
33	20.139	38.159
34	19.639	38.886
35	19.161	39.587
36	18.707	40.263
37	18.273	40.915
38	17.859	41.544
39	17.464	42.152
40	17.086	42.739

Table A.105 Dielectric Properties of Heart from 40 GHz to 90 GHz

Frequency [GHz]	Permittivity	Conductivity [S/m]
40	17.086	42.739
50	14.089	47.665
60	12.078	51.327
70	10.664	54.165
80	9.628	56.441
90	8.845	58.319

Table A.106 Dielectric Properties of Kidney from 1 GHz to 5 GHz

Frequency [GHz]	Permittivity	Conductivity [S/m]
1	57.939	1.450
2	53.852	2.090
3	51.588	2.891
4	49.751	3.849
5	48.059	4.942

Table A.107 Dielectric Properties of Kidney from 5 GHz to 20 GHz

Frequency [GHz]	Permittivity	Conductivity [S/m]
5	48.059	4.942
6	46.430	6.144
7	44.839	7.429
8	43.281	8.775
9	41.758	10.160
10	40.275	11.567
11	38.836	12.983
12	37.445	14.393
13	36.106	15.790
14	34.820	17.164
15	33.588	18.511
16	32.411	19.825
17	31.288	21.103
18	30.219	22.344
19	29.201	23.545
20	28.234	24.707

Table A.108 Dielectric Properties of Kidney from 20 GHz to 30 GHz

Frequency [GHz]	Permittivity	Conductivity [S/m]
20	28.234	24.707
21	27.314	25.828
22	26.441	26.910
23	25.612	27.953
24	24.825	28.957
25	24.078	29.924
26	23.369	30.855
27	22.696	31.750
28	22.056	32.613
29	21.448	33.442
30	20.870	34.241

Table A.109 Dielectric Properties of Kidney from 30 GHz to 40 GHz

Frequency [GHz]	Permittivity	Conductivity [S/m]
30	20.870	34.241
31	20.321	35.010
32	19.798	35.751
33	19.301	36.465
34	18.827	37.153
35	18.376	37.816
36	17.946	38.455
37	17.535	39.072
38	17.144	39.668
39	16.770	40.243
40	16.413	40.799

Table A.110 Dielectric Properties of Kidney from 40 GHz to 90 GHz

Frequency [GHz]	Permittivity	Conductivity [S/m]
40	16.413	40.799
50	13.578	45.463
60	11.676	48.936
70	10.337	51.629
80	9.356	53.792
90	8.614	55.579

Table A.111 Dielectric Properties of Lens from 1 GHz to 5 GHz

Frequency [GHz]	Permittivity	Conductivity [S/m]
1	46.399	0.824
2	45.126	1.249
3	44.013	1.866
4	42.867	2.646
5	41.671	3.561

Table A.112 Dielectric Properties of Lens from 5 GHz to 20 GHz

Frequency [GHz]	Permittivity	Conductivity [S/m]
5	41.671	3.561
6	40.437	4.581
7	39.180	5.682
8	37.915	6.842
9	36.657	8.042
10	35.415	9.264
11	34.199	10.496
12	33.017	11.726
13	31.871	12.946
14	30.767	14.147
15	29.707	15.325
16	28.690	16.475
17	27.719	17.594
18	26.791	18.681
19	25.908	19.733
20	25.067	20.751

Table A.113 Dielectric Properties of Lens from 20 GHz to 30 GHz

Frequency [GHz]	Permittivity	Conductivity [S/m]
20	25.067	20.751
21	24.267	21.734
22	23.507	22.681
23	22.784	23.595
24	22.098	24.475
25	21.446	25.322
26	20.827	26.137
27	20.239	26.921
28	19.680	27.676
29	19.149	28.402
30	18.644	29.101

Table A.114 Dielectric Properties of Lens from 30 GHz to 40 GHz

Frequency [GHz]	Permittivity	Conductivity [S/m]
30	18.644	29.101
31	18.164	29.774
32	17.707	30.422
33	17.272	31.046
34	16.858	31.648
35	16.463	32.227
36	16.087	32.786
37	15.728	33.324
38	15.386	33.844
39	15.059	34.346
40	14.746	34.831

Table A.115 Dielectric Properties of Lens from 40 GHz to 90 GHz

Frequency [GHz]	Permittivity	Conductivity [S/m]
40	14.746	34.831
50	12.268	38.892
60	10.606	41.903
70	9.437	44.229
80	8.583	46.090
90	7.938	47.621

Table A.116 Dielectric Properties of Liver from 1 GHz to 5 GHz

Frequency [GHz]	Permittivity	Conductivity [S/m]
1	46.401	0.897
2	43.822	1.404
3	42.165	2.076
4	40.689	2.893
5	39.260	3.828

Table A.117 Dielectric Properties of Liver from 5 GHz to 20 GHz

Frequency [GHz]	Permittivity	Conductivity [S/m]
5	39.260	3.828
6	37.849	4.853
7	36.456	5.942
8	35.086	7.073
9	33.748	8.228
10	32.450	9.391
11	31.198	10.549
12	29.995	11.694
13	28.846	12.816
14	27.750	13.912
15	26.708	14.976
16	25.719	16.007
17	24.783	17.001
18	23.898	17.960
19	23.061	18.882
20	22.270	19.767

Table A.118 Dielectric Properties of Liver from 20 GHz to 30 GHz

Frequency [GHz]	Permittivity	Conductivity [S/m]
20	22.270	19.767
21	21.524	20.617
22	20.819	21.432
23	20.154	22.213
24	19.526	22.962
25	18.933	23.679
26	18.372	24.367
27	17.843	25.026
28	17.342	25.658
29	16.868	26.263
30	16.419	26.845

Table A.119 Dielectric Properties of Liver from 30 GHz to 40 GHz

Frequency [GHz]	Permittivity	Conductivity [S/m]
30	16.419	26.845
31	15.994	27.403
32	15.591	27.938
33	15.209	28.453
34	14.846	28.948
35	14.501	29.423
36	14.174	29.881
37	13.862	30.322
38	13.566	30.746
39	13.283	31.155
40	13.014	31.550

Table A.120 Dielectric Properties of Liver from 40 GHz to 90 GHz

Frequency [GHz]	Permittivity	Conductivity [S/m]
40	13.014	31.550
50	10.900	34.840
60	9.503	37.267
70	8.528	39.143
80	7.820	40.647
90	7.286	41.890

Table A.121 Dielectric Properties of Lung Deflated from 1 GHz to 5 GHz

Frequency [GHz]	Permittivity	Conductivity [S/m]
1	51.102	0.897
2	49.059	1.395
3	47.604	2.085
4	46.232	2.943
5	44.859	3.941

Table A.122 Dielectric Properties of Lung Deflated from 5 GHz to 20 GHz

Frequency [GHz]	Permittivity	Conductivity [S/m]
5	44.859	3.941
6	43.472	5.050
7	42.077	6.244
8	40.685	7.499
9	39.306	8.796
10	37.951	10.116
11	36.628	11.445
12	35.343	12.772
13	34.101	14.087
14	32.905	15.382
15	31.757	16.652
16	30.658	17.891
17	29.607	19.097
18	28.606	20.268
19	27.651	21.402
20	26.743	22.498

Table A.123 Dielectric Properties of Lung Deflated from 20 GHz to 30 GHz

Frequency [GHz]	Permittivity	Conductivity [S/m]
20	26.743	22.498
21	25.880	23.556
22	25.060	24.577
23	24.280	25.561
24	23.540	26.509
25	22.837	27.422
26	22.169	28.300
27	21.535	29.145
28	20.933	29.958
29	20.360	30.741
30	19.816	31.494

Table A.124 Dielectric Properties of Lung Deflated from 30 GHz to 40 GHz

Frequency [GHz]	Permittivity	Conductivity [S/m]
30	19.816	31.494
31	19.298	32.220
32	18.806	32.918
33	18.337	33.591
34	17.891	34.239
35	17.465	34.863
36	17.060	35.466
37	16.673	36.047
38	16.304	36.607
39	15.951	37.149
40	15.615	37.671

Table A.125 Dielectric Properties of Lung Deflated from 40 GHz to 90 GHz

Frequency [GHz]	Permittivity	Conductivity [S/m]
40	15.615	37.671
50	12.943	42.054
60	11.151	45.307
70	9.891	47.823
80	8.969	49.837
90	8.273	51.496

Table A.126 Dielectric Properties of Lung Inflated from 1 GHz to 5 GHz

Frequency [GHz]	Permittivity	Conductivity [S/m]
1	21.825	0.474
2	20.791	0.685
3	20.130	0.969
4	19.541	1.318
5	18.966	1.722

Table A.127 Dielectric Properties of Lung Inflated from 5 GHz to 20 GHz

Frequency [GHz]	Permittivity	Conductivity [S/m]
5	18.966	1.722
6	18.394	2.170
7	17.823	2.650
8	17.256	3.156
9	16.697	3.677
10	16.149	4.207
11	15.614	4.741
12	15.096	5.274
13	14.595	5.802
14	14.113	6.322
15	13.651	6.832
16	13.209	7.329
17	12.786	7.813
18	12.384	8.283
19	12.000	8.738
20	11.635	9.177

Table A.128 Dielectric Properties of Lung Inflated from 20 GHz to 30 GHz

Frequency [GHz]	Permittivity	Conductivity [S/m]
20	11.635	9.177
21	11.288	9.602
22	10.959	10.012
23	10.646	10.406
24	10.349	10.787
25	10.066	11.153
26	9.798	11.505
27	9.544	11.844
28	9.302	12.171
29	9.072	12.485
30	8.853	12.787

Table A.129 Dielectric Properties of Lung Inflated from 30 GHz to 40 GHz

Frequency [GHz]	Permittivity	Conductivity [S/m]
30	8.853	12.787
31	8.646	13.078
32	8.448	13.358
33	8.260	13.628
34	8.081	13.888
35	7.910	14.139
36	7.747	14.381
37	7.592	14.614
38	7.444	14.839
39	7.302	15.056
40	7.167	15.266

Table A.130 Dielectric Properties of Lung Inflated from 40 GHz to 90 GHz

Frequency [GHz]	Permittivity	Conductivity [S/m]
40	7.167	15.266
50	6.095	17.026
60	5.376	18.332
70	4.870	19.344
80	4.500	20.154
90	4.220	20.821

Table A.131 Dielectric Properties of Lymph from 1 GHz to 5 GHz

Frequency [GHz]	Permittivity	Conductivity [S/m]
1	59.470	1.079
2	57.850	1.633
3	56.403	2.441
4	54.906	3.464
5	53.342	4.661

Table A.132 Dielectric Properties of Lymph from 5 GHz to 20 GHz

Frequency [GHz]	Permittivity	Conductivity [S/m]
5	53.342	4.661
6	51.726	5.998
7	50.080	7.440
8	48.424	8.960
9	46.776	10.531
10	45.150	12.132
11	43.558	13.746
12	42.008	15.357
13	40.509	16.954
14	39.063	18.527
15	37.673	20.070
16	36.342	21.576
17	35.070	23.043
18	33.855	24.466
19	32.698	25.844
20	31.597	27.177

Table A.133 Dielectric Properties of Lymph from 20 GHz to 30 GHz

Frequency [GHz]	Permittivity	Conductivity [S/m]
20	31.597	27.177
21	30.549	28.464
22	29.553	29.706
23	28.607	30.902
24	27.708	32.054
25	26.855	33.164
26	26.044	34.232
27	25.273	35.259
28	24.542	36.248
29	23.846	37.199
30	23.185	38.115

Table A.134 Dielectric Properties of Lymph from 30 GHz to 40 GHz

Frequency [GHz]	Permittivity	Conductivity [S/m]
30	23.185	38.115
31	22.556	38.996
32	21.957	39.845
33	21.388	40.662
34	20.845	41.450
35	20.328	42.209
36	19.835	42.941
37	19.365	43.646
38	18.917	44.328
39	18.488	44.985
40	18.079	45.620

Table A.135 Dielectric Properties of Lymph from 40 GHz to 90 GHz

Frequency [GHz]	Permittivity	Conductivity [S/m]
40	18.079	45.620
50	14.833	50.940
60	12.656	54.885
70	11.125	57.933
80	10.006	60.370
90	9.161	62.377

Table A.136 Dielectric Properties of Mucous Membrane from 1 GHz to 5 GHz

Frequency [GHz]	Permittivity	Conductivity [S/m]
1	45.711	0.882
2	43.520	1.336
3	42.112	1.947
4	40.847	2.702
5	39.611	3.574

Table A.137 Dielectric Properties of Mucous Membrane from 5 GHz to 20 GHz

Frequency [GHz]	Permittivity	Conductivity [S/m]
5	39.611	3.574
6	38.378	4.542
7	37.146	5.582
8	35.922	6.675
9	34.714	7.803
10	33.528	8.951
11	32.373	10.107
12	31.252	11.260
13	30.169	12.403
14	29.127	13.528
15	28.127	14.631
16	27.170	15.707
17	26.256	16.755
18	25.384	17.772
19	24.554	18.756
20	23.765	19.708

Table A.138 Dielectric Properties of Mucous Membrane from 20 GHz to 30 GHz

Frequency [GHz]	Permittivity	Conductivity [S/m]
20	23.765	19.708
21	23.014	20.628
22	22.301	21.514
23	21.623	22.369
24	20.980	23.192
25	20.369	23.984
26	19.788	24.747
27	19.237	25.481
28	18.714	26.187
29	18.216	26.867
30	17.743	27.521

Table A.139 Dielectric Properties of Mucous Membrane from 30 GHz to 40 GHz

Frequency [GHz]	Permittivity	Conductivity [S/m]
30	17.743	27.521
31	17.294	28.151
32	16.866	28.757
33	16.458	29.342
34	16.071	29.904
35	15.701	30.447
36	15.349	30.970
37	15.013	31.475
38	14.692	31.962
39	14.386	32.432
40	14.093	32.886

Table A.140 Dielectric Properties of Mucous Membrane from 40 GHz to 90 GHz

Frequency [GHz]	Permittivity	Conductivity [S/m]
40	14.093	32.886
50	11.773	36.693
60	10.216	39.519
70	9.121	41.706
80	8.321	43.457
90	7.715	44.900

Table A.141 Dielectric Properties of Nail from 1 GHz to 5 GHz

Frequency [GHz]	Permittivity	Conductivity [S/m]
1	12.363	0.156
2	11.654	0.310
3	11.066	0.506
4	10.532	0.728
5	10.040	0.962

Table A.142 Dielectric Properties of Nail from 5 GHz to 20 GHz

Frequency [GHz]	Permittivity	Conductivity [S/m]
5	10.040	0.962
6	9.587	1.203
7	9.171	1.443
8	8.790	1.680
9	8.440	1.912
10	8.120	2.136
11	7.826	2.352
12	7.556	2.561
13	7.308	2.760
14	7.080	2.952
15	6.870	3.136
16	6.676	3.311
17	6.496	3.480
18	6.329	3.641
19	6.174	3.796
20	6.030	3.944

Table A.143 Dielectric Properties of Nail from 20 GHz to 30 GHz

Frequency [GHz]	Permittivity	Conductivity [S/m]
20	6.030	3.944
21	5.896	4.087
22	5.771	4.223
23	5.653	4.355
24	5.544	4.481
25	5.441	4.603
26	5.344	4.720
27	5.253	4.834
28	5.167	4.943
29	5.086	5.048
30	5.010	5.150

Table A.144 Dielectric Properties of Nail from 30 GHz to 40 GHz

Frequency [GHz]	Permittivity	Conductivity [S/m]
30	5.010	5.150
31	4.937	5.249
32	4.869	5.344
33	4.804	5.437
34	4.742	5.527
35	4.684	5.614
36	4.628	5.698
37	4.575	5.780
38	4.524	5.860
39	4.476	5.938
40	4.430	6.014

Table A.145 Dielectric Properties of Nail from 40 GHz to 90 GHz

Frequency [GHz]	Permittivity	Conductivity [S/m]
40	4.430	6.014
50	4.062	6.674
60	3.810	7.206
70	3.628	7.649
80	3.491	8.029
90	3.384	8.360

Table A.146 Dielectric Properties of Nerve from 1 GHz to 5 GHz

Frequency [GHz]	Permittivity	Conductivity [S/m]
1	32.252	0.600
2	30.627	0.914
3	29.620	1.330
4	28.739	1.839
5	27.890	2.426

Table A.147 Dielectric Properties of Nerve from 5 GHz to 20 GHz

Frequency [GHz]	Permittivity	Conductivity [S/m]
5	27.890	2.426
6	27.050	3.076
7	26.216	3.773
8	25.389	4.506
9	24.575	5.261
10	23.778	6.030
11	23.002	6.803
12	22.249	7.575
13	21.523	8.339
14	20.824	9.092
15	20.154	9.829
16	19.513	10.549
17	18.901	11.250
18	18.317	11.930
19	17.762	12.588
20	17.233	13.225

Table A.148 Dielectric Properties of Nerve from 20 GHz to 30 GHz

Frequency [GHz]	Permittivity	Conductivity [S/m]
20	17.233	13.225
21	16.731	13.839
22	16.253	14.432
23	15.800	15.004
24	15.370	15.554
25	14.961	16.084
26	14.573	16.594
27	14.204	17.085
28	13.854	17.557
29	13.521	18.012
30	13.205	18.449

Table A.149 Dielectric Properties of Nerve from 30 GHz to 40 GHz

Frequency [GHz]	Permittivity	Conductivity [S/m]
30	13.205	18.449
31	12.904	18.871
32	12.618	19.276
33	12.345	19.667
34	12.086	20.044
35	11.839	20.407
36	11.603	20.757
37	11.378	21.094
38	11.164	21.420
39	10.959	21.735
40	10.763	22.039

Table A.150 Dielectric Properties of Nerve from 40 GHz to 90 GHz

Frequency [GHz]	Permittivity	Conductivity [S/m]
40	10.763	22.039
50	9.211	24.587
60	8.170	26.481
70	7.437	27.947
80	6.901	29.121
90	6.496	30.090

Table A.151 Dielectric Properties of Oesophagus from 1 GHz to 5 GHz

Frequency [GHz]	Permittivity	Conductivity [S/m]
1	64.797	1.232
2	62.892	1.844
3	61.268	2.729
4	59.611	3.848
5	57.890	5.157

Table A.152 Dielectric Properties of Oesophagus from 5 GHz to 20 GHz

Frequency [GHz]	Permittivity	Conductivity [S/m]
5	57.890	5.157
6	56.118	6.617
7	54.315	8.192
8	52.503	9.851
9	50.700	11.566
10	48.923	13.314
11	47.184	15.075
12	45.491	16.834
13	43.853	18.577
14	42.274	20.295
15	40.757	21.978
16	39.304	23.623
17	37.914	25.223
18	36.588	26.776
19	35.325	28.280
20	34.123	29.735

Table A.153 Dielectric Properties of Oesophagus from 20 GHz to 30 GHz

Frequency [GHz]	Permittivity	Conductivity [S/m]
20	34.123	29.735
21	32.979	31.140
22	31.892	32.495
23	30.859	33.800
24	29.878	35.058
25	28.946	36.269
26	28.061	37.434
27	27.220	38.555
28	26.421	39.634
29	25.662	40.673
30	24.940	41.672

Table A.154 Dielectric Properties of Oesophagus from 30 GHz to 40 GHz

Frequency [GHz]	Permittivity	Conductivity [S/m]
30	24.940	41.672
31	24.254	42.634
32	23.601	43.560
33	22.979	44.452
34	22.387	45.312
35	21.823	46.140
36	21.285	46.939
37	20.772	47.709
38	20.282	48.453
39	19.815	49.170
40	19.368	49.863

Table A.155 Dielectric Properties of Oesophagus from 40 GHz to 90 GHz

Frequency [GHz]	Permittivity	Conductivity [S/m]
40	19.368	49.863
50	15.825	55.670
60	13.449	59.975
70	11.778	63.302
80	10.557	65.964
90	9.634	68.154

Table A.156 Dielectric Properties of Ovary from 1 GHz to 5 GHz

Frequency [GHz]	Permittivity	Conductivity [S/m]
1	49.783	1.345
2	45.823	1.949
3	43.520	2.685
4	41.648	3.537
5	39.961	4.480

Table A.157 Dielectric Properties of Ovary from 5 GHz to 20 GHz

Frequency [GHz]	Permittivity	Conductivity [S/m]
5	39.961	4.480
6	38.384	5.490
7	36.891	6.545
8	35.472	7.626
9	34.123	8.721
10	32.841	9.817
11	31.625	10.905
12	30.472	11.979
13	29.382	13.032
14	28.351	14.063
15	27.376	15.067
16	26.456	16.043
17	25.586	16.990
18	24.766	17.907
19	23.990	18.795
20	23.258	19.654

Table A.158 Dielectric Properties of Ovary from 20 GHz to 30 GHz

Frequency [GHz]	Permittivity	Conductivity [S/m]
20	23.258	19.654
21	22.566	20.484
22	21.912	21.285
23	21.293	22.059
24	20.708	22.807
25	20.154	23.529
26	19.628	24.226
27	19.130	24.900
28	18.657	25.551
29	18.208	26.180
30	17.782	26.788

Table A.159 Dielectric Properties of Ovary from 30 GHz to 40 GHz

Frequency [GHz]	Permittivity	Conductivity [S/m]
30	17.782	26.788
31	17.376	27.377
32	16.991	27.946
33	16.623	28.498
34	16.273	29.031
35	15.939	29.549
36	15.620	30.050
37	15.316	30.536
38	15.025	31.008
39	14.746	31.466
40	14.480	31.911

Table A.160 Dielectric Properties of Ovary from 40 GHz to 90 GHz

Frequency [GHz]	Permittivity	Conductivity [S/m]
40	14.480	31.911
50	12.346	35.746
60	10.882	38.742
70	9.828	41.170
80	9.039	43.195
90	8.429	44.923

Table A.161 Dielectric Properties of Pancreas from 1 GHz to 5 GHz

Frequency [GHz]	Permittivity	Conductivity [S/m]
1	59.470	1.079
2	57.850	1.633
3	56.403	2.441
4	54.906	3.464
5	53.342	4.661

Table A.162 Dielectric Properties of Pancreas from 5 GHz to 20 GHz

Frequency [GHz]	Permittivity	Conductivity [S/m]
5	53.342	4.661
6	51.726	5.998
7	50.080	7.440
8	48.424	8.960
9	46.776	10.531
10	45.150	12.132
11	43.558	13.746
12	42.008	15.357
13	40.509	16.954
14	39.063	18.527
15	37.673	20.070
16	36.342	21.576
17	35.070	23.043
18	33.855	24.466
19	32.698	25.844
20	31.597	27.177

Table A.163 Dielectric Properties of Pancreas from 20 GHz to 30 GHz

Frequency [GHz]	Permittivity	Conductivity [S/m]
20	31.597	27.177
21	30.549	28.464
22	29.553	29.706
23	28.607	30.902
24	27.708	32.054
25	26.855	33.164
26	26.044	34.232
27	25.273	35.259
28	24.542	36.248
29	23.846	37.199
30	23.185	38.115

Table A.164 Dielectric Properties of Pancreas from 30 GHz to 40 GHz

Frequency [GHz]	Permittivity	Conductivity [S/m]
30	23.185	38.115
31	22.556	38.996
32	21.957	39.845
33	21.388	40.662
34	20.845	41.450
35	20.328	42.209
36	19.835	42.941
37	19.365	43.646
38	18.917	44.328
39	18.488	44.985
40	18.079	45.620

Table A.165 Dielectric Properties of Pancreas from 40 GHz to 90 GHz

Frequency [GHz]	Permittivity	Conductivity [S/m]
40	18.079	45.620
50	14.833	50.940
60	12.656	54.885
70	11.125	57.933
80	10.006	60.370
90	9.161	62.377

Table A.166 Dielectric Properties of Prostate from 1 GHz to 5 GHz

Frequency [GHz]	Permittivity	Conductivity [S/m]
1	60.259	1.253
2	58.270	1.827
3	56.695	2.647
4	55.131	3.679
5	53.526	4.883

Table A.167 Dielectric Properties of Prostate from 5 GHz to 20 GHz

Frequency [GHz]	Permittivity	Conductivity [S/m]
5	53.526	4.883
6	51.882	6.226
7	50.216	7.673
8	48.544	9.197
9	46.884	10.772
10	45.248	12.377
11	43.648	13.994
12	42.092	15.608
13	40.586	17.208
14	39.135	18.784
15	37.742	20.329
16	36.407	21.838
17	35.131	23.306
18	33.913	24.732
19	32.753	26.112
20	31.649	27.447

Table A.168 Dielectric Properties of Prostate from 20 GHz to 30 GHz

Frequency [GHz]	Permittivity	Conductivity [S/m]
20	31.649	27.447
21	30.599	28.736
22	29.601	29.979
23	28.653	31.177
24	27.753	32.331
25	26.898	33.442
26	26.085	34.511
27	25.314	35.540
28	24.580	36.530
29	23.884	37.483
30	23.221	38.400

Table A.169 Dielectric Properties of Prostate from 30 GHz to 40 GHz

Frequency [GHz]	Permittivity	Conductivity [S/m]
30	23.221	38.400
31	22.591	39.283
32	21.992	40.133
33	21.421	40.951
34	20.878	41.740
35	20.360	42.500
36	19.866	43.233
37	19.396	43.940
38	18.946	44.622
39	18.517	45.280
40	18.107	45.916

Table A.170 Dielectric Properties of Prostate from 40 GHz to 90 GHz

Frequency [GHz]	Permittivity	Conductivity [S/m]
40	18.107	45.916
50	14.856	51.245
60	12.675	55.198
70	11.142	58.252
80	10.021	60.695
90	9.175	62.706

Table A.171 Dielectric Properties of Retina from 1 GHz to 5 GHz

Frequency [GHz]	Permittivity	Conductivity [S/m]
1	55.017	1.206
2	53.271	1.725
3	51.859	2.468
4	50.448	3.404
5	48.996	4.499

Table A.172 Dielectric Properties of Retina from 5 GHz to 20 GHz

Frequency [GHz]	Permittivity	Conductivity [S/m]
5	48.996	4.499
6	47.506	5.718
7	45.994	7.033
8	44.477	8.418
9	42.969	9.849
10	41.484	11.308
11	40.030	12.777
12	38.617	14.244
13	37.249	15.698
14	35.931	17.131
15	34.664	18.535
16	33.451	19.906
17	32.292	21.241
18	31.186	22.536
19	30.132	23.791
20	29.128	25.004

Table A.173 Dielectric Properties of Retina from 20 GHz to 30 GHz

Frequency [GHz]	Permittivity	Conductivity [S/m]
20	29.128	25.004
21	28.174	26.175
22	27.267	27.305
23	26.406	28.394
24	25.587	29.443
25	24.810	30.453
26	24.072	31.424
27	23.370	32.360
28	22.704	33.260
29	22.071	34.126
30	21.469	34.959

Table A.174 Dielectric Properties of Retina from 30 GHz to 40 GHz

Frequency [GHz]	Permittivity	Conductivity [S/m]
30	21.469	34.959
31	20.896	35.761
32	20.351	36.534
33	19.833	37.278
34	19.339	37.995
35	18.868	38.685
36	18.420	39.352
37	17.992	39.994
38	17.584	40.614
39	17.194	41.213
40	16.821	41.791

Table A.175 Dielectric Properties of Retina from 40 GHz to 90 GHz

Frequency [GHz]	Permittivity	Conductivity [S/m]
40	16.821	41.791
50	13.866	46.634
60	11.884	50.226
70	10.491	53.002
80	9.472	55.222
90	8.702	57.050

Table A.176 Dielectric Properties of Skin Wet from 1 GHz to 5 GHz

Frequency [GHz]	Permittivity	Conductivity [S/m]
1	45.711	0.882
2	43.520	1.336
3	42.112	1.947
4	40.847	2.702
5	39.611	3.574

Table A.177 Dielectric Properties of Skin Wet from 5 GHz to 20 GHz

Frequency [GHz]	Permittivity	Conductivity [S/m]
5	39.611	3.574
6	38.378	4.542
7	37.146	5.582
8	35.922	6.675
9	34.714	7.803
10	33.528	8.951
11	32.373	10.107
12	31.252	11.260
13	30.169	12.403
14	29.127	13.528
15	28.127	14.631
16	27.170	15.707
17	26.256	16.755
18	25.384	17.772
19	24.554	18.756
20	23.765	19.708

Table A.178 Dielectric Properties of Skin Wet from 20 GHz to 30 GHz

Frequency [GHz]	Permittivity	Conductivity [S/m]
20	23.765	19.708
21	23.014	20.628
22	22.301	21.514
23	21.623	22.369
24	20.980	23.192
25	20.369	23.984
26	19.788	24.747
27	19.237	25.481
28	18.714	26.187
29	18.216	26.867
30	17.743	27.521

Table A.179 Dielectric Properties of Skin Wet from 30 GHz to 40 GHz

Frequency [GHz]	Permittivity	Conductivity [S/m]
30	17.743	27.521
31	17.294	28.151
32	16.866	28.757
33	16.458	29.342
34	16.071	29.904
35	15.701	30.447
36	15.349	30.970
37	15.013	31.475
38	14.692	31.962
39	14.386	32.432
40	14.093	32.886

Table A.180 Dielectric Properties of Skin Wet from 40 GHz to 90 GHz

Frequency [GHz]	Permittivity	Conductivity [S/m]
40	14.093	32.886
50	11.773	36.693
60	10.216	39.519
70	9.121	41.706
80	8.321	43.457
90	7.715	44.900

Table A.181 Dielectric Properties of Small Intestine from 1 GHz to 5 GHz

Frequency [GHz]	Permittivity	Conductivity [S/m]
1	58.872	2.218
2	55.406	2.834
3	53.373	3.640
4	51.634	4.622
5	49.977	5.753

Table A.182 Dielectric Properties of Small Intestine from 5 GHz to 20 GHz

Frequency [GHz]	Permittivity	Conductivity [S/m]
5	49.977	5.753
6	48.347	7.004
7	46.733	8.347
8	45.137	9.756
9	43.567	11.208
10	42.030	12.687
11	40.535	14.174
12	39.086	15.658
13	37.687	17.128
14	36.342	18.575
15	35.053	19.993
16	33.819	21.378
17	32.641	22.724
18	31.519	24.032
19	30.450	25.298
20	29.433	26.522

Table A.183 Dielectric Properties of Small Intestine from 20 GHz to 30 GHz

Frequency [GHz]	Permittivity	Conductivity [S/m]
20	29.433	26.522
21	28.467	27.703
22	27.549	28.843
23	26.677	29.942
24	25.849	31.000
25	25.063	32.018
26	24.316	32.999
27	23.607	33.942
28	22.934	34.850
29	22.294	35.724
30	21.685	36.565

Table A.184 Dielectric Properties of Small Intestine from 30 GHz to 40 GHz

Frequency [GHz]	Permittivity	Conductivity [S/m]
30	21.685	36.565
31	21.107	37.375
32	20.557	38.154
33	20.033	38.905
34	19.534	39.629
35	19.059	40.326
36	18.606	40.999
37	18.174	41.648
38	17.761	42.274
39	17.367	42.879
40	16.991	43.463

Table A.185 Dielectric Properties of Small Intestine from 40 GHz to 90 GHz

Frequency [GHz]	Permittivity	Conductivity [S/m]
40	16.991	43.463
50	14.007	48.359
60	12.005	51.996
70	10.597	54.811
80	9.567	57.067
90	8.789	58.926

Table A.186 Dielectric Properties of Spinal Cord from 1 GHz to 5 GHz

Frequency [GHz]	Permittivity	Conductivity [S/m]
1	32.252	0.600
2	30.627	0.914
3	29.620	1.330
4	28.739	1.839
5	27.890	2.426

Table A.187 Dielectric Properties of Spinal Cord from 5 GHz to 20 GHz

Frequency [GHz]	Permittivity	Conductivity [S/m]
5	27.890	2.426
6	27.050	3.076
7	26.216	3.773
8	25.389	4.506
9	24.575	5.261
10	23.778	6.030
11	23.002	6.803
12	22.249	7.575
13	21.523	8.339
14	20.824	9.092
15	20.154	9.829
16	19.513	10.549
17	18.901	11.250
18	18.317	11.930
19	17.762	12.588
20	17.233	13.225

Table A.188 Dielectric Properties of Spinal Cord from 20 GHz to 30 GHz

Frequency [GHz]	Permittivity	Conductivity [S/m]
20	17.233	13.225
21	16.731	13.839
22	16.253	14.432
23	15.800	15.004
24	15.370	15.554
25	14.961	16.084
26	14.573	16.594
27	14.204	17.085
28	13.854	17.557
29	13.521	18.012
30	13.205	18.449

Table A.189 Dielectric Properties of Spinal Cord from 30 GHz to 40 GHz

Frequency [GHz]	Permittivity	Conductivity [S/m]
30	13.205	18.449
31	12.904	18.871
32	12.618	19.276
33	12.345	19.667
34	12.086	20.044
35	11.839	20.407
36	11.603	20.757
37	11.378	21.094
38	11.164	21.420
39	10.959	21.735
40	10.763	22.039

Table A.190 Dielectric Properties of Spinal Cord from 40 GHz to 90 GHz

Frequency [GHz]	Permittivity	Conductivity [S/m]
40	10.763	22.039
50	9.211	24.587
60	8.170	26.481
70	7.437	27.947
80	6.901	29.121
90	6.496	30.090

Table A.191 Dielectric Properties of Spleen from 1 GHz to 5 GHz

Frequency [GHz]	Permittivity	Conductivity [S/m]
1	56.611	1.323
2	53.378	1.912
3	51.447	2.686
4	49.784	3.630
5	48.195	4.718

Table A.192 Dielectric Properties of Spleen from 5 GHz to 20 GHz

Frequency [GHz]	Permittivity	Conductivity [S/m]
5	48.195	4.718
6	46.630	5.920
7	45.079	7.210
8	43.545	8.564
9	42.037	9.961
10	40.560	11.381
11	39.123	12.811
12	37.730	14.237
13	36.387	15.649
14	35.094	17.040
15	33.855	18.403
16	32.670	19.733
17	31.538	21.027
18	30.459	22.283
19	29.432	23.500
20	28.455	24.676

Table A.193 Dielectric Properties of Spleen from 20 GHz to 30 GHz

Frequency [GHz]	Permittivity	Conductivity [S/m]
20	28.455	24.676
21	27.527	25.812
22	26.645	26.907
23	25.807	27.963
24	25.011	28.980
25	24.256	29.959
26	23.539	30.901
27	22.857	31.808
28	22.210	32.680
29	21.595	33.520
30	21.011	34.329

Table A.194 Dielectric Properties of Spleen from 30 GHz to 40 GHz

Frequency [GHz]	Permittivity	Conductivity [S/m]
30	21.011	34.329
31	20.455	35.107
32	19.926	35.857
33	19.423	36.578
34	18.943	37.274
35	18.487	37.945
36	18.051	38.591
37	17.636	39.215
38	17.240	39.817
39	16.862	40.399
40	16.500	40.960

Table A.195 Dielectric Properties of Spleen from 40 GHz to 90 GHz

Frequency [GHz]	Permittivity	Conductivity [S/m]
40	16.500	40.960
50	13.632	45.669
60	11.708	49.168
70	10.354	51.878
80	9.364	54.049
90	8.615	55.840

Table A.196 Dielectric Properties of Stomach from 1 GHz to 5 GHz

Frequency [GHz]	Permittivity	Conductivity [S/m]
1	64.797	1.232
2	62.892	1.844
3	61.268	2.729
4	59.611	3.848
5	57.890	5.157

Table A.197 Dielectric Properties of Stomach from 5 GHz to 20 GHz

Frequency [GHz]	Permittivity	Conductivity [S/m]
5	57.890	5.157
6	56.118	6.617
7	54.315	8.192
8	52.503	9.851
9	50.700	11.566
10	48.923	13.314
11	47.184	15.075
12	45.491	16.834
13	43.853	18.577
14	42.274	20.295
15	40.757	21.978
16	39.304	23.623
17	37.914	25.223
18	36.588	26.776
19	35.325	28.280
20	34.123	29.735

Table A.198 Dielectric Properties of Stomach from 20 GHz to 30 GHz

Frequency [GHz]	Permittivity	Conductivity [S/m]
20	34.123	29.735
21	32.979	31.140
22	31.892	32.495
23	30.859	33.800
24	29.878	35.058
25	28.946	36.269
26	28.061	37.434
27	27.220	38.555
28	26.421	39.634
29	25.662	40.673
30	24.940	41.672

Table A.199 Dielectric Properties of Stomach from 30 GHz to 40 GHz

Frequency [GHz]	Permittivity	Conductivity [S/m]
30	24.940	41.672
31	24.254	42.634
32	23.601	43.560
33	22.979	44.452
34	22.387	45.312
35	21.823	46.140
36	21.285	46.939
37	20.772	47.709
38	20.282	48.453
39	19.815	49.170
40	19.368	49.863

Table A.200 Dielectric Properties of Stomach from 40 GHz to 90 GHz

Frequency [GHz]	Permittivity	Conductivity [S/m]
40	19.368	49.863
50	15.825	55.670
60	13.449	59.975
70	11.778	63.302
80	10.557	65.964
90	9.634	68.154

Table A.201 Dielectric Properties of Tendon from 1 GHz to 5 GHz

Frequency [GHz]	Permittivity	Conductivity [S/m]
1	45.634	0.760
2	43.908	1.339
3	42.125	2.166
4	40.237	3.174
5	38.299	4.301

Table A.202 Dielectric Properties of Tendon from 5 GHz to 20 GHz

Frequency [GHz]	Permittivity	Conductivity [S/m]
5	38.299	4.301
6	36.365	5.498
7	34.475	6.726
8	32.658	7.955
9	30.934	9.164
10	29.310	10.339
11	27.792	11.469
12	26.379	12.549
13	25.068	13.576
14	23.854	14.549
15	22.731	15.469
16	21.694	16.337
17	20.736	17.156
18	19.851	17.928
19	19.032	18.656
20	18.274	19.342

Table A.203 Dielectric Properties of Tendon from 20 GHz to 30 GHz

Frequency [GHz]	Permittivity	Conductivity [S/m]
20	18.274	19.342
21	17.573	19.989
22	16.922	20.599
23	16.318	21.176
24	15.757	21.722
25	15.235	22.239
26	14.748	22.728
27	14.294	23.192
28	13.870	23.633
29	13.473	24.052
30	13.102	24.451

Table A.204 Dielectric Properties of Tendon from 30 GHz to 40 GHz

Frequency [GHz]	Permittivity	Conductivity [S/m]
30	13.102	24.451
31	12.753	24.831
32	12.426	25.193
33	12.118	25.539
34	11.829	25.870
35	11.556	26.186
36	11.298	26.489
37	11.055	26.779
38	10.825	27.058
39	10.608	27.325
40	10.401	27.583

Table A.205 Dielectric Properties of Tendon from 40 GHz to 90 GHz

Frequency [GHz]	Permittivity	Conductivity [S/m]
40	10.401	27.583
50	8.822	29.701
60	7.813	31.248
70	7.125	32.444
80	6.631	33.407
90	6.263	34.208

Table A.206 Dielectric Properties of Testis from 1 GHz to 5 GHz

Frequency [GHz]	Permittivity	Conductivity [S/m]
1	60.259	1.253
2	58.270	1.827
3	56.695	2.647
4	55.131	3.679
5	53.526	4.883

Table A.207 Dielectric Properties of Testis from 5 GHz to 20 GHz

Frequency [GHz]	Permittivity	Conductivity [S/m]
5	53.526	4.883
6	51.882	6.226
7	50.216	7.673
8	48.544	9.197
9	46.884	10.772
10	45.248	12.377
11	43.648	13.994
12	42.092	15.608
13	40.586	17.208
14	39.135	18.784
15	37.742	20.329
16	36.407	21.838
17	35.131	23.306
18	33.913	24.732
19	32.753	26.112
20	31.649	27.447

Table A.208 Dielectric Properties of Testis from 20 GHz to 30 GHz

Frequency [GHz]	Permittivity	Conductivity [S/m]
20	31.649	27.447
21	30.599	28.736
22	29.601	29.979
23	28.653	31.177
24	27.753	32.331
25	26.898	33.442
26	26.085	34.511
27	25.314	35.540
28	24.580	36.530
29	23.884	37.483
30	23.221	38.400

Table A.209 Dielectric Properties of Testis from 30 GHz to 40 GHz

Frequency [GHz]	Permittivity	Conductivity [S/m]
30	23.221	38.400
31	22.591	39.283
32	21.992	40.133
33	21.421	40.951
34	20.878	41.740
35	20.360	42.500
36	19.866	43.233
37	19.396	43.940
38	18.946	44.622
39	18.517	45.280
40	18.107	45.916

Table A.210 Dielectric Properties of Testis from 40 GHz to 90 GHz

Frequency [GHz]	Permittivity	Conductivity [S/m]
40	18.107	45.916
50	14.856	51.245
60	12.675	55.198
70	11.142	58.252
80	10.021	60.695
90	9.175	62.706

Table A.211 Dielectric Properties of Thymus from 1 GHz to 5 GHz

Frequency [GHz]	Permittivity	Conductivity [S/m]
1	59.470	1.079
2	57.850	1.633
3	56.403	2.441
4	54.906	3.464
5	53.342	4.661

Table A.212 Dielectric Properties of Thymus from 5 GHz to 20 GHz

Frequency [GHz]	Permittivity	Conductivity [S/m]
5	53.342	4.661
6	51.726	5.998
7	50.080	7.440
8	48.424	8.960
9	46.776	10.531
10	45.150	12.132
11	43.558	13.746
12	42.008	15.357
13	40.509	16.954
14	39.063	18.527
15	37.673	20.070
16	36.342	21.576
17	35.070	23.043
18	33.855	24.466
19	32.698	25.844
20	31.597	27.177

Table A.213 Dielectric Properties of Thymus from 20 GHz to 30 GHz

Frequency [GHz]	Permittivity	Conductivity [S/m]
20	31.597	27.177
21	30.549	28.464
22	29.553	29.706
23	28.607	30.902
24	27.708	32.054
25	26.855	33.164
26	26.044	34.232
27	25.273	35.259
28	24.542	36.248
29	23.846	37.199
30	23.185	38.115

Table A.214 Dielectric Properties of Thymus from 30 GHz to 40 GHz

Frequency [GHz]	Permittivity	Conductivity [S/m]
30	23.185	38.115
31	22.556	38.996
32	21.957	39.845
33	21.388	40.662
34	20.845	41.450
35	20.328	42.209
36	19.835	42.941
37	19.365	43.646
38	18.917	44.328
39	18.488	44.985
40	18.079	45.620

Table A.215 Dielectric Properties of Thymus from 40 GHz to 90 GHz

Frequency [GHz]	Permittivity	Conductivity [S/m]
40	18.079	45.620
50	14.833	50.940
60	12.656	54.885
70	11.125	57.933
80	10.006	60.370
90	9.161	62.377

Table A.216 Dielectric Properties of Thyroid from 1 GHz to 5 GHz

Frequency [GHz]	Permittivity	Conductivity [S/m]
1	59.470	1.079
2	57.850	1.633
3	56.403	2.441
4	54.906	3.464
5	53.342	4.661

Table A.217 Dielectric Properties of Thyroid from 5 GHz to 20 GHz

Frequency [GHz]	Permittivity	Conductivity [S/m]
5	53.342	4.661
6	51.726	5.998
7	50.080	7.440
8	48.424	8.960
9	46.776	10.531
10	45.150	12.132
11	43.558	13.746
12	42.008	15.357
13	40.509	16.954
14	39.063	18.527
15	37.673	20.070
16	36.342	21.576
17	35.070	23.043
18	33.855	24.466
19	32.698	25.844
20	31.597	27.177

Table A.218 Dielectric Properties of Thyroid from 20 GHz to 30 GHz

Frequency [GHz]	Permittivity	Conductivity [S/m]
20	31.597	27.177
21	30.549	28.464
22	29.553	29.706
23	28.607	30.902
24	27.708	32.054
25	26.855	33.164
26	26.044	34.232
27	25.273	35.259
28	24.542	36.248
29	23.846	37.199
30	23.185	38.115

Table A.219 Dielectric Properties of Thyroid from 30 GHz to 40 GHz

Frequency [GHz]	Permittivity	Conductivity [S/m]
30	23.185	38.115
31	22.556	38.996
32	21.957	39.845
33	21.388	40.662
34	20.845	41.450
35	20.328	42.209
36	19.835	42.941
37	19.365	43.646
38	18.917	44.328
39	18.488	44.985
40	18.079	45.620

Table A.220 Dielectric Properties of Thyroid from 40 GHz to 90 GHz

Frequency [GHz]	Permittivity	Conductivity [S/m]
40	18.079	45.620
50	14.833	50.940
60	12.656	54.885
70	11.125	57.933
80	10.006	60.370
90	9.161	62.377

Table A.221 Dielectric Properties of Tongue from 1 GHz to 5 GHz

Frequency [GHz]	Permittivity	Conductivity [S/m]
1	55.017	0.975
2	53.271	1.494
3	51.859	2.238
4	50.448	3.174
5	48.996	4.268

Table A.222 Dielectric Properties of Tongue from 5 GHz to 20 GHz

Frequency [GHz]	Permittivity	Conductivity [S/m]
5	48.996	4.268
6	47.506	5.488
7	45.994	6.803
8	44.477	8.187
9	42.969	9.619
10	41.484	11.077
11	40.030	12.546
12	38.617	14.014
13	37.249	15.468
14	35.931	16.900
15	34.664	18.304
16	33.451	19.676
17	32.292	21.010
18	31.186	22.306
19	30.132	23.560
20	29.128	24.773

Table A.223 Dielectric Properties of Tongue from 20 GHz to 30 GHz

Frequency [GHz]	Permittivity	Conductivity [S/m]
20	29.128	24.773
21	28.174	25.945
22	27.267	27.075
23	26.406	28.164
24	25.587	29.212
25	24.810	30.222
26	24.072	31.194
27	23.370	32.129
28	22.704	33.029
29	22.071	33.895
30	21.469	34.728

Table A.224 Dielectric Properties of Tongue from 30 GHz to 40 GHz

Frequency [GHz]	Permittivity	Conductivity [S/m]
30	21.469	34.728
31	20.896	35.531
32	20.351	36.303
33	19.833	37.047
34	19.339	37.764
35	18.868	38.455
36	18.420	39.121
37	17.992	39.763
38	17.584	40.383
39	17.194	40.982
40	16.821	41.560

Table A.225 Dielectric Properties of Tongue from 40 GHz to 90 GHz

Frequency [GHz]	Permittivity	Conductivity [S/m]
40	16.821	41.560
50	13.866	46.403
60	11.884	49.995
70	10.491	52.771
80	9.472	54.992
90	8.702	56.819

Table A.226 Dielectric Properties of Tooth from 1 GHz to 5 GHz

Frequency [GHz]	Permittivity	Conductivity [S/m]
1	12.363	0.156
2	11.654	0.310
3	11.066	0.506
4	10.532	0.728
5	10.040	0.962

Table A.227 Dielectric Properties of Tooth from 5 GHz to 20 GHz

Frequency [GHz]	Permittivity	Conductivity [S/m]
5	10.040	0.962
6	9.587	1.203
7	9.171	1.443
8	8.790	1.680
9	8.440	1.912
10	8.120	2.136
11	7.826	2.352
12	7.556	2.561
13	7.308	2.760
14	7.080	2.952
15	6.870	3.136
16	6.676	3.311
17	6.496	3.480
18	6.329	3.641
19	6.174	3.796
20	6.030	3.944

Table A.228 Dielectric Properties of Tooth from 20 GHz to 30 GHz

Frequency [GHz]	Permittivity	Conductivity [S/m]
20	6.030	3.944
21	5.896	4.087
22	5.771	4.223
23	5.653	4.355
24	5.544	4.481
25	5.441	4.603
26	5.344	4.720
27	5.253	4.834
28	5.167	4.943
29	5.086	5.048
30	5.010	5.150

Table A.229 Dielectric Properties of Tooth from 30 GHz to 40 GHz

Frequency [GHz]	Permittivity	Conductivity [S/m]
30	5.010	5.150
31	4.937	5.249
32	4.869	5.344
33	4.804	5.437
34	4.742	5.527
35	4.684	5.614
36	4.628	5.698
37	4.575	5.780
38	4.524	5.860
39	4.476	5.938
40	4.430	6.014

Table A.230 Dielectric Properties of Tooth from 40 GHz to 90 GHz

Frequency [GHz]	Permittivity	Conductivity [S/m]
40	4.430	6.014
50	4.062	6.674
60	3.810	7.206
70	3.628	7.649
80	3.491	8.029
90	3.384	8.360

Table A.231 Dielectric Properties of Trachea from 1 GHz to 5 GHz

Frequency [GHz]	Permittivity	Conductivity [S/m]
1	41.779	0.802
2	40.262	1.210
3	39.113	1.784
4	37.997	2.503
5	36.864	3.340

Table A.232 Dielectric Properties of Trachea from 5 GHz to 20 GHz

Frequency [GHz]	Permittivity	Conductivity [S/m]
5	36.864	3.340
6	35.712	4.273
7	34.548	5.277
8	33.383	6.333
9	32.227	7.425
10	31.090	8.537
11	29.979	9.657
12	28.899	10.775
13	27.854	11.883
14	26.848	12.974
15	25.881	14.044
16	24.956	15.089
17	24.072	16.106
18	23.228	17.092
19	22.424	18.048
20	21.659	18.972

Table A.233 Dielectric Properties of Trachea from 20 GHz to 30 GHz

Frequency [GHz]	Permittivity	Conductivity [S/m]
20	21.659	18.972
21	20.932	19.865
22	20.241	20.725
23	19.584	21.555
24	18.961	22.354
25	18.368	23.123
26	17.806	23.863
27	17.271	24.576
28	16.764	25.261
29	16.281	25.921
30	15.822	26.556

Table A.234 Dielectric Properties of Trachea from 30 GHz to 40 GHz

Frequency [GHz]	Permittivity	Conductivity [S/m]
30	15.822	26.556
31	15.386	27.167
32	14.971	27.756
33	14.576	28.323
34	14.200	28.869
35	13.841	29.395
36	13.499	29.903
37	13.173	30.393
38	12.862	30.865
39	12.565	31.321
40	12.281	31.762

Table A.235 Dielectric Properties of Trachea from 40 GHz to 90 GHz

Frequency [GHz]	Permittivity	Conductivity [S/m]
40	12.281	31.762
50	10.030	35.454
60	8.520	38.194
70	7.458	40.313
80	6.681	42.008
90	6.094	43.404

Table A.236 Dielectric Properties of Uterus from 1 GHz to 5 GHz

Frequency [GHz]	Permittivity	Conductivity [S/m]
1	60.777	1.315
2	58.577	1.902
3	56.921	2.731
4	55.314	3.769
5	53.681	4.979

Table A.237 Dielectric Properties of Uterus from 5 GHz to 20 GHz

Frequency [GHz]	Permittivity	Conductivity [S/m]
5	53.681	4.979
6	52.018	6.326
7	50.337	7.778
8	48.654	9.306
9	46.985	10.884
10	45.341	12.492
11	43.735	14.112
12	42.173	15.730
13	40.663	17.332
14	39.208	18.911
15	37.811	20.458
16	36.472	21.969
17	35.194	23.440
18	33.974	24.867
19	32.811	26.249
20	31.705	27.586

Table A.238 Dielectric Properties of Uterus from 20 GHz to 30 GHz

Frequency [GHz]	Permittivity	Conductivity [S/m]
20	31.705	27.586
21	30.653	28.877
22	29.653	30.122
23	28.704	31.322
24	27.802	32.477
25	26.945	33.590
26	26.131	34.661
27	25.358	35.691
28	24.624	36.683
29	23.926	37.637
30	23.262	38.555

Table A.239 Dielectric Properties of Uterus from 30 GHz to 40 GHz

Frequency [GHz]	Permittivity	Conductivity [S/m]
30	23.262	38.555
31	22.631	39.439
32	22.031	40.291
33	21.460	41.110
34	20.915	41.900
35	20.397	42.662
36	19.902	43.396
37	19.431	44.104
38	18.981	44.787
39	18.551	45.447
40	18.141	46.084

Table A.240 Dielectric Properties of Uterus from 40 GHz to 90 GHz

Frequency [GHz]	Permittivity	Conductivity [S/m]
40	18.141	46.084
50	14.884	51.423
60	12.700	55.384
70	11.164	58.447
80	10.041	60.897
90	9.193	62.915

Table A.241 Dielectric Properties of Vitreous Humor from 1 GHz to 5 GHz

Frequency [GHz]	Permittivity	Conductivity [S/m]
1	68.875	1.667
2	68.472	2.156
3	67.817	2.956
4	66.923	4.049
5	65.810	5.411

Table A.242 Dielectric Properties of Vitreous Humor from 5 GHz to 20 GHz

Frequency [GHz]	Permittivity	Conductivity [S/m]
5	65.810	5.411
6	64.502	7.011
7	63.026	8.817
8	61.411	10.795
9	59.683	12.909
10	57.872	15.126
11	56.002	17.414
12	54.098	19.745
13	52.180	22.093
14	50.267	24.434
15	48.374	26.750
16	46.516	29.025
17	44.701	31.246
18	42.938	33.404
19	41.233	35.491
20	39.590	37.501

Table A.243 Dielectric Properties of Vitreous Humor from 20 GHz to 30 GHz

Frequency [GHz]	Permittivity	Conductivity [S/m]
20	39.590	37.501
21	38.013	39.432
22	36.502	41.281
23	35.058	43.048
24	33.681	44.733
25	32.370	46.338
26	31.123	47.865
27	29.938	49.315
28	28.813	50.692
29	27.745	51.999
30	26.733	53.238

Table A.244 Dielectric Properties of Vitreous Humor from 30 GHz to 40 GHz

Frequency [GHz]	Permittivity	Conductivity [S/m]
30	26.733	53.238
31	25.773	54.412
32	24.864	55.525
33	24.002	56.581
34	23.184	57.581
35	22.410	58.529
36	21.676	59.427
37	20.979	60.280
38	20.319	61.088
39	19.692	61.855
40	19.097	62.583

Table A.245 Dielectric Properties of Vitreous Humor from 40 GHz to 90 GHz

Frequency [GHz]	Permittivity	Conductivity [S/m]
40	19.097	62.583
50	14.544	68.156
60	11.704	71.632
70	9.844	73.909
80	8.571	75.467
90	7.665	76.575

APPENDIX B

THESIS MODEL CODE

B.1 MATLAB Code for MRI Image Processing

Listing B.1: Human wrist 3D model for MRI image processing applications.

```
clear;clc;close all;
% resolution 2 mm
nx = 320;
ny = 160;
nz = 866;
fname='male-v1.raw';
fid = fopen(fname,'rb');
body_data=fread(fid,inf, 'uint8');
fclose(fid);
irec = 0;
for iz = 1:nz
    for iy = 1:ny
        for ix = 1:nx
            irec = irec+1;
            body(ix,iy,iz) = body_data(irec);
        end
    end
end

wrist=zeros(40,50,60);
wrist(1:40,1:50,1:60)=body(24:63,50:99,424:-1:365);

ax=40;
ay=50;
az=60;

for ii=1:ax
    for jj=1:ay
        for kk=1:az
            if wrist(ii,jj,kk)==51 %skin
                wrist(ii,jj,kk)=7;
            end
        end
    end
end

for ii=1:ax
    for jj=1:ay
        for kk=1:az
            if wrist(ii,jj,kk)==48 %fat
                wrist(ii,jj,kk)=2;
            end
        end
    end
end

for ii=1:ax
```

```
    for jj=1:ay
        for kk=1:az
            if wrist(ii,jj,kk)==45 %cortical bone
                wrist(ii,jj,kk)=5;
            end
        end
    end
end

for ii=1:ax
    for jj=1:ay
        for kk=1:az
            if wrist(ii,jj,kk)==46 % bone marrow
                wrist(ii,jj,kk)=4;
            end
        end
    end
end

for ii=1:ax
    for jj=1:ay
        for kk=1:az
            if wrist(ii,jj,kk)==49 %muscle
                wrist(ii,jj,kk)=10;
            end
        end
    end
end

for ii=1:ax
    for jj=1:ay
        for kk=1:az
            if wrist(ii,jj,kk)==44 %blood
                wrist(ii,jj,kk)=8;
            end
        end
    end
end

% assign tissues to colors
background = [60/255 60/255 150/255];
fat = [1 229/255 142/255];
bone_marrow = [158/255 135/255 114/255];
cortical_bone = [209/255 196/255 170/255];
skin = [245/255 165/255 170/255];
blood = [1 0 0];
muscle = [193/255 70/255 70/255];

% plotting each slide for xz cross section of a wrist model
bb=zeros(ax,az,1);
for kk=5:ay
    for ii=1:ax
        for jj=1:az

            bb(ii,jj)=wrist(ii,kk,jj);
        end
    end
    figure
    %imagesc(bb(:,:,1))
```

```
    hAxes = gca;
    imagesc(hAxes,bb(:,:,1));
    colormap(hAxes,[background;fat;bone_marrow;cortical_bone;skin;blood;muscle]);
end
```